



HAL
open science

Development of Smoothed Particle Hydrodynamics approach for modelling of multiphase flows with interfaces

Kamil Szewc

► **To cite this version:**

Kamil Szewc. Development of Smoothed Particle Hydrodynamics approach for modelling of multiphase flows with interfaces. Other [cond-mat.other]. Université de Lorraine, 2013. English. NNT : 2013LORR0328 . tel-01750701

HAL Id: tel-01750701

<https://hal.univ-lorraine.fr/tel-01750701v1>

Submitted on 29 Mar 2018

HAL is a multi-disciplinary open access archive for the deposit and dissemination of scientific research documents, whether they are published or not. The documents may come from teaching and research institutions in France or abroad, or from public or private research centers.

L'archive ouverte pluridisciplinaire **HAL**, est destinée au dépôt et à la diffusion de documents scientifiques de niveau recherche, publiés ou non, émanant des établissements d'enseignement et de recherche français ou étrangers, des laboratoires publics ou privés.



AVERTISSEMENT

Ce document est le fruit d'un long travail approuvé par le jury de soutenance et mis à disposition de l'ensemble de la communauté universitaire élargie.

Il est soumis à la propriété intellectuelle de l'auteur. Ceci implique une obligation de citation et de référencement lors de l'utilisation de ce document.

D'autre part, toute contrefaçon, plagiat, reproduction illicite encourt une poursuite pénale.

Contact : ddoc-theses-contact@univ-lorraine.fr

LIENS

Code de la Propriété Intellectuelle. articles L 122. 4

Code de la Propriété Intellectuelle. articles L 335.2- L 335.10

http://www.cfcopies.com/V2/leg/leg_droi.php

<http://www.culture.gouv.fr/culture/infos-pratiques/droits/protection.htm>



KAMIL SZEWC

DEVÉLOPPÉMENT D'UNE APPROCHE PARTICULAIRE
DE TYPE SPH POUR LA MODÉLISATION DES
ÉCOULEMENTS MULTIPHASIQUES AVEC
INTERFACES VARIABLES

THESE

PRÉSENTÉE EN VUE DE L'OBTENTION DU GRADE DE
DOCTEUR DE L'UDL ET L'IMP
SPÉCIALITÉ
MÉCANIQUE ET ENERGÉTIQUE

SOUTENANCE PRÉVUE LE 24/06/2013

Devant le jury composé de:

Rapporteurs:	M. Konrad Bajer	Professeur, Université de Varsovie
	M. David Le Touzé	Professeur, Ecole Centrale de Nantes
Examineurs:	M. Michel Gradeck	MCF HDR, Université de Lorraine
	M. Grégory Lefèbvre	Chargé de Recherche HDR, CNRS
	M. Jacek Pozorski	Professeur, IMP (Directeur de thèse)
	Mme. Anne Tanière	MCF HDR, Université de Lorraine (Directeur de thèse)
Invités:	M. Jean-Pierre Minier	Ingénieur de Recherche, EDF

GDAŃSK 2013



KAMIL SZEWC

DEVELOPMENT OF SMOOTHED PARTICLE
HYDRODYNAMICS APPROACH FOR MODELLING
OF MULTIPHASE FLOWS WITH INTERFACES

A DISSERTATION PRESENTED TO

THE INSTITUTE OF FLUID FLOW MACHINERY,
POLISH ACADEMY OF SCIENCES, GDAŃSK, POLAND

AND

THE UNIVERSITY OF LORRAINE, NANCY, FRANCE

FOR THE DEGREE OF
DOCTOR OF PHILOSOPHY

SUPERVISORS:

JACEK POZORSKI, D.Sc.

ANNE TANIÈRE, D.Sc.

GDAŃSK 2013

Declaration of Authorship

I, Kamil Szewc, declare that this thesis titled 'Development of Smoothed Particle Hydrodynamics approach for modelling of multiphase flows with interfaces' and the work presented in it are my own. I confirm that:

- This work was done wholly or mainly while in candidature for a research degree at the Institute of Fluid-Flow Machinery, Polish Academy of Science and the University of Lorraine.
- Where I have quoted from work of others, the source is always given. With the exception of such quotations, this thesis is entirely my own work.
- I have acknowledged all main sources of help.

Acknowledgements

I owe my deepest gratitude to those who helped me to complete this thesis. My supervisors Dr. Jacek Pozorski (Institute of Fluid-Flow Machinery, Polish Academy of Sciences, Gdańsk) and Dr. Anne Tanière (University of Lorraine, Nancy) gave me encouragement, guidance and support from the initial to the final level enabled me to overcome many difficulties. Jean-Pierre Minier (Électricité de France, Paris) inspired me with many creative ideas. I am grateful to my work mates: Maria Knorps, Christophe Henry, Arek Grucelski, Michał Butterweck, Patryk Chaja and Mirosław Łuniewski for the coffee sessions full of, not always, inspiring discussions. Special thanks to my parents, grandparents and all of my relatives for their support despite the distance separating the beautiful Upper Silesia from all the places I spent my PhD studies. Lastly, the most importantly, I wish to thank my wife Kasia. Your love, patience and understanding are out of this world.

Summary

Smoothed Particle Hydrodynamics (SPH) is a fully Lagrangian, particle based approach for fluid-flow simulations. One of its advantages over Eulerian techniques is no need of a numerical grid. Therefore, there is no necessity to handle the interface shape as it is done in Volume-of-Fluid, Level-Set or Front-Tracking methods. Thus, the SPH approach is increasingly used for hydro-engineering and geophysical applications involving free-surface flows where the natural treatment of evolving interfaces makes it an attractive method. However, for real-life multi-phase simulations this method has only started to be considered and many problems like a proper formulation or a spurious fragmentation of the interface remain to be solved.

One of the aims of this work is to critically analyse the existing SPH variants and assess their suitability for complex multi-phase problems. For modelling the surface-tension phenomena the Continuum Surface Force (CSF) methods are validated and used. The natural convection phenomena are modeled using a new, more general formulation, beyond the Boussinesq approximation. A substantial part of the work is devoted to the problem of a spurious fragmentation of the interface (the micro-mixing of SPH particles). Its negative effects and possible remedies are extensively discussed and a new variant is proposed. Contrary to general opinion, it is proven that the micro-mixing is not only the problem of flows with negligible surface tension.

A significant part of this work is devoted to the modelling of bubbles rising through liquids, including bubble-bubble interactions. The SPH simulations were performed for several flow regimes corresponding to different relative importance of surface tension, viscosity and buoyancy effects. The predicted topological changes, bubble terminal velocity and drag coefficients were validated with respect to reference experimental data and compared to other numerical methods.

In the work, fundamental concepts of assuring the incompressibility constraint in SPH are also recalled. An important part of work is a thorough comparison of two different incompressibility treatments: the weakly compressible approach, where a suitably chosen equation of state is used, and truly incompressible method (in two basic variants), where the velocity field is projected onto a divergence-free space. Their usefulness for multi-phase modelling is discussed. Problems associated with the numerical setup are investigated, and an optimal choice of the computational parameters is proposed and verified. For these purposes the study is supported by many two- and three-dimensional validation cases.

In addition, the present work opens new perspectives to future simulations of boiling phenomena using the SPH method. First ideas and sketches for the implementation of the liquid-vapour phase change are presented.

Summary (in Polish)

TYTUŁ PRACY: ROZWÓJ METODY SMOOTHED PARTICLE HYDRODYNAMICS DLA PRZEPLYWÓW Z POWIERZCHNIAMI ROZDZIAŁU

Smoothed Particle Hydrodynamics (SPH) jest w pełni Lagranżowska, bazująca na cząstkach, metodą hydrodynamiki obliczeniowej. Jedną z głównych zalet tego podejścia, w stosunku do metod Eulerowskich, jest brak siatki obliczeniowej. W metodzie SPH, nie ma konieczności śledzenia lub rekonstrukcji powierzchni rozdziału, inaczej niż ma to miejsce w przypadku takich metod numerycznych jak Volume-of-Fluid, Level-Set, czy Front-Tracking. Dlatego też, ta metoda jest coraz chętniej wykorzystywana do obliczeń hydrotechnicznych i geofizycznych z powierzchnią swobodną. W przypadku obliczeń przepływów wielofazowych z powierzchniami rozdziału, metoda SPH dopiero zaczyna być stosowana, a co za tym idzie, wiele problemów takich jak poprawne sformułowanie równań, czy zjawisko mikro-mieszania cząstek występujące na powierzchni rozdziału wymaga rozwiązania.

Jednym z celów pracy jest krytyczna analiza istniejących wariantów metody SPH, a także ocena ich użyteczności pod kątem symulacji przepływów wielofazowych z powierzchniami rozdziału. W celu modelowania napięcia powierzchniowego zbadano i wykorzystano techniki Continuum Surface Force. Konwekcja naturalna została symulowana z wykorzystaniem nowego, bardziej ogólnego podejścia niż przybliżenie Boussinesqa. Istotną część pracy poświęcono problemowi mikro-mieszania cząstek SPH na powierzchni rozdziału. Obszernie przedyskutowano negatywny wpływ tego efektu na jakość wyników jak i sposoby jego ograniczenia. W pracy pokazano, że – wbrew panującej opinii – zjawisko mikro-mieszania występuje nie tylko w przepływach z zanedbywalnym wpływem napięcia powierzchniowego.

Dużą część pracy poświęcono problemowi modelowania wzrostu pęcherzyków gazu w cieczy, włączając ich oddziaływanie poprzez ślad hydrodynamiczny. Symulacje przeprowadzono dla wielu parametrów odpowiadających różnemu wpływowi napięcia powierzchniowego, lepkości i sił wyporu. Prędkości, zmiany kształtu i współczynniki oporu pęcherzyków porównano zarówno z danymi doświadczalnymi, jak również z wynikami otrzymanymi za pomocą innych metod numerycznych.

Istotną część pracy stanowi rzetelne porównanie dwóch podejść zapewnienia nieściśliwości płynu w metodzie SPH: modelu ze sztuczną ściśliwością, gdzie wykorzystywane jest odpowiednio dobrane równanie stanu, oraz modelu, w którym pole prędkości jest rzutowane na przestrzeń o zerowej dywergencji. Przedyskutowano użyteczność obu podejść dla zagadnień przepływów wielofazowych z powierzchniami rozdziału. Analizę przeprowadzono na podstawie wyników uzyskanych dla wielu dwu- i trójwymiarowych przypadków testowych. Dokonano także optymal-

nego doboru parametrów numerycznych.

Dodatkowo, praca otwiera nowe perspektywy dla podjęcia symulacji numerycznych procesów wrzenia z wykorzystaniem metody SPH. Zaproponowano i przedyskutowano pierwsze koncepcje dotyczące modelowania zjawiska przemiany fazowej gaz-ciecz.

Summary (in French)

TITRE: DÉVELOPPEMENT D'UNE APPROCHE PARTICULAIRE DE TYPE SPH POUR LA MODÉLISATION DES ÉCOULEMENTS MULTIPHASIQUES AVEC INTERFACES VARIABLES

L'approche Smoothed Particle Hydrodynamics (SPH) est une méthode de calcul pour simuler des écoulements fluides avec une méthode Lagrangienne de type suivi de particules. A l'inverse des méthodes Euleriennes, ce type d'approche ne nécessite pas de maillage. C'est là l'un des atouts majeurs de l'approche SPH puisqu'elle permet de s'affranchir des méthodes de suivi d'interfaces couramment utilisées dans les approches Eulériennes (par exemple Volume-of-Fluid, Level-Set ou Front-Tracking). L'approche SPH est donc de plus en plus utilisée dans les domaines de l'hydro-ingénierie et de la géophysique notamment de part le traitement naturel des écoulements à surface libre dans la méthode SPH. Cependant, l'approche SPH n'est utilisée que depuis peu pour simuler des écoulements multiphasiques complexes et de nombreux problèmes restent en suspens, notamment concernant une formulation adéquate ou le micro-mélange aux interfaces.

L'un des principaux enjeux de ces travaux de thèse est d'analyser de façon objective les différentes approches de type SPH existantes et d'évaluer leur capacité à simuler des écoulements multiphasiques complexes. Ainsi, la modélisation des phénomènes liés à la tension de surface a été réalisée et validée via l'utilisation de techniques de type Continuum Surface Force. Les phénomènes de convection naturelle ont quant à eux été modélisés grâce à une nouvelle formulation plus générale (non-Boussinesq). Une partie de ces travaux est dédiée à l'étude des problèmes de micro-mélange aux interfaces: les effets indésirables (notamment la fragmentation de l'interface) sont analysés et des solutions sont proposées.

Une autre part de travail porte sur la modélisation des mouvements ascendants de bulles dans des liquides, avec l'inclusion des interactions entre bulles. Des simulations SPH ont été réalisées pour différents régimes d'écoulement, chacun d'eux correspondant à un ratio spécifique entre la tension de surface, la viscosité et la flottabilité. Les prédictions numériques de la topographie des bulles, de leur vitesse ainsi que de leur coefficient de traînée ont été validées. Pour ce faire, les résultats numériques ont été comparés non seulement aux données expérimentales de référence mais également à d'autres simulations numériques de bulles ascendantes.

Dans ces travaux de thèse, une étude détaillée des concepts liés aux contraintes d'incompressibilité a été réalisée. Dans cet objectif, deux traitements différents ont été comparés: l'approche faiblement compressible (où une équation d'état adéquate est choisie) et l'approche incompressible (où une projection des champs de vitesse

sur un espace sans divergence est réalisée de deux façons différentes). La pertinence de ces modèles pour des simulations d'écoulements multiphasiques est également évaluée. Les problèmes associés aux paramètres numériques sont discutés et un choix approprié de ces paramètres est proposé. Pour ce faire, de nombreux calculs de validation en deux et trois dimensions ont été réalisés.

Enfin, une extension est proposée pour simuler les phénomènes liés à l'ébullition via une approche SPH. Ce sujet étant encore en friche, de nouvelles idées et schémas sont proposés pour le changement de phase liquide-vapeur dans l'approche SPH.

Contents

Declaration of Authorship	iii
Acknowledgements	v
Summary	vii
1 Introduction	1
2 SPH formulation	5
2.1 Basic ideas	5
2.2 Governing equations	7
2.3 Incompressibility condition	10
2.3.1 Weakly Compressible SPH (WCSPH)	10
2.3.2 Truly Incompressible SPH (ISPH)	10
2.4 Time step criteria	12
2.5 Boundary conditions	13
2.6 Hydrostatic pressure computation	18
3 Assessment of the SPH approaches	21
3.1 Introduction	21
3.2 Lid-driven cavity (2D)	22
3.2.1 The kernel type influence	22
3.2.2 The kernel size influence	24
3.2.3 The particle number influence	24
3.3 Lid-driven cavity (3D)	27
3.4 The Rayleigh-Taylor instability (2D)	31
3.5 Density error estimation	32
3.6 Incompressible SPH with density correction	35
3.7 The need to use the density correction procedure	39
3.7.1 Cube-to-sphere droplet deformation (3D)	39
3.8 Conclusions	41
4 Multiphase SPH	43
4.1 Introduction	43
4.1.1 Standard formulation	44
4.1.2 Colagrossi and Landrini formulation	44
4.1.3 Hu and Adams formulation	45
4.1.4 Grenier et al. formulation	48

4.2	Micro-mixing phenomenon	50
4.3	Conclusions	56
5	Surface-tension force in SPH	59
5.1	Introduction	59
5.2	Computation of the vector normal to interface	59
5.3	Continuum Surface Force model (CSF)	61
5.4	CSF - Surface Stress Tensor model (CSF-SST)	63
5.5	Numerical validation tests	64
5.5.1	Square-droplet deformation	64
5.5.2	Capillary wave	67
5.6	Conclusions	70
6	Simulations of bubbles rising through liquids using SPH	71
6.1	Introduction	71
6.2	Single bubbles	73
6.2.1	Shape	76
6.2.2	Terminal velocity	78
6.2.3	$C_D - Re$ correlation	78
6.3	Bubble-bubble interaction	80
6.4	Conclusions	82
7	Heat transfer modelling using SPH	83
7.1	Introduction	83
7.2	Conduction modelling	83
7.2.1	Heat conduction in slabs	85
7.3	Natural convection	85
7.3.1	Introduction	85
7.3.2	Booussinesq approximation	87
7.3.3	Non-Booussinesq (general) regime	88
7.3.4	Flow in a differentially heated square cavity	89
7.4	Conclusions	95
8	Towards phase-change simulations	97
8.1	Introduction	97
8.2	Freezing	98
8.3	Boiling	99
8.3.1	Particle pushing model	100
8.3.2	Variable mass and volume model	103
8.4	Conclusions	109
9	Perspectives	111
	Bibliography	113
	List of publications	125

Chapter 1

Introduction

Fluid dynamic systems involving multiple phases separated by interfaces are common in many technological, biological and geophysical problems. From numerical point of view, modelling of multiphase flows is a very complex problem. Up to now, the vast majority of CFD studies carried out to address this issue have been based on a fixed-grid solvers of governing equations. To capture the interface evolution these methods explicitly handle (reconstruct or track) the interface position. The examples of such methods are: Volume-Of-Fluid (Hirt and Nichols, 1981), Front-Tracking (Tryggvason et al., 2001; Unverdi and Tryggvason, 1992), Level-Set (Sussman et al., 1994), and their combinations. All these methods were proven to be useful in many applications, but, in many circumstances, due to such problems as an additional numerical diffusion caused by the interface handling, achieving high accuracy is challenging. In this thesis, these approaches are so-called Eulerian methods.

A very promising alternative are grid-free particle approaches (here so-called Lagrangian methods). Some of the most common particle methods able to simulate multi-phase flows are: the Moving Particle Semi-implicit (Yoon et al., 2001), Discrete Element Method (Zhu et al., 2008) and Smoothed Particle Hydrodynamics (Monaghan, 2012). All of them are relatively new and all these methods are very closely related. Some of their main advantages over grid-based approaches are: no need to reconstruct the interface (it is directly obtained from the set of the computational particles) and easiness to deal with complex geometries (no need to create numerical grid). However, due to the relatively small interest in such methods by the community, there are many points where these methods have to be improved.

Yet another approach are the methods combining grid-based and grid-free ideas. Examples are: Particle-in-Cell (Andrews and O'Rourke, 1996), Marker-and-Cell (Harlow and Welch, 1957; McKee et al., 2008), Lattice Boltzmann Method (Aidun and Clausen, 2010). The most promising approach among them, mainly due to the numerical efficiency, is LBM.

In this work, since we are interested in a potential application of the Lagrangian approaches to multi-phase flows with phase changes, we decided to critically analyse the existing Smoothed Particle Hydrodynamics variants and assess their usefulness to simulate complex multiphase problems. In the areas where these variants fail, we set ourselves a new goal to understand the reason for such behaviour and to propose some remedies.

The Smoothed Particle Hydrodynamics (SPH) method was independently proposed by Gingold and Monaghan (1977) and Lucy (1977) to simulate some astrophysical phenomena at the hydrodynamic level. The main idea of the SPH method is to introduce kernel interpolants for flow quantities so that fluid dynamics is represented by a set of particle evolution equations. Then three approximations are made to devise practical formulation, cf. Chapter 1. Due to the fact that SPH is a fully Lagrangian technique and there is no necessity to handle the interface position as it is obligatory in Eulerian methods, during the last ten years, the SPH approach has been greatly developed to deal with free-surface and, recently, multi-phase flows. One of the disadvantages of the SPH method is the numerical efficiency when compared to other grid-based approaches. However, in many cases involving complex geometry, the ‘human’ time needed to create a computational grid can be so long, that it is going to be more efficient to perform calculations using the SPH approach.

Nowadays, the SPH approach is increasingly used for hydro-engineering applications involving free-surface flows where the natural treatment of evolving interfaces makes it an attractive method. The applications of the SPH in hydro-engineering include:

- Wave dynamics: Dalrymple and Rogers (2006), Shao et al. (2006), Kim and Ko (2008), Khayyer et al. (2008), Li et al. (2012)
- Water collapse: Monaghan (1994), Shao and Lo (2003), Colagrossi and Landrini (2003), Grenier et al. (2009), Lee et al. (2010)
- Sloshing flows: Delorme (2008), Shao et al. (2012)
- Marine-engineering: Le Touzé et al. (2010), Marrone et al. (2011), Veen and Gourlay (2012)

The SPH method was also shown to be applicable (very successfully) to a wide variety of fields different than hydro-engineering. The examples are:

- Astrophysical flows
 - Star formation: Berczik (2000), Nagamine et al. (2004), Bürzle et al. (2010)
 - Cosmology: Shapiro et al. (1996), Springel et al. (2005),
 - Collisions: Faber and Rasio (2000), Faber and Rasio (2001), Trac et al. (2007), Jutzi et al. (2013)
 - Supernova explosions: Nagasawa et al. (1988), Liu et al. (2012)
 - Review: Springel (2010)
- Geophysical flows
 - Geomorphology: Vandamme et al. (2012)
 - Glaciology: Shen et al. (2000), Wenxiao et al. (2012)
 - Volcanology: Haddad et al. (2010), Prakash and Cleary (2011)

- Biophysical flows
 - Swimming bodies: Kajtar and Monaghan (2010, 2012)
 - Medicine: Chui and Heng (2010), Sinnott et al. (2012)
- Solid mechanics
 - Impact problems: Johnson et al. (1996) Guida et al. (2011) Grimaldi et al. (2013)
 - Fracture modelling: Benz and Asphaug (1993, 1995)
 - Metal forming: Cleary and Ha (2002), Cleary et al. (2006), Cleary (2010)

This thesis is divided into eight chapters. The first one is the present introduction. In Chapter 2, fundamental concepts of the method are briefly recalled. Then, in Chapter 3, we present a thorough comparison of two different incompressibility treatments in SPH: the weakly compressible approach, where a suitably chosen equation of state is used, and the truly incompressible method (in two basic variants), where the velocity field projection onto a divergence-free space is performed. A noteworthy aspect of the study is that in each incompressibility treatment, the same boundary conditions are used (and further developed) that allows for a direct comparison to be made. Two-dimensional and three-dimensional validation cases are studied. Problems associated with the numerical setup are discussed, and an optimal choice of the computational parameters is proposed and verified. The efficiency issues of the incompressibility treatments are considered, and the speed-up features are highlighted. The results show that the present state-of-the-art truly incompressible methods (based on a velocity correction) suffer from density accumulation errors. To address this issue, an algorithm, based on a correction for both particle velocities and positions, is presented. The usefulness of this density correction is examined and demonstrated.

The main purpose of Chapter 4 is a critical analysis of the SPH variants to assess their influence on multiphase flow simulations. We give a special attention to the multi-phase formulations proposed by Colagrossi and Landrini (2003), Hu and Adams (2006) and Grenier et al. (2009). Comparing these techniques, it is easy to notice how some small details may have a strong impact on the results. The comparison is performed using common validation tests: the Rayleigh-Taylor instability, a square-droplet deformation and a bubble rising in water. However, the main advantage of the SPH approach, which is no necessity to handle the position of the interface, unfortunately implies a problem – the spurious fragmentation of the interface (micro-mixing). The main reason of this phenomenon is a lack of mechanism assuring immiscibility of phases in SPH. In this chapter, all the remedies available in the literature are discussed, and, a new variant of sharpness correction procedure is proposed and validated.

Chapter 5 contains a comparison of two macro-scale surface tension models based on the Continuum Surface Force (CSF) approach. The first, basic, concept consists in the SPH computation of a local curvature of an interface. In the second approach, the surface tension force is computed using a surface stress tensor. The validation of the surface tension models is assessed with two standard numerical tests: the square-droplet deformation and the water droplet in air oscillation.

In the Chapter 6, the shapes and dynamics of bubbles rising through a liquid are studied using the SPH approach. For that purpose a multiphase formulation of SPH that can address large density differences is retained, while surface tension effects are explicitly accounted for through the CSF model based on the computation of a local curvature of an interface. To the best of our knowledge, SPH has not yet been widely used for two-phase flows and there is still a lack of proper validation for fully three-dimensional multi-phase flows with high density ratios, further compounded by surface tension and gravitation force influence. Numerical simulations were performed for different regimes (corresponding to different relative importance of surface tension, viscosity and buoyancy effects) and the predicted topological changes as well as the terminal velocity and drag coefficients of bubbles are validated. The numerical outcomes are assessed not only with respect to reference experimental data but also with respect to other numerical methods, namely the Front-Tracking and the Lattice Boltzmann methods.

Chapter 7 is divided into two parts. The first one contains a short introduction to the SPH implementations of heat transfer phenomena. A new SPH form of energy equation is also introduced and validated. In the second part, the usefulness of the Boussinesq approximation for simulations of the natural convection is discussed and a new SPH technique of simulation of this phenomena is introduced.

Chapter 8 is devoted to discussion about the application of SPH for simulations of phase-change phenomena. The usefulness of SPH for modelling of a solidification/melting is proven by many authors. The first part of this chapter is a very short introduction to a solidification/melting modelling with SPH. However, in the case of an evaporation/condensation (boiling) phenomena the situation is different. To the best of our knowledge, the possibility of applying the SPH method to modelling evaporation/condensation problems (except the mesoscopic description proposed by Charles and Daivis (2009)) was never discussed in the literature. In the second part of the Chapter 8 our first ideas and sketches for an implementation of the liquid-vapour phase change are presented and potential advantages and drawbacks are discussed.

Chapter 2

SPH formulation

2.1 Basic ideas

The main idea behind SPH is the introduction of kernel interpolants for the field quantities so that the fluid dynamics is represented by a set of particle evolution equations, cf. Monaghan (1992, 2012) and Liu and Liu (2003) for a review. Then, three approximations are made to devise practical formulations.

The first is interpolation of the field quantities at a point. To construct it, we utilise an integral interpolant $\hat{A}(\mathbf{r})$ of any field $A(\mathbf{r})$ (for simplicity we consider here a scalar field)

$$\hat{A}(\mathbf{r}) = \int_{\Omega} A(\mathbf{r}') W(\mathbf{r} - \mathbf{r}', h) d\mathbf{r}', \quad (2.1)$$

where the integration is over all the domain Ω and $W(\mathbf{r}, h)$ is a weighting function (the kernel) with the parameter h called the smoothing length.

Generally, the kernel should be even (symmetric) function

$$W(\mathbf{r}, h) = W(-\mathbf{r}, h), \quad (2.2)$$

satisfy the limit condition

$$\lim_{h \rightarrow 0} W(\mathbf{r}, h) = \delta(\mathbf{r}), \quad (2.3)$$

where $\delta(\mathbf{r})$ is the Dirac delta distribution, and should be normalised so that

$$\int_{\Omega} W(\mathbf{r}, h) d\mathbf{r} = 1. \quad (2.4)$$

Additionally, the kernel should be sufficiently smooth.

The limit condition is necessary to ensure the convergence of the interpolation

$$\lim_{h \rightarrow 0} \hat{A}(\mathbf{r}) = \lim_{h \rightarrow 0} \int_{\Omega} A(\mathbf{r}') W(\mathbf{r} - \mathbf{r}', h) d\mathbf{r}' = \int_{\Omega} A(\mathbf{r}') \delta(\mathbf{r} - \mathbf{r}', h) d\mathbf{r}' \equiv A(\mathbf{r}). \quad (2.5)$$

The error of the kernel interpolation can be estimated using Taylor expansion of the field $A(r)$ around r (1D for simplicity)

$$\hat{A}(r) = \int_{\Omega} \left[A(r) + A'(r)(r - r') + \frac{1}{2} A''(r)(r - r')^2 + \dots \right] W(r - r', h) dr'. \quad (2.6)$$

Since $W(r, h)$ is an even function, the second r.h.s. term disappears

$$\int_{\Omega} (r - r')W(r - r', h)dr' = 0, \quad (2.7)$$

as well as other odd terms. Due to the normalisation condition, Eq. (2.6) becomes

$$\widehat{A}(r) = A(r) + O(h^2), \quad (2.8)$$

which gives the second order accuracy of the kernel approximation. It is important to note that it is possible to formulate kernels of higher order accuracy by elimination of higher order terms, cf. Gingold and Monaghan (1982). However, such kernels are locally negative which implies additional difficulties but negligible increase of accuracy (Morris, 1996).

Taking into consideration the computational effort and the proper implementation of the boundary conditions it is worth using kernels having a compact support, cf. Sect. 2.5. Since there are a lot of possibilities to choose $W(\mathbf{r}, h)$, in Chapter 3 we decided to compare solutions obtained employing three different (the most commonly used) 2D kernels: the cubic B-spline form (Schoenberg, 1946)

$$W(\mathbf{r}, h) = \frac{10}{7\pi h^2} \begin{cases} 1 - \frac{3}{2}q^2 + \frac{3}{4}q^3, & \text{for } 0 \leq q < 1, \\ \frac{1}{4}(2 - q)^3, & \text{for } 1 \leq q < 2, \\ 0, & \text{otherwise,} \end{cases} \quad (2.9)$$

the quintic B-spline form introduced by Morris et al. (1997)

$$W(\mathbf{r}, h) = \frac{7}{478\pi h^2} \begin{cases} (3 - q)^5 - 6(2 - q)^5 + 15(1 - q)^5, & \text{for } 0 \leq q < 1, \\ (3 - q)^5 - 6(2 - q)^5, & \text{for } 1 \leq q < 2, \\ (3 - q)^5, & \text{for } 2 \leq q < 3, \\ 0, & \text{otherwise,} \end{cases} \quad (2.10)$$

and the quintic form proposed by Wendland (1995)

$$W(\mathbf{r}, h) = \frac{7}{4\pi h^2} \begin{cases} \left(1 - \frac{q}{2}\right)^4 (2q + 1), & \text{for } q < 2, \\ 0, & \text{otherwise,} \end{cases} \quad (2.11)$$

where $q = |\mathbf{r}|/h$. The Wendland kernel is also used for 3D simulations with the normalisation constant $21/16\pi h^3$ instead. General approach to construct analytical smoothing functions for SPH and other mesh-free methods is presented in Liu et al. (2003).

The second approximation of the SPH technique is the field discretisation. It is done through dividing medium into a fine-grained representation (particles). Each particle carries the properties of the field. The integral interpolant $\widehat{\langle \cdot \rangle}$, Eq. (2.1), becomes then the summation interpolant $\langle \cdot \rangle$

$$\langle A \rangle(\mathbf{r}) = \sum_b A(\mathbf{r}_b)W(\mathbf{r} - \mathbf{r}_b, h)\Omega_b, \quad (2.12)$$

where \mathbf{r}_b and Ω_b denote the position and volume of the particle b . Specifically, the SPH task involves the computations of the interpolant at each particle, so that Eq. (2.12) may be rewritten into the common form

$$\langle A \rangle_a = \sum_b A_b W_{ab}(h)\Omega_b, \quad (2.13)$$

where $\langle A \rangle_a = \langle A \rangle(\mathbf{r}_a)$, $A_a = A(\mathbf{r}_a)$ and $W_{ab}(h) = W_{ba}(h) = W(\mathbf{r}_b - \mathbf{r}_a, h)$. Thus, the subscript a denotes the computational particle/node.

An additional advantage of SPH reveals with the differentiation of fields. In accordance with (2.1), the gradient of $A(\mathbf{r})$ assumes the form

$$\widehat{\nabla A}(\mathbf{r}) = \int_{\Omega} \nabla A(\mathbf{r}') W(\mathbf{r} - \mathbf{r}', h) d\mathbf{r}'. \quad (2.14)$$

Taking advantage of the integration by parts and utilizing the kernel symmetry, we can transform the foregoing equation into

$$\widehat{\nabla A}(\mathbf{r}) = \int_{\partial\Omega} A(\mathbf{r}') W(\mathbf{r} - \mathbf{r}') \mathbf{n}' dS + \int_{\Omega} A(\mathbf{r}') \nabla' W(\mathbf{r} - \mathbf{r}', h) d\mathbf{r}', \quad (2.15)$$

where $\mathbf{n}' = \mathbf{n}(\mathbf{r}')$ is the normal vector to surface element dS . Generally, the first term does not necessarily vanish for finite domain sizes, cf. (Feldman and Bonet, 2007). However, it is a common practice to neglect this term and deal with the boundaries explicitly, cf. Sect. 2.5. The SPH form (discretisation) of (2.15) brings the common rule

$$\langle \nabla A \rangle_a = \sum_b A_b \nabla_a W_{ab}(h) \Omega_b. \quad (2.16)$$

Since the nabla operator acts only on the kernel, the gradient of the field is dependent only on the values of the fields at particles, not gradients.

The third SPH feature is the assumption that the field value A_a at a point and its SPH approximation $\langle A \rangle$ are in relation

$$\langle A \rangle_a \approx A_a. \quad (2.17)$$

Since, in the case of the time dependent simulations, the calculation of the field quantities at each time step is performed using the results obtained in the previous step, the above introduced assumption becomes natural.

2.2 Governing equations

The full set of governing equations for incompressible viscous flows is composed of the Navier-Stokes (N-S) equation

$$\frac{d\mathbf{u}}{dt} = -\frac{1}{\rho} \nabla p + \frac{1}{\rho} (\nabla \cdot \mu \nabla) \mathbf{u} + \mathbf{f}, \quad (2.18)$$

where $\rho = \text{const}$ is the density, \mathbf{u} the velocity, t the time, p the pressure, ν the kinematic viscosity and \mathbf{f} an external force, and the continuity equation

$$\frac{d\rho}{dt} = -\rho \nabla \cdot \mathbf{u}, \quad (2.19)$$

that for $\rho = \text{const}$ arises to the form

$$\nabla \cdot \mathbf{u} = 0. \quad (2.20)$$

The whole set of governing equations should now be expressed in the SPH formalism. Utilising the relation (2.16), the divergence of velocity becomes

$$\langle \nabla \cdot \mathbf{u} \rangle_a = \sum_b \mathbf{u}_b \cdot \nabla_a W_{ab}(h) \Omega_b. \quad (2.21)$$

Therefore, the continuity equation (2.19) takes the form

$$\frac{d\rho_a}{dt} = -\rho_a \sum_b \frac{m_b}{\rho_b} \mathbf{u}_b \cdot \nabla_a W_{ab}(h), \quad (2.22)$$

where the particle mass is $m_b = \rho_b \Omega_b$. However, for constant velocity field \mathbf{u} , the above form of velocity divergence does not vanish explicitly. In addition, the result is very sensitive to particle disorder (Monaghan, 2005a,b; Morris, 1996). Therefore, due to these reasons (accuracy), it is a good idea to do some modifications to obtain other forms of continuity equation. Applying the identity

$$\rho \nabla \cdot \mathbf{u} \equiv \nabla \cdot (\rho \mathbf{u}) - \mathbf{u} \cdot \nabla \rho. \quad (2.23)$$

to the Eq. (2.19), we can obtain the most commonly used SPH form

$$\frac{d\rho_a}{dt} = \sum_b m_b \mathbf{u}_{ab} \cdot \nabla_a W_{ab}(h), \quad (2.24)$$

where $\mathbf{u}_{ab} = \mathbf{u}_a - \mathbf{u}_b$. The use of this form of continuity equation ensures no density changes for constant velocity fields. Alternatively, the use of identity

$$\nabla \cdot \mathbf{u} \equiv \nabla \cdot \mathbf{u} - \mathbf{u} \cdot \nabla I, \quad (2.25)$$

where I is the unit scalar field, allows to write the continuity equation in the form proposed by Colagrossi and Landrini (2003)

$$\frac{d\rho_a}{dt} = \rho_a \sum_b \frac{m_b}{\rho_b} \mathbf{u}_{ab} \cdot \nabla_a W_{ab}(h). \quad (2.26)$$

The main advantage of Eq. (2.26) over Eq. (2.24) is higher accuracy in multiphase systems. For detailed description of this issue, cf. Chapter 4. It is important to note that due to the numerical errors and used approximations, in all forms based on computation of velocity divergence $\nabla \cdot \mathbf{u}$, the density and velocity fields can become inconsistent. Since the mass of the particles does not change during a simulation, the density and the particle volumes are affected.

However, there also exists an alternative formulation, maintaining the density field consistent with others, with the fluid density computed directly from the SPH formula (2.13)

$$\rho_a = \sum_b \rho_b W_{ab}(h) \Omega_b = \sum_b m_b W_{ab}(h). \quad (2.27)$$

A practical disadvantage of this approach is that ρ must be evaluated by summing over the particles (the computation of the kernel functions) before other quantities (where only the gradients of kernel are used) cf. Morris (1996); Morris et al. (1997). Therefore, the computational effort increases (Sect. 3.2). Another disadvantage is

the problem with representing sharp discontinuities near material interfaces. To avoid this difficulty, Hu and Adams (2006) suggested to use the form (cf. Sect. 4.1.3)

$$\varrho_a = m_a \sum_b W_{ab}(h). \quad (2.28)$$

In the SPH technique, the pressure N-S term is responsible for ensuring the incompressibility constraint (Sect. 2.3). Utilising Eq. (2.16) it takes the form

$$\left\langle \frac{1}{\varrho} \nabla p \right\rangle_a = \frac{1}{\varrho_a} \sum_b \frac{m_b}{\varrho_b} p_b \nabla_a W_{ab}(h). \quad (2.29)$$

However, since force with which two freely chosen particles interact is not antisymmetric with swapping positions

$$\frac{m_a m_b}{\varrho_a \varrho_b} p_b \nabla_a W_{ab}(h) \neq -\frac{m_b m_a}{\varrho_b \varrho_a} p_a \nabla_b W_{ba}(h), \quad (2.30)$$

this form does not conserve linear and angular momentum (Monaghan, 2005a).

Similarly to the continuity equation (2.24), the use of some identities allows one to write the pressure N-S term into conservative form. The most commonly used form is one obtained using relation

$$\frac{\nabla p}{\varrho} = \nabla \left(\frac{p}{\varrho} \right) + \frac{p}{\varrho^2} \nabla \varrho. \quad (2.31)$$

Applying the SPH interpolation procedures, the pressure N-S term can be written as

$$\left\langle \frac{1}{\varrho} \nabla p \right\rangle_a = \sum_b m_b \left(\frac{p_a}{\varrho_a^2} + \frac{p_b}{\varrho_b^2} \right) \nabla_a W_{ab}(h). \quad (2.32)$$

Since force between two freely chosen particles is antisymmetric with swapping positions, the linear and angular momentum are conserved. But, this form is not behaving well in the case of multiphase flows, cf. Chapter 4. To avoid a problem, Colagrossi and Landrini (2003) proposed another antisymmetric form

$$\left\langle \frac{1}{\varrho} \nabla p \right\rangle_a = \sum_b m_b \frac{p_a + p_b}{\varrho_a \varrho_b} \nabla_a W_{ab}(h). \quad (2.33)$$

As it was shown by (Bonet and Lok, 1999) it is very important (due to the energy conservation reasons) to perform the SPH simulations using the forms of the continuity equation and the N-S pressure term which are variationally consistent (in the absence of external forces). For instance, Eq. (2.32) is variationally consistent with Eq. (2.24), while Eq. (2.33) is consistent with Eq. (2.26). There are many ways to show the variational consistency (Bonet and Lok, 1999; Grenier et al., 2009; Monaghan, 2005a).

The viscous N-S term, containing the second derivative over velocity, can be also easily expressed using pure SPH approximations. Generally, there are two strategies to do this. The first consists in direct employment of second derivatives of kernel (Chaniotis et al., 2002; Takeda et al., 1994). The main disadvantage of this approach is high sensitivity to low resolution regions and necessity to perform simulations using high number of particles under the kernel hat. The second idea

consists in the use of first kernel derivatives, but, double loop over interacting particles (Watkins et al., 1996). Therefore, this method implies very high computational effort. To avoid these problems, Morris et al. (1997) proposed to express the viscous N-S term as a combination of the Finite Difference (FD) method and SPH approximations

$$\left\langle \frac{1}{\rho} (\nabla \cdot \mu \nabla) \mathbf{u} \right\rangle_a = \sum_b m_b \frac{\mu_a + \mu_b}{\rho_a \rho_b} \frac{\mathbf{r}_{ab} \cdot \nabla_a W_{ab}(h)}{r_{ab}^2 + \eta^2} \mathbf{u}_{ab}, \quad (2.34)$$

where $\eta = 0.01h$ is small regularising parameter added to avoid potential singularities. Many different variations of the FD-SPH approximation were also proposed (Cleary, 1998; Monaghan, 2005a; Shao and Lo, 2003).

Since SPH is fully Lagrangian approach, the particle advection equation completes the system

$$\frac{d\mathbf{r}_a}{dt} = \mathbf{u}_a. \quad (2.35)$$

2.3 Incompressibility condition

To compute incompressible flows in the Eulerian CFD, two approaches are commonly used: the artificial compressibility method (where a specific equation of state is applied) and the pressure-correction technique (where the velocity field is projected onto the divergence-free space). Generally, the analogues of these techniques are also used in the SPH approach. They are presented in the following.

2.3.1 Weakly Compressible SPH (WCSPH)

The most common technique is the weakly compressible SPH (WCSPH). It involves the set of governing equations closed by a suitably chosen, artificial equation of state $p = p(\rho)$. Since the fluid pressure is an explicit function of ρ , the density gradient exerts an influence on the particle motion. The commonly used equation of state has the form (Batchelor, 1967)

$$p = \frac{c^2 \rho_0}{\gamma} \left[\left(\frac{\rho}{\rho_0} \right)^\gamma - 1 \right], \quad (2.36)$$

where the reference density ρ_0 , the numerical sound speed c and parameter γ are suitably chosen to reduce the density fluctuations down to demanded level. In the present work, to assure density variations lower than 1%, we use $\gamma = 7$ and assume c at the level at least 10 times higher than the maximum fluid velocity (Monaghan, 1994). However, since the sound speed is high, the time step should be, correspondingly, very small (cf. Sect. 2.4). Therefore, the WCSPH method is commonly considered as a less efficient approach, however, as it is presented in Sect. 3.7, this is not always true.

2.3.2 Truly Incompressible SPH (ISPH)

An alternative technique is the truly incompressible SPH (ISPH). It is based on the Projection Method which is a common approach for numerically solving

time-dependent incompressible fluid-flow problems. In this technique the pressure needed to ensure incompressibility is found by projecting the calculated velocity field onto the divergence-free space (Cummins and Rudman, 1999). In the ISPH approach, the decomposition procedure of velocity into the potential and solenoidal part (the well-known Helmholtz decomposition) begins with splitting the integration of the N-S equation (2.18) over the time interval $\delta t = t^{n+1} - t^n$ into two parts. The first, so-called predictor step, gives the fractional velocity \mathbf{u}^*

$$\frac{\mathbf{u}^* - \mathbf{u}^n}{\delta t} = \nu \nabla^2 \mathbf{u}^n + \mathbf{f}^n. \quad (2.37)$$

The right-hand side of the above equation contains all the N-S terms except the pressure one. The second part of the procedure is the correction step to yield \mathbf{u}^{n+1}

$$\frac{\mathbf{u}^{n+1} - \mathbf{u}^*}{\delta t} = -\frac{1}{\rho} \nabla p^{n+1}. \quad (2.38)$$

It imposes the correction of \mathbf{u}^* to ensure compliance with the divergence-free constraint. To obtain an appropriate pressure p^{n+1} we write the divergence of Eq. (2.38)

$$\nabla \cdot \left(\frac{\mathbf{u}^{n+1} - \mathbf{u}^*}{\delta t} \right) = \nabla \cdot \left(-\frac{1}{\rho} \nabla p^{n+1} \right). \quad (2.39)$$

To have a divergence-free velocity field at the end of the time step, $\nabla \cdot \mathbf{u}^{n+1} = 0$, Eq. (2.39) becomes the Poisson equation for p^{n+1}

$$\nabla \cdot \left(\frac{1}{\rho} \nabla p^{n+1} \right) = \frac{\nabla \cdot \mathbf{u}^*}{\delta t}. \quad (2.40)$$

Finally, substitution of p^{n+1} into the correction step (2.38) yields the divergence-free velocity field.

It is important to note, that besides the ISPH approach based on projecting velocity field onto the divergence-free space, there exist also other formulations. Analogously to the Moving Particle Semi-implicit method (MPS) (Koshizuka et al., 1998), Shao and Lo (2003) proposed density invariant projection-based method. In this approach, density is evaluated during simulation by Eq. (2.27), then, the pressure field is obtained by solving the Poisson equation wherein the source term is not divergence of velocity, but, the relative density difference

$$\nabla \cdot \left(\frac{1}{\rho} \nabla p^{n+1} \right) = \left(\frac{\rho_0 - \rho}{\rho_0} \right) \frac{1}{\delta t^2}, \quad (2.41)$$

where ρ_0 is the reference density. However, despite rather accurate results of 2D dam-braking validation case presented by Shao and Lo (2003), for very basic cases like the Taylor-Green vortices or the Vortex Spin-Down, this approach gives inaccurate, very noisy and, for some cases ($Re > 10$), unstable results (Xu, 2009; Xu et al., 2009).

However, it may be shown, cf. Sect. 3.5 that if only the velocity divergence condition is used as a source term of the Poisson equation (2.40), density error can accumulate during simulation, which can lead to inaccurate results (cf. Sect. 3.7.1). To solve this problem, Pozorski and Wawreńczuk (2002) suggested to apply the second correction solving the second Poisson solver. The concept is described in detail in Sect. 3.6. A similar approach was later proposed, in the multiphase flow context, by Hu and Adams (2007).

Particle-based Poisson solver

Employing together the SPH formulae for the divergence and gradient operators, it is straightforward to obtain the direct SPH representation of the Laplace operator on the l.h.s. of (2.40). However, Cummins and Rudman (1999) performed a simple one-dimensional hydrostatic test to show that such an approach produces a distinct pressure decoupling pattern. To avoid this problem, it is common to utilise the approximate Laplacian operator with the similar form as the viscous N-S term (combination of SPH and Finite Difference approaches)

$$\left\langle \nabla \cdot \frac{1}{\rho} \nabla p \right\rangle_a \approx \sum_b \frac{m_b}{\rho_b} \frac{4}{\rho_a + \rho_b} \frac{p_{ab} \mathbf{r}_{ab} \cdot \nabla_a W_{ab}(h)}{r_{ab}^2 + \eta^2}, \quad (2.42)$$

where $p_{ab} = p_a - p_b$. The Poisson equation (2.40) is then solved on the irregular grid of Lagrangian points (particles); therefore, this variant of ISPH will be called here the Particle-based Poisson Solver (PPS).

However, the main disadvantage of the SPH-PPS method is its inefficiency, cf. Sect. 3.2. Dealing with the Poisson equation using Eq. (2.42) consists in solving a linear equation system with a sparse irregular and each time step different coefficient matrix (here Bi-CGSTAB algorithm proposed by Van der Vorst (1992)). It requires much more CPU time and available memory than the Poisson solvers performed on a regular grid.

Grid-based Poisson solver

The common way to solve the Poisson equation in the SPH approach is to compute it directly on particles (irregular grid). However, there exists another, less useful (specially for free-surface flows), but much more efficient treatment, called here the Grid-based Poisson Solver (GPS). It consists in projecting the r.h.s. of (2.40) on an auxiliary grid and then to crunch it with some commonly known (from Eulerian approaches) solvers. This is a standard technique in various particle methods (more precisely, particle-mesh methods) such as Lagrangian PDF (Pope, 1994) or Vortex-in-Cell (Cottet and Koumoutsakos, 2000).

2.4 Time step criteria

To assure the stability of the SPH scheme, several time step criteria must be satisfied, as amply discussed in Morris et al. (1997), Cleary and Monaghan (1999) and Monaghan (1992). We briefly recall them here.

In the case of the ISPH approach, the CFL time step condition is

$$\delta t \leq \delta t_{CFL} = 0.25 \frac{h}{|\mathbf{u}|_{max}}, \quad (2.43)$$

where $|\mathbf{u}|_{max}$ is maximum velocity in the flow. In the WCSPH approach, due to the utilisation of the equation of state (2.36), the CFL time step condition is

$$\delta t \leq \delta t_{CFL} = 0.25 \frac{h}{c + |\mathbf{u}|_{max}}. \quad (2.44)$$

Since we demand density fluctuations to be lower than 1%, we have chosen $c \geq 10|\mathbf{u}|_{max}$ (Sect. 2.3.1). Therefore, WCSPH seems to be computationally less efficient than the ISPH approaches. In the case of explicit schemes for viscous flows, another stability criterion is

$$\delta t \leq \delta t_v = 0.125 \frac{h^2}{\nu}. \quad (2.45)$$

Additional condition must be satisfied due to the magnitude of particle accelerations (eg. gravity) \mathbf{f}

$$\delta t \leq \delta t_f = 0.25 \min_a \left(\frac{h}{|\mathbf{f}_a|} \right)^{\frac{1}{2}}. \quad (2.46)$$

2.5 Boundary conditions

The proper implementation of the boundaries is one of the common topics in the SPH developments during recent years. Early stage applications of WCSPH involved high Reynolds number simulations with free-slip boundaries, performed using one layer of boundary particles placed at the wall. The layer exerted a strong repulsive force to prevent penetrating solid surfaces (Monaghan, 1989). Since the number of interacting particles near the walls is decreased, the accuracy of numerical scheme degrades. Another treatment was proposed by Campbell (1989) where the boundary condition was included in (2.15) through the residual boundary term. Today, the most often used boundary conditions are based on dummy particles (Lee et al., 2008; Shao and Lo, 2003). They are regularly distributed on the boundaries (to satisfy the impermeability condition) and have prescribed velocity (no-slip condition). In ISPH, the Poisson equation (2.40) is also solved on these dummy particles to repulse the fluid. To prevent inconsistency between the density of inner particles and that of the wall, additional layers of dummy particles are placed outside the flow domain. Other popular, virtual-particle based boundary conditions utilise so-called mirror particles. These particles are given the prescribed velocity to assure the proper boundary condition. Yet, their properties are not integrated in time, unlike those of real SPH particles. Nowadays, there are two commonly used mirror-particle approaches, differing by the way the inner particle velocities are projected on fixed boundary particles (Morris et al., 1997; Yildiz et al., 2008).

The mirror-particle techniques, presented above, have been further developed to another, more natural approach, i.e., the ghost particle method (Cummins and Rudman, 1999). This technique is similar to the well-known Classic Image Problem in electrostatics. To any particle a located at \mathbf{r}_a near the straight and infinite boundary, we introduce the image a' of this particle located at

$$\mathbf{r}_{a'} = 2\mathbf{d} + \mathbf{r}_a \quad (2.47)$$

where \mathbf{d} is the vector pointing from the particle a to the nearest point at the wall, cf. Fig. 2.1(a). Since a chosen kernel is compact, the boundary may be finite. The role of these particles is to assure a high accuracy of the computation (to remedy for the lack of particles near the boundaries) and to enforce the boundary condition for the field quantities. For velocity, the natural way to obtain the proper implementation of the no-slip wall boundary condition is to set:

$$\mathbf{u}_{a'} = 2\mathbf{u}_w - \mathbf{u}_a, \quad m_{a'} = m_a, \quad \rho_{a'} = \rho_a, \quad (2.48)$$

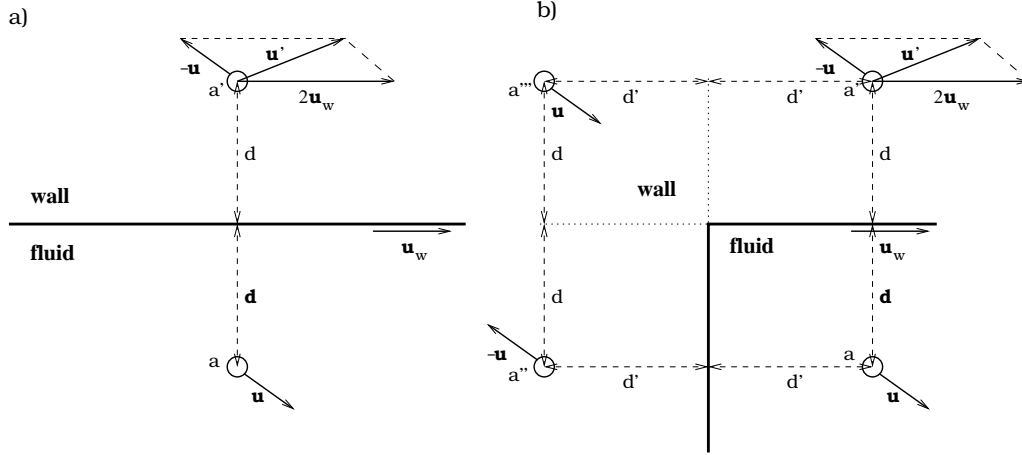


Figure 2.1: The ghost-particle no-slip boundary scheme: a) straight wall, b) inner corner ($\alpha = 0$).

where \mathbf{u}_w is the velocity of the boundary. To enforce the proper Neumann boundary condition for the pressure

$$\frac{\partial p}{\partial n} = 0, \quad (2.49)$$

where \mathbf{n} is the vector normal to the boundary, we extend the set (2.48) by an approximation of (2.49)

$$p_{a'} = p_a. \quad (2.50)$$

Let \mathbf{r}_w stand for a position of any point placed at the boundary. Due to the kernel symmetry we have

$$W(\mathbf{r}_w - \mathbf{r}_a, h) = W(\mathbf{r}_w - \mathbf{r}_{a'}, h). \quad (2.51)$$

Now, utilising the SPH summation interpolant (2.13) for velocity, we write

$$\begin{aligned} \langle \mathbf{u} \rangle(\mathbf{r}_w) &= \sum_a \frac{m_a}{\rho_a} \mathbf{u}_a W(\mathbf{r}_w - \mathbf{r}_a, h) + \sum_{a'} \frac{m_{a'}}{\rho_{a'}} \mathbf{u}_{a'} W(\mathbf{r}_w - \mathbf{r}_{a'}, h) = \\ &= 2\mathbf{u}_w \sum_a \frac{m_a}{\rho_a} W(\mathbf{r}_w - \mathbf{r}_a, h). \end{aligned} \quad (2.52)$$

Since the summation in the above equation is over fluid particles only, assuming nearly homogeneous distribution of fluid particles, we have

$$\sum_a \frac{m_a}{\rho_a} W(\mathbf{r}_w - \mathbf{r}_a, h) = \sum_{a'} \frac{m_{a'}}{\rho_{a'}} W(\mathbf{r}_w - \mathbf{r}_{a'}, h) \approx \frac{1}{2} \quad (2.53)$$

and (2.52) becomes

$$\langle \mathbf{u} \rangle(\mathbf{r}_w) \approx \mathbf{u}_w. \quad (2.54)$$

Therefore, (2.48) provides the proper formulation of the no-slip wall condition.

Another boundary type that can be treated with the ghost-particle approach is the inner corner. The technique of constructing particle images is presented in Fig. 2.1(b). In this case we use three mirror particles. It is important to note that the influence range of this corner is smaller than $2h$. For a larger distance from the

corner, the boundary condition boils down to the previous case (both in vertical and horizontal directions). For the distances smaller than $2h$, Cummins and Rudman (1999) use the third mirror particle placed symmetrically with respect to the corner point

$$\mathbf{r}_{a'} = 2\mathbf{d} + \mathbf{r}_a, \quad \mathbf{r}_{a''} = 2\mathbf{d}' + \mathbf{r}_a, \quad \mathbf{r}_{a'''} = 2\mathbf{d} + 2\mathbf{d}' + \mathbf{r}_a, \quad (2.55)$$

possessing the same density and mass

$$\rho_a = \rho_{a'} = \rho_{a''} = \rho_{a'''}, \quad m_a = m_{a'} = m_{a''} = m_{a'''}, \quad (2.56)$$

but opposite velocity to the fluid particle

$$\mathbf{u}_{a'} = 2\mathbf{u}_w - \mathbf{u}_a, \quad \mathbf{u}_{a''} = -\mathbf{u}_a, \quad \mathbf{u}_{a'''} = \mathbf{u}_a. \quad (2.57)$$

Yet, in the case of moving boundary, the resulting velocity vector computed at the corner is neither $\mathbf{0}$ nor \mathbf{u}_w . Therefore, to find a more accurate approach, we parametrise the mirror particles' velocity as follows (using the notation from Fig. 2.1):

$$\mathbf{u}_{a'} = 2\alpha\mathbf{u}_w - \mathbf{u}_a, \quad \mathbf{u}_{a''} = -\mathbf{u}_a, \quad \mathbf{u}_{a'''} = 2\alpha\mathbf{u}_w + \mathbf{u}_a, \quad (2.58)$$

where α may change from -1 up to 1 . Now, for a point \mathbf{r}_w at the boundary, we carry similar investigation as in (2.52)

$$\begin{aligned} \langle \mathbf{u} \rangle(\mathbf{r}_w) &= \sum_a \frac{m_a}{\rho_a} \mathbf{u}_a W(\mathbf{r}_w - \mathbf{r}_a, h) + \sum_{a'} \frac{m_{a'}}{\rho_{a'}} \mathbf{u}_{a'} W(\mathbf{r}_w - \mathbf{r}_{a'}, h) \\ &+ \sum_{a''} \frac{m_{a''}}{\rho_{a''}} \mathbf{u}_{a''} W(\mathbf{r}_w - \mathbf{r}_{a''}, h) + \sum_{a'''} \frac{m_{a'''}}{\rho_{a'''}} \mathbf{u}_{a'''} W(\mathbf{r}_w - \mathbf{r}_{a'''}, h) \\ &= 2\mathbf{u}_w \sum_a \frac{m_a}{\rho_a} [W(\mathbf{r}_w - 2\mathbf{d} - \mathbf{r}_a, h) + \alpha W(\mathbf{r}_w - 2\mathbf{d} - 2\mathbf{d}' - \mathbf{r}_a, h)]. \end{aligned} \quad (2.59)$$

For a point placed exactly at the corner, the above formula reduces to the form

$$\langle \mathbf{u} \rangle(\mathbf{r}_c) \approx \frac{1}{2} \mathbf{u}_w (1 + \alpha). \quad (2.60)$$

Depending on the value of parameter α , the velocity of the corner changes from $\mathbf{u}(\mathbf{r}_c) = \mathbf{0}$ (for $\alpha = -1$) up to $\mathbf{u}(\mathbf{r}_c) = \mathbf{u}_w$ (for $\alpha = 1$). Despite this parametrisation, there is no way to assure proper velocity at boundary points closer than $2h$ from the corner. This issue is presented in Fig. 2.2. Yet, the simulations of various test problems show that varying the parameter α does not have a significant impact on the global (except near the corner) velocity or density fields. In the present work, we utilise the no-slip condition (2.58) with $\alpha = 0$.

Another problem with the no-slip condition appears during computation of density in WCSPH utilising the continuity equation (2.19). Assuming a statistically homogeneous distribution of particle positions, the tangential velocity component at the boundary is negligible for computing the divergence. Therefore, along straight boundaries the no-slip condition is properly stated. The problem appears near the corners. Using (2.16), we compute the divergence of velocity at the boundary near the corner

$$\begin{aligned} \langle \nabla \cdot \mathbf{u} \rangle(\mathbf{r}_w) &= \sum_a \frac{m_a}{\rho_a} \mathbf{u}_a \cdot \nabla_a W(\mathbf{r}_w - \mathbf{r}_a, h) + \sum_{a'} \frac{m_{a'}}{\rho_{a'}} \mathbf{u}_{a'} \cdot \nabla_{a'} W(\mathbf{r}_w - \mathbf{r}_{a'}, h) \\ &+ \sum_{a''} \frac{m_{a''}}{\rho_{a''}} \mathbf{u}_{a''} \cdot \nabla_{a''} W(\mathbf{r}_w - \mathbf{r}_{a''}, h) + \sum_{a'''} \frac{m_{a'''}}{\rho_{a'''}} \mathbf{u}_{a'''} \cdot \nabla_{a'''} W(\mathbf{r}_w - \mathbf{r}_{a'''}, h). \end{aligned} \quad (2.61)$$

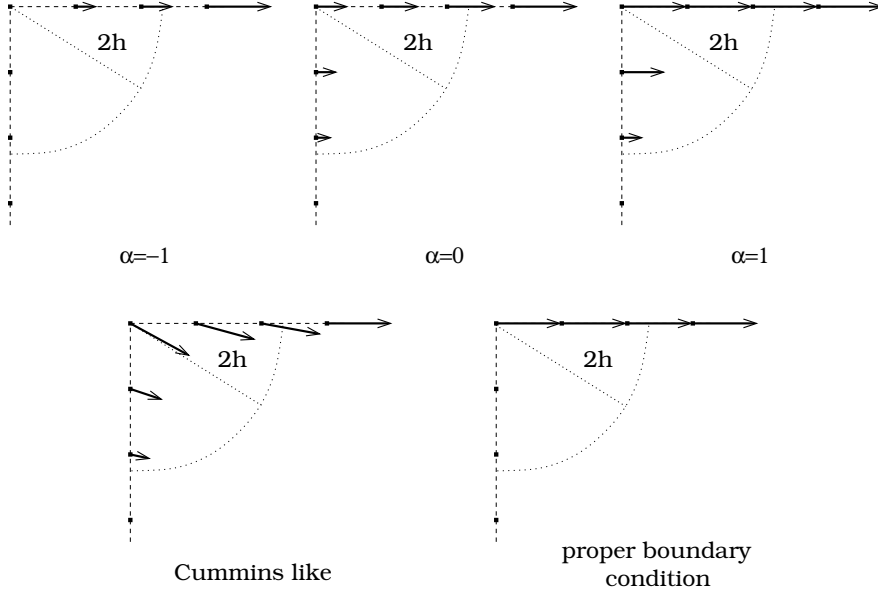


Figure 2.2: The problem with the ghost-particle no-slip boundary condition near the corner: depending on value of the parameter α , the velocity boundary condition changes.

For the point at the corner \mathbf{r}_c we have

$$\begin{aligned} \nabla_\alpha W(\mathbf{r}_c - \mathbf{r}_a, h) \cdot \mathbf{n}_x &= \nabla_{a'} W(\mathbf{r}_c - \mathbf{r}_{a'}, h) \cdot \mathbf{n}_x = \\ &= -\nabla_{a''} W(\mathbf{r}_c - \mathbf{r}_{a''}, h) \cdot \mathbf{n}_x = -\nabla_{a'''} W(\mathbf{r}_c - \mathbf{r}_{a'''}, h) \cdot \mathbf{n}_x \end{aligned} \quad (2.62)$$

and

$$\begin{aligned} \nabla_\alpha W(\mathbf{r}_c - \mathbf{r}_a, h) \cdot \mathbf{n}_y &= -\nabla_{a'} W(\mathbf{r}_c - \mathbf{r}_{a'}, h) \cdot \mathbf{n}_y = \\ &= \nabla_{a''} W(\mathbf{r}_c - \mathbf{r}_{a''}, h) \cdot \mathbf{n}_y = -\nabla_{a'''} W(\mathbf{r}_c - \mathbf{r}_{a'''}, h) \cdot \mathbf{n}_y, \end{aligned} \quad (2.63)$$

where \mathbf{n}_x and \mathbf{n}_y are unit vectors in x and y directions respectively. Therefore, connecting the above relations with (2.58) and (2.61) we obtain

$$\langle \nabla \cdot \mathbf{u} \rangle(\mathbf{r}_c) \approx 0. \quad (2.64)$$

Let us consider the situation where fluid particles are driven to the corner. To prevent penetrating the boundary, there should appear a repulsive force near this corner. In WCSPH this is done by a local density increase. However, since the divergence of velocity is always close to zero near the corner, according to the continuity equation (2.19), the density does not change. Unfortunately, with this implementation we observed a growth of velocity instabilities near the corners (see Fig. 2.3). Therefore, only for computing the divergence of velocity, we suggest to use the free-slip condition. For a straight boundary, cf. Fig. 2.4, the free-slip mirror particle is placed at $\mathbf{r}_{a'} = 2\mathbf{d} + \mathbf{r}_a$. It has the same mass and density, its velocity component normal to the boundary is opposite, while the tangential component is unchanged. Near the corner, cf. Fig. 2.4(b), the mirror particles are placed in the same position

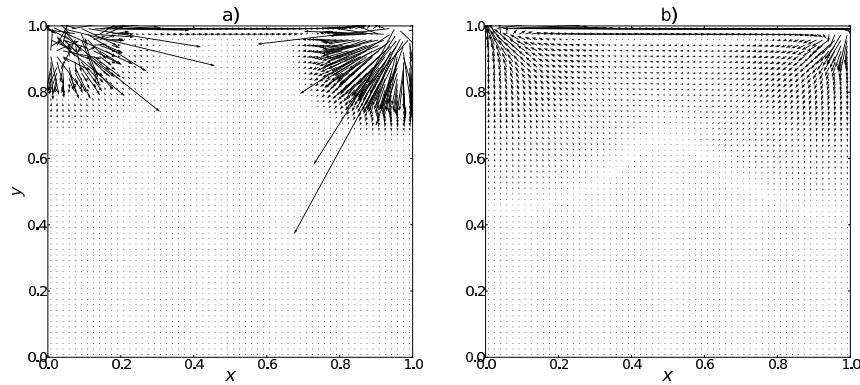


Figure 2.3: The WCSPH results of two-dimensional lid-driven cavity ($Re = 1000$) at $t = 0.03$ with: a) the no-slip and b) the free-slip boundary treatment for velocity divergence computation; employing no-slip condition induces instabilities near the corners.

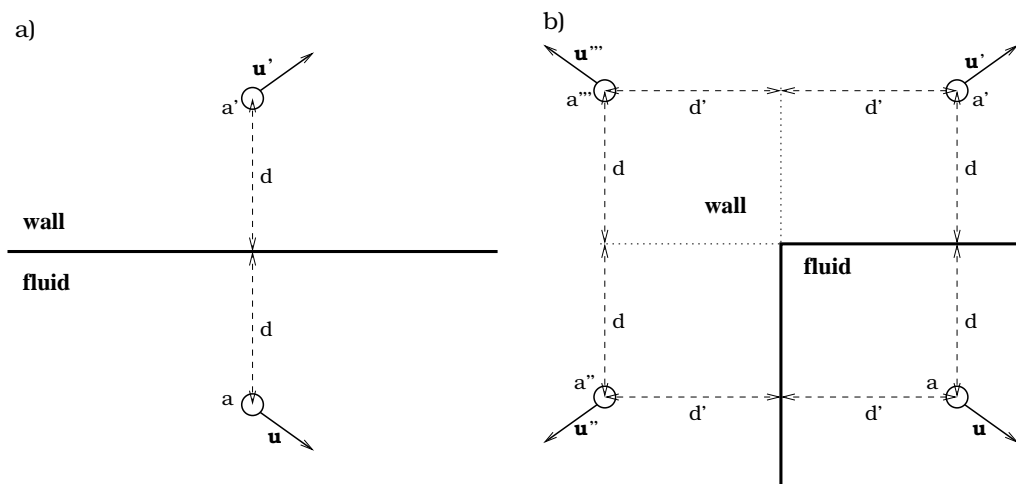


Figure 2.4: The ghost-particle free-slip boundary treatment for: a) the straight wall and b) the corner.

as in the case of no-slip condition (2.55), while they carry the following properties:

$$\begin{aligned} \mathbf{u}_{a'} \cdot \mathbf{n}_x &= \mathbf{u}_a \cdot \mathbf{n}_x, & \mathbf{u}_{a'} \cdot \mathbf{n}_y &= -\mathbf{u}_a \cdot \mathbf{n}_y, \\ \mathbf{u}_{a''} \cdot \mathbf{n}_x &= -\mathbf{u}_a \cdot \mathbf{n}_x, & \mathbf{u}_{a''} \cdot \mathbf{n}_y &= \mathbf{u}_a \cdot \mathbf{n}_y, \\ \mathbf{u}_{a'''} \cdot \mathbf{n}_x &= -\mathbf{u}_a \cdot \mathbf{n}_x, & \mathbf{u}_{a'''} \cdot \mathbf{n}_y &= -\mathbf{u}_a \cdot \mathbf{n}_y. \end{aligned} \quad (2.65)$$

Obviously, the kind of boundary treatment presented here is basically limited to flat wall segments only; more advanced formulations exist and represent the state of the art for arbitrarily-shaped boundaries, e.g., Feldman and Bonet (2007). However, since the main focus of Chapter 3 is on incompressibility treatments, we have chosen simple geometry cases to have enough reference data.

2.6 Hydrostatic pressure computation

The hydrostatic pressure p_{hs} at depth H can be calculated according to the relation (2D)

$$p_{\text{hs}}(x, H) = \int_0^H \rho(x, y) g dy + p_{\text{ref}}, \quad (2.66)$$

where p_{ref} is a reference pressure. The above integral can not be straightforwardly solved in SPH since the particles (nodes), carrying information about density, move in the domain. Only for single-phase flows, Eq. (2.66) can be simplified to the relation

$$p_{\text{hs}} = \rho_0 g H + p_{\text{ref}}, \quad (2.67)$$

so that the total numerical cost is to determine H . The hydrostatic pressure can be also calculated jointly with the dynamic pressure using the equation of state (2.36) (Crespo, 2008; Monaghan, 1994). The crucial point is to provide the proper sound speed c . Particles are assigned an initial density ρ resulting from pressure at a given depth H

$$\rho = \rho_0 \left(1 + \frac{\rho_0 g (H - y)}{B} \right)^{\frac{1}{\gamma}}, \quad (2.68)$$

where $B = c^2 \rho_0 / \gamma$. This approach is very commonly used for simulations of single-phase flows in hydro-engineering (eg. dam-breaking, sloshing problems).

However, in the case of flows of variable density, cf. Sect. 7.3, as well as for multiphase flows, the above mentioned procedures of computing the hydrostatic force are not straightforward to implement. Therefore, to perform explicit integration of Eq. (2.66), we resigned from a fully Lagrangian description. We decided to use an auxiliary regular mesh with a suitably chosen number of cells, cf. Fig. 2.5. Each cell contains several particles. The mean density in the cell (i, j) (i horizontal, j vertical direction) is equal to the average over all particles $N_{i,j}$ in this cell

$$\rho_{i,j}^{\text{cell}} = \frac{1}{N_{i,j}} \sum_{a \in \text{cell}(i,j)} \rho_a. \quad (2.69)$$

Afterwards, in accordance with Eq. (2.66), we compute the pressure at the bottom (S) of each cell and simultaneously $p_{i,j}^S = p_{i,j-1}^N$, taking advantage of the discretisation

$$p_{i,j}^S = p_{\text{ref}} + \sum_{k>j} \rho_{i,k}^{\text{cell}} g \Delta y_{i,j}, \quad (2.70)$$

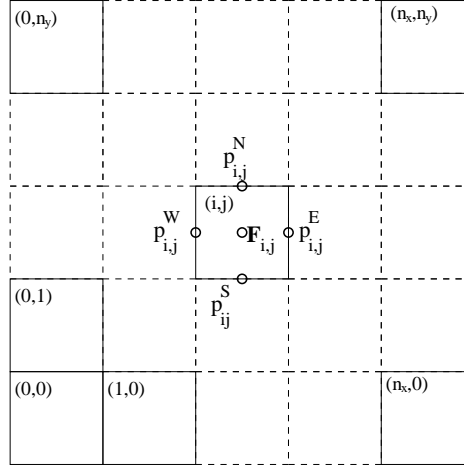


Figure 2.5: An auxiliary mesh for computing the hydrostatic force.

where $\Delta y_{i,k}$ is the height of cell (i,j) . The pressure values at the centres of cell sides are computed by averaging pressures at the bottom and top of neighbouring cells. In the next step, the pressure obtained using Eq. (2.70) is interpolated at the particle positions, and then, after adding the dynamical pressure, computed with the standard SPH form. However, in that approach, to assure proper gradient at the top and bottom walls, some modifications of boundary conditions are necessary.

Alternatively, there exists another formulation. The hydrostatic force can be computed at the center of cells (cf. Fig. 2.5)

$$\mathbf{F}_{i,j} = \frac{1}{\rho_{i,j}^{\text{cell}}} \left[\frac{\partial p}{\partial x}, \frac{\partial p}{\partial y} \right]_{i,j} = \frac{1}{\rho_{i,j}^{\text{cell}}} \left[\frac{p_{i,j}^E - p_{i,j}^W}{\Delta x_{i,j}}, \frac{p_{i,j}^N - p_{i,j}^S}{\Delta y_{i,j}} \right]. \quad (2.71)$$

Then, the calculated force can be projected at the particles using the bi-linear interpolation scheme. Numerical experiments show that there is no vital difference between both approaches.

Chapter 3

Assessment of the SPH approaches¹

3.1 Introduction

An important issue in SPH is the proper account of the incompressibility constraint. In this chapter, three different variants are critically discussed and compared for a selection of validation examples. The first one is the Weakly Compressible SPH (WCSPH) approach, which is the most common technique, used from the beginning of SPH. It involves the standard set of governing equations closed by a suitably-chosen, artificial equation of state, cf. Sect. 2.3.1. The second and third variants, called truly incompressible SPH (ISPH), are based on the Projection Method, introduced in SPH by Cummins and Rudman (1999). Generally in ISPH, a Poisson equation is solved to obtain the divergence-free velocity field. In the second approach, this Poisson equation is solved on an auxiliary regular mesh (Pozorski and Wawreńczuk, 2002), as described in Sect. 2.3.2. Here, this method is called the Grid-based Poisson Solver (GPS). Since this approach consists in combining the Eulerian and Lagrangian techniques, it is not an optimal choice for free-surface and multi-phase flows; yet, due to the computational efficiency, its usefulness seems to be worth of discussion. The third approach considered is the ISPH scheme with the Particle-based Poisson Solver (PPS), cf. Sect. 2.3.2. In this variant, first proposed in Cummins and Rudman (1999), the Poisson equation is rewritten in SPH formulation and solved on the grid of Lagrangian points (particles). The main advantage of this idea is that the additional domain discretisation and related discretisation errors are avoided.

The first part of the chapter is related to the work of Lee (2007) and Lee et al. (2008, 2010), where a similar comparison between WCSPH and ISPH-PPS approaches was done. However, in the present work, a comprehensive analysis of boundary conditions is performed. Moreover, since we use the same (ghost-particle) boundary conditions (cf. Sect. 2.5) for both WCSPH and ISPH approaches, our comparison offers a new look at the usefulness of the incompressibility variants. Some

¹The original material presented in this chapter has been published as: K. Szewc, J. Pozorski, J-P. Minier, ‘Analysis of the incompressibility constraint in the SPH method’, *Int. J. Numer. Methods Eng.* **92** (2012) 343-369.

work along these lines has recently been performed by Hughes and Graham (2010), but, their comparison was limited to single-phase free-surface flows only. It is also interesting to note that Lee et al. (2008) and Hughes and Graham (2010) reached apparently opposite conclusions on the advantage of one of the incompressibility treatments.

In the present work, for the sake of validation for both single- and two-phase flows, the three different variants of the incompressibility constraint are compared for the lid-driven cavity flow (2D and 3D), the Rayleigh-Taylor instability (2D) and the cube-to-sphere droplet deformation case (3D). For the first case, the impact of various computational parameters on the results has been analysed and an optimal setting has been found; it is consequently used also for other cases considered. To accurately simulate multiphase cases with the WCSPH approach, the Colagrossi and Landrini (2003) N-S pressure (2.33) and continuity equation forms (2.26) were used, cf. Chapter 4. In the case of the ISPH approaches we used Eq. (2.26) as the N-S pressure term, while the divergence of velocity was calculated from formula

$$\langle \nabla \cdot \mathbf{u} \rangle_a = - \sum_b \frac{m_b}{\rho_b} \mathbf{u}_{ab} \cdot \nabla_a W_{ab}(h). \quad (3.1)$$

An extensive comparison of ISPH solvers was presented by Xu et al. (2009). However, the authors do not discuss the problem of density errors accumulation in the ISPH approach. Since, like other authors (Cummins and Rudman, 1999; Hu and Adams, 2007), we have been faced with such a problem, we decided to examine the usefulness of the correction algorithm proposed by Pozorski and Wawreńczuk (2002), cf. Sect. 3.6. This formulation, used also in the PDF computations of turbulent flows (Minier and Pozorski, 1999), consists in retrieving the constant fluid density field by applying the correction to the particle positions. In practice, that method involves a second Poisson equation. The improvement of results in some cases is clearly demonstrated and the effectiveness of such an approach is discussed.

3.2 Lid-driven cavity (2D)

Two-dimensional lid-driven cavity is a common test of numerical algorithms for viscous flows. It involves a fluid at density ρ_0 inside a square ($L \times L$) box where only one boundary moves with the constant velocity \mathbf{u}_w , cf. Fig. 3.1. The geometry is very simple, however there is no analytical solution. In the present work, we computed the lid-driven cavity flow at $Re = |\mathbf{u}_w|L/\nu = 1000$. For this value of Reynolds number the flow is still laminar and there is no necessity to use a turbulence model. All variables are suitably non-dimensionalised with L , $|\mathbf{u}_w|$ and ρ_0 ; in particular, time is normalised with the convective time scale $L/|\mathbf{u}_w|$. Flow results are compared to those from a numerical calculation on a fine grid performed with the Eulerian solver by Ghia et al. (1982).

3.2.1 The kernel type influence

One of the important issues that have an impact on the SPH solutions is a proper selection of the kernel. To compare the treatments of the incompressibility

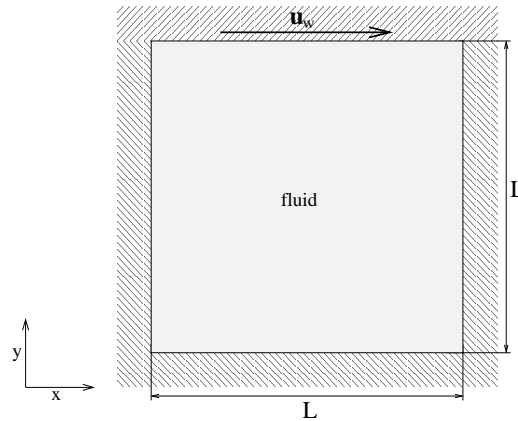


Figure 3.1: A scheme of a lid-driven cavity.

constraint, we decided to perform the benchmark simulation of the lid-driven cavity flow with the three kernels presented in Sect. 2.1. The particles' number has been chosen with two requirements: N should be large enough to get solutions comparable to reference data; however, it should be sufficiently small to show kernels' defects. We decided to use $N = 3600$ particles in the domain and $h/\Delta r = 2$, where Δr is a measure of the inter-particle distance, cf. Sect. 3.2.2. The steady-state velocity profiles are presented in Fig. 3.2. As seen, the results obtained with the cubic spline kernel are the most inconsistent with the reference data. This discrepancy is caused by the particles' clustering.

It is commonly known that increase of irregularities in particle distribution causes an increase of numerical errors in SPH. Sweagle et al. (1995) pointed out that the clustering phenomenon is not caused by the time integration scheme, but it corresponds to the tensile instability resulting from the interaction between the constitutive relation and the kernel function properties. To avoid the problem, Monaghan (2000) proposed to use an extra artificial stress in the pressure term. Another remedy, consisting in remeshing on a fine grid, was proposed by Chaniotis et al. (2002). However, in this approach, similarly to ISPH-GPS, the method lost the advantages of being mesh-free. Yet another technique to avoid the particle clustering (in ISPH approaches) was proposed by Xu et al. (2009). It consists in slightly shifting particles away of streamlines and interpolating on them the hydrodynamic variables by the Taylor series. This procedure leads to redistribute particles in a more uniform manner. The particle clustering is very common issue in structural mechanics. To avoid it, Dyka and Ingel (1995) and, later, Randles and Libersky (2000) introduced stress points into SPH. This technique stabilises SPH by suppressing spurious singular modes. However, in our simulations, we are not using any of the above methods.

Figs. 3.3 and 3.4 respectively present the particle spatial distribution and histograms of the distance between the nearest pairs of particles for all kernels considered. As it transpires from the histogram for the cubic spline kernel, in this case there are many particles that move joined in groups, cf. also details in Fig. 3.3; as a consequence, the accuracy of the scheme is decreased. As far as the quintic kernels are concerned, both perform similarly to each other. However, the kernel

proposed by Morris et al. (2.10) shows a more pronounced tendency to clustering (Fig. 3.4); moreover, it is not zero up to $|\mathbf{r}|/h = 3$ (as contrasted to $|\mathbf{r}|/h = 2$ for the other kernels), so it involves many more particles. Therefore, the computational time is increased about 12% comparing to the Wendland kernel. Summarising, due to a good agreement with the reference data, not noticeable clustering phenomenon, and finally the efficiency, for further analysis we decided to use the quintic Wendland kernel. An interesting work about its behaviour in SPH has recently been performed by Robinson (2009) (Ch. 7).

3.2.2 The kernel size influence

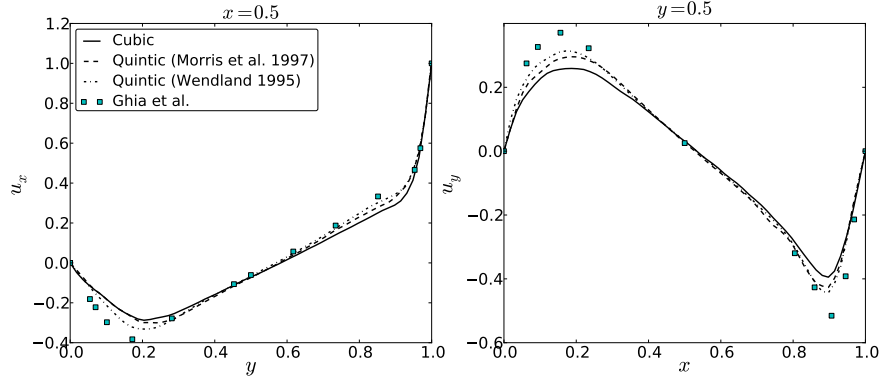
Apart from the initial inter-particle distance Δr (related to the number of particles in the domain), in the SPH approach there exists another characteristic length - the kernel parameter h . Examining the impact on the solutions, we decided to compute 2D lid-driven cavity problem ($Re = 1000$) for chosen $N = 3600$, the Wendland kernel and different $h/\Delta r$ values that determine the number of particles under the kernel hat. Figure 3.5 presents the velocity profiles for $h/\Delta r = 2.31, 2.0, 1.67$ and 1.5 computed with all the SPH incompressibility variants. Lower values of $h/\Delta r$ may cause inaccuracy of interpolates (too few particles). On the other hand, higher values of $h/\Delta r$ have a strong impact on computational time, since the number of interacting particles grows like $\sim (h/\Delta r)^D$, where D is the space dimension. Judging from the comparison to the reference data (Ghia et al., 1982), there is no significant effect of the kernel size on the velocity field. Only for $h/\Delta r < 2$ a small influence of this parameter can be observed. Pondering between the computational times and accuracy, we decided to use $h/\Delta r = 2$ for all simulations presented henceforth.

3.2.3 The particle number influence

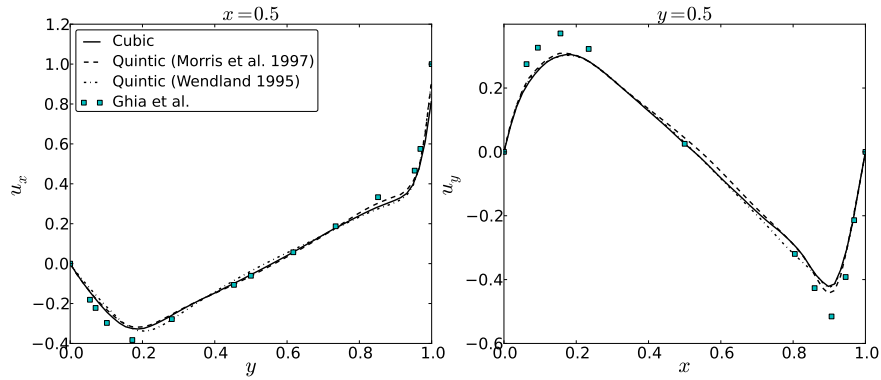
Examining the influence of the spatial resolution, the simulations were performed with a different number of particles in the domain (from $N = 1600$ up to $N = 57600$). The steady-state velocity profiles are presented in Fig. 3.6. In all the methods of incompressibility treatment, the profiles obtained for $N = 1600$ did not agree very well with the Ghia et al. (1982) solution obtained on 129×129 Eulerian mesh. Performing simulations with the higher resolutions, the accuracy increases so that in the case of $N = 14400$, independently of the compressibility treatment, the obtained results are already in very good agreement with the reference data. For $N = 57600$ the velocity profiles computed using WCSPH and ISPH-PPS approaches practically overlap with those from Ghia et al. (1982). The ISPH-GPS solution is less accurate. This deficiency is due to a higher numerical diffusion caused by the projection of the quantities from particles on a regular grid and subsequent interpolation of pressure on particles.

Due to the utilisation of the equation of state and the time step constraint in WCSPH, the CPU time of the lid-driven cavity simulation (not-parallelised) computed by the ISPH-PPS is about 7 times shorter for $N = 3600$; however, this difference in CPU time decreases steadily with increasing number of particles. Performing the ISPH-GPS simulations, the computational effort may be reduced another order of magnitude with respect to ISPH-PPS. The comparison of CPU times for all

(a) WCSPH



(b) ISPH-GPS



(c) ISPH-PPS

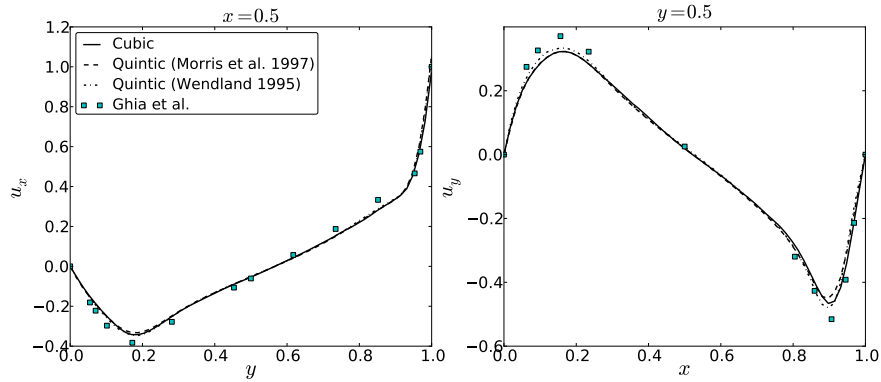


Figure 3.2: The lid-driven cavity (2D) steady-state velocity profiles for: (a) WCSPH, (b) ISPH-GPS and (c) ISPH-PPS against Ghia et al. (1982) results; profiles obtained for different kernels; $N = 3600$, $h/\Delta r = 2$.

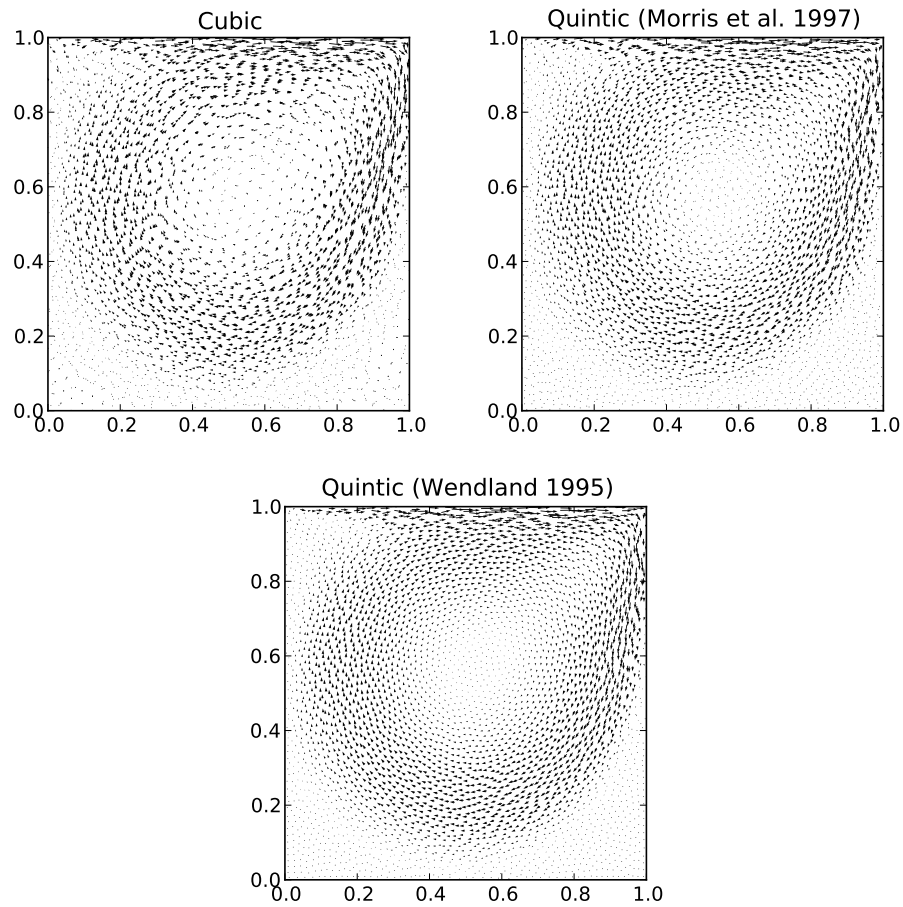


Figure 3.3: The lid-driven cavity (2D) steady-state velocity ($Re = 1000$, $N = 3600$) computed with the WCSPH approach and kernels: (2.9)–(2.11); the particle clustering is noticeable with the cubic spline kernel.

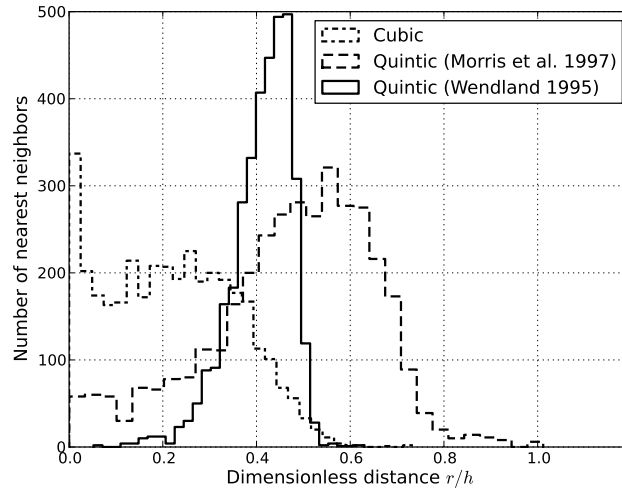


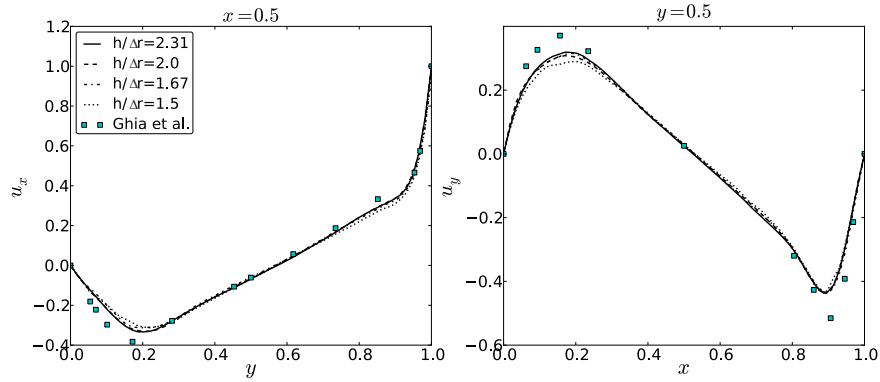
Figure 3.4: Histograms of the distance between the nearest pairs of particles; the results obtained for the WCSPH approach and kernels: (2.9)–(2.11).

considered SPH schemes is presented in Fig. 3.7(a). On the other hand, worth of discussing is the growth of needed memory as a function of N , cf. Fig. 3.7(b). Since the Poisson equation in the ISPH-PPS approach consists in solving a linear equation system with a sparse irregular coefficient matrix (of size $N \times N$), this method requires much more memory than the other approaches. This explains the decreasing difference between WCSPH and ISPH-PPS computational time when the number of particles grows. There is much more intense memory-processor communication and, additionally, some CPU time is spent on sparse matrix management.

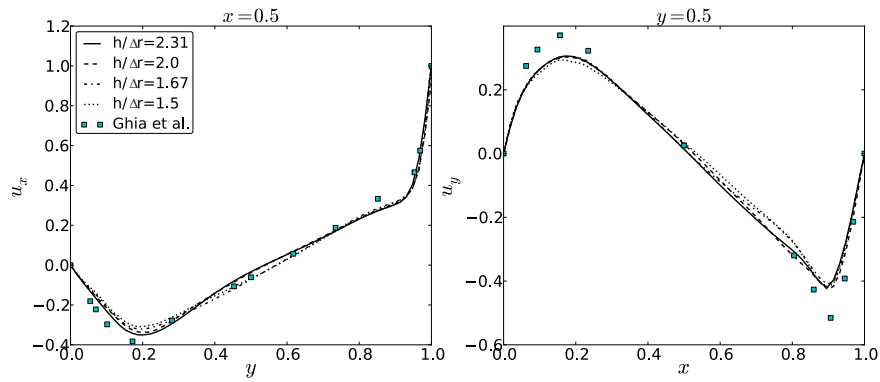
3.3 Lid-driven cavity (3D)

Three-dimensional extension of the previously discussed lid-driven cavity test is one of the most commonly used for validation purposes of algorithms for 3D viscous flows. It involves a fluid at density ρ_0 inside a cube of side L . Only one boundary moves with a constant velocity \mathbf{u}_w in its plane (in our case $\mathbf{u}_w = [u_w, 0, 0]$). As in 2D case there is no analytical solution. Moreover, as previously, we decided to stay in the laminar regime ($Re = 100$). To compare the incompressibility treatments, we performed the SPH simulations with $N = 216000$ particles ($60 \times 60 \times 60$), $h/\Delta r = 2$ and the Wendland kernel. The solutions are presented in Fig. 3.8. All results are suitably non-dimensionalised in the same way as in 2D case and compared to data obtained using Eulerian solvers by Shu et al. (2003) (Differential Quadrature) and Lo et al. (2005) (Finite Difference Method). The solutions obtained with the WCSPH and ISPH-PPS approaches agree very well with the reference data. Unfortunately, ISPH-GPS results seem to be much less accurate. The main reason is an additional numerical diffusion related to the projection of physical quantities on grid. On the other hand, in case of such a large number of particles, the disadvantage of the ISPH-PPS method starts to be the large amount of data that need to be kept during

(a) WCSPH



(b) ISPH-GPS



(c) ISPH-PPS

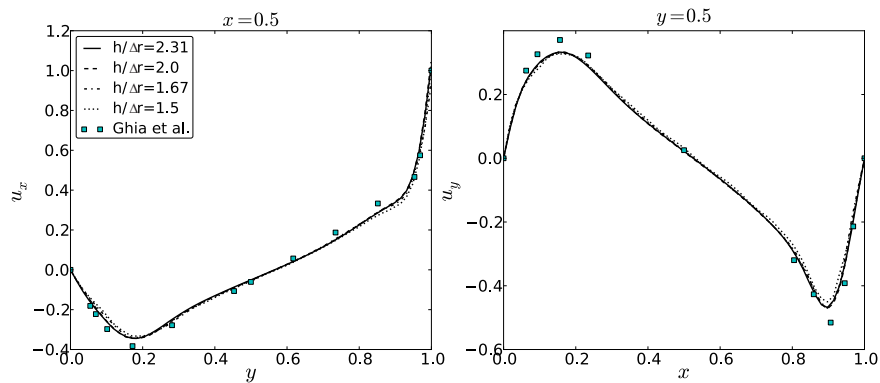
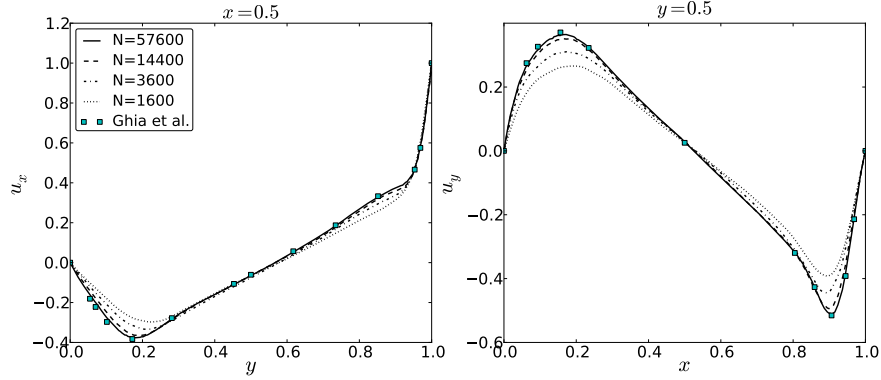
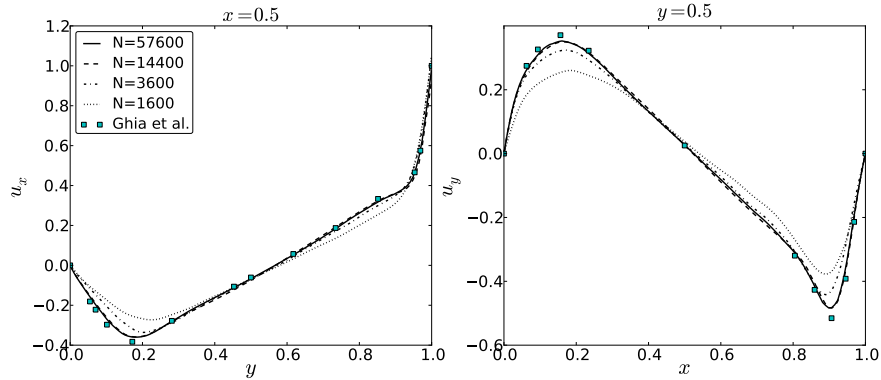


Figure 3.5: The lid-driven cavity (2D) steady-state velocity profiles for: (a) WCSPH, (b) ISPH-GPS and (c) ISPH-PPS against Ghia et al. (1982) reference data; results obtained with different $h/\Delta r$ values using the Wendland (1995) kernel and $N = 3600$ particles in domain.

(a) WCSPH



(b) ISPH-GPS



(c) ISPH-PPS

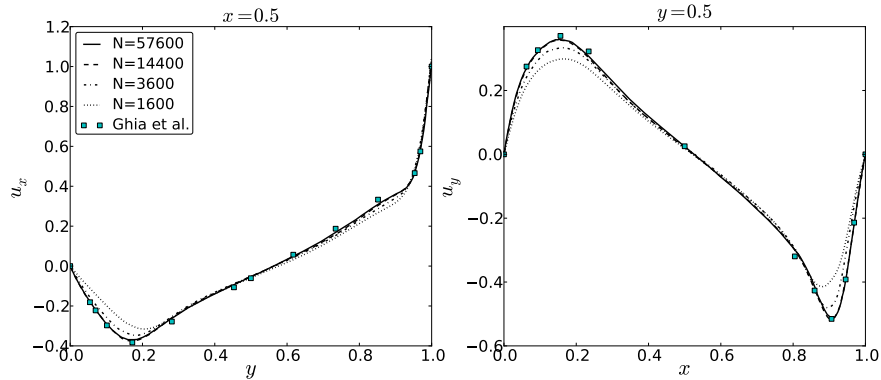


Figure 3.6: The lid-driven cavity (2D) steady-state velocity profiles for: (a) WCSPH, (b) ISPH-GPS and (c) ISPH-PPS against Ghia et al. (1982) reference data; results for different number of particles N , the Wendland (1995) kernel and $h/\Delta r = 2$.

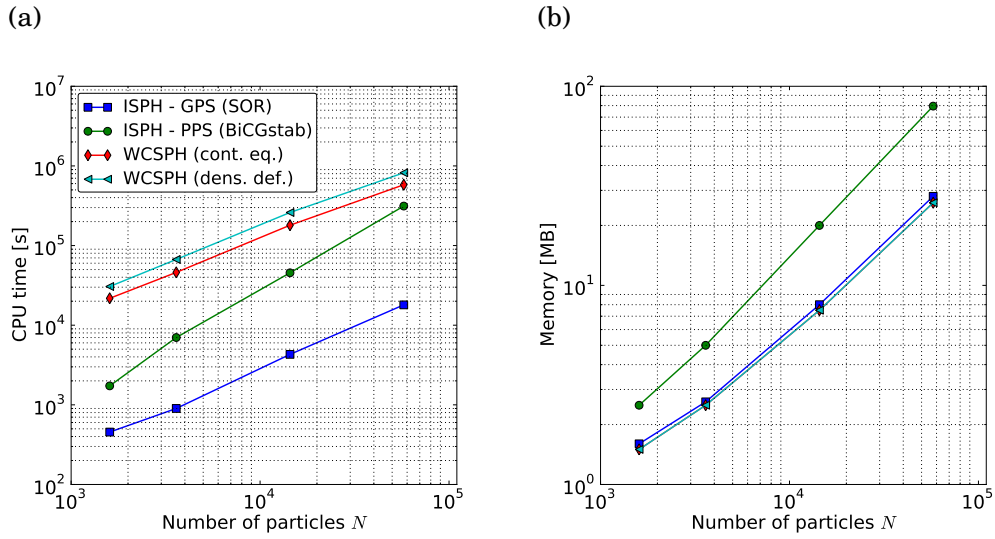


Figure 3.7: The CPU times (non-parallelized) and memory needed to obtain the steady-state solution of two-dimensional lid-driven cavity ($Re = 1000$) using the WCSPH and both ISPH approaches; for the WCSPH method, the continuity equation (2.24) is compared to the density definition (2.28).

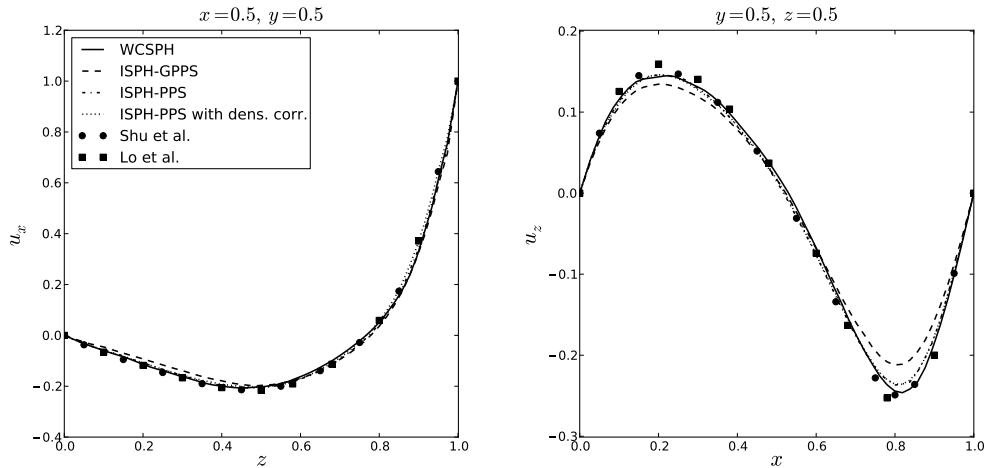


Figure 3.8: The lid-driven cavity (3D) steady-state velocity profiles at $Re = 100$ computed using WCSPH, ISPH-GPS, ISPH-PPS, and ISPH-PPS with density correction procedure (cf. Sect. 3.6) against Shu et al. (2003) and Lo et al. (2005).

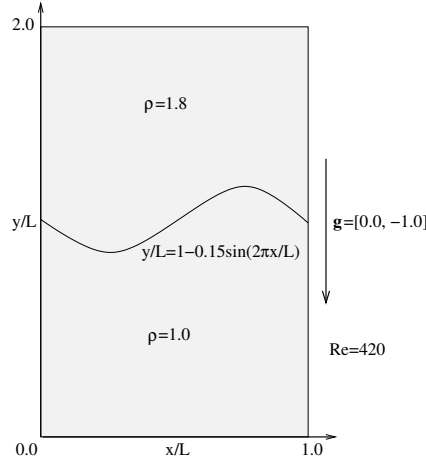


Figure 3.9: A scheme of the Rayleigh-Taylor instability test case.

the simulation (about 2GB), mainly for the linear solver (the Poisson equation). In our simulations it had a strong impact on the computational time (communication and thread synchronisation). The simulations, parallelized to 6-threads on AMD FX-8120 processor, took respectively: 80 h for WCSPH, 55 h for ISPH-PPS and 12 h for ISPH-GPS. Increasing further the number of particles, WCSPH seems to be more promising.

3.4 The Rayleigh-Taylor instability (2D)

The Rayleigh-Taylor instability is one of generic multiphase flows, therefore it is commonly utilised as a test problem. It involves two immiscible fluids enclosed in a rectangular domain of width L and height $2L$, cf. Fig. 3.9. Initially, in our case, the phases are separated by the interface located at $y/L = 1 - 0.15 \sin(2\pi x/L)$. The lower component has density $\rho_L = \rho_0$, while the upper one $\rho_U = 1.8\rho_0$. Since the system is subject to gravity $\mathbf{g} = (0, -g)$ and the upper phase is heavier, in the absence of the surface tension an instability always arises and vorticity is generated. The Reynolds number may be defined as

$$Re = \frac{\sqrt{L^3 g}}{\nu} = 420. \quad (3.2)$$

The simulations were performed for 120×240 particles in the domain. To compute the hydrostatic force, we use the technique described in Szewc et al. (2011), where the hydrostatic pressure is computed on a regular mesh and later projected on the particles. Figure 3.10 presents particle positions (directly showing the location of the liquid-liquid interface) computed with different treatments of the incompressibility condition. All the simulations are compared to the reference solutions from the Level-Set method (312×624 cells) computed by Grenier et al. (2009). Presented data were obtained at $t = 5$ (normalised with the convective time scale $\sqrt{L/g}$).

Comparing the interface shapes, we find no convincing arguments to judge which SPH approach is more accurate. However, the comparison of the computational

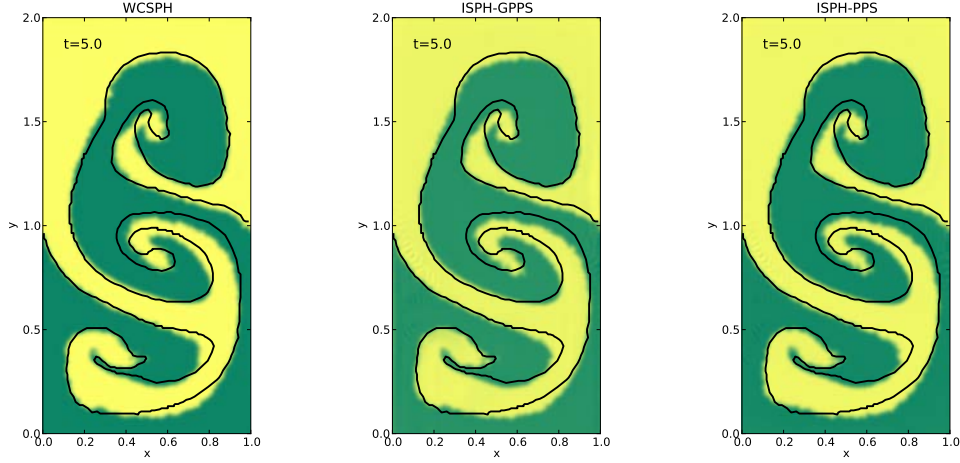


Figure 3.10: The Rayleigh-Taylor instability; particle positions at $t = 5$ obtained using different incompressibility treatments; colours show the location of the phases calculated by SPH; solid line shows position of liquid-liquid interface from the reference Level-Set solution (Grenier et al., 2009).

times shows that the most efficient choice is the ISPH-GPS. The ISPH-PPS is slower about 6 times, while the WCSPH about 13 times.

3.5 Density error estimation

In order to measure the density errors, we compute two quantities: the mean density over the flow domain $\bar{\rho}(t)$ and the root mean square of the density fluctuations $\rho_{\text{rms}}(t)$. However, since in the Projection Methods the values of the density carried by particles do not change, it is necessary to use formulae which are able to compute $\bar{\rho}(t)$ and $\rho_{\text{rms}}(t)$ taking into account both the density values and spatial distribution of the particles. The simplest proposals (expressed as the SPH formulae) are: for the mean density

$$\bar{\rho}(t) = \frac{1}{N} \sum_a m_a \sum_b W_{ab}(h), \quad (3.3)$$

and for the density fluctuations $\rho_{\text{rms}}(t)$

$$\rho_{\text{rms}}(t) = \sqrt{\frac{1}{N} \sum_a \left(m_a \sum_b W_{ab} - \bar{\rho}(t) \right)^2}. \quad (3.4)$$

In WCSPH, comparing the influence of the kernel shape, we observe that the quintic kernel proposed by Wendland (2.11) gives the smallest fluctuations of the density field, cf. Fig. 3.11(a). The weakness of the Wendland kernel is a slight overestimation of the mean density. Even for a homogeneously distributed set of particles (at $t = 0$) the density field is flawed, cf. discussion in (Hongbin and Xin, 2005). The decrease of the $h/\Delta r$ parameter causes this error to grow from 0.2% for

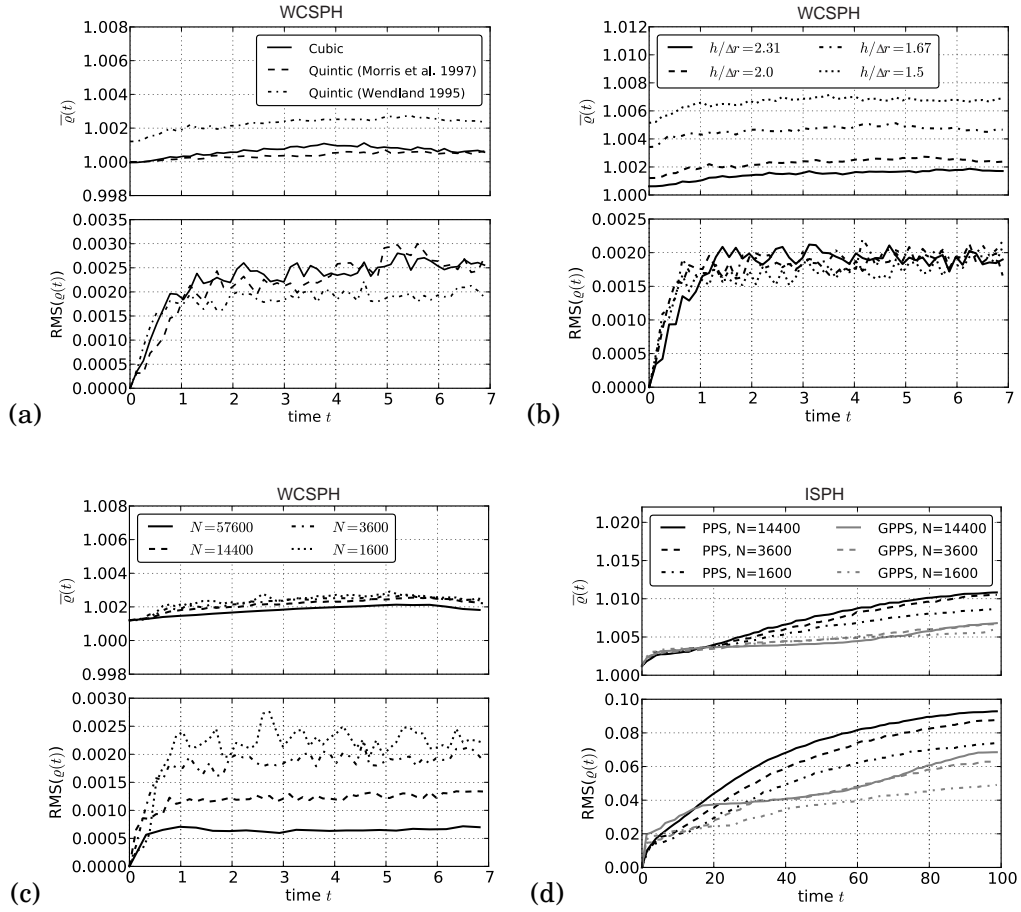


Figure 3.11: The density mean value and the r.m.s. obtained for the lid-driven cavity (2D) flow at $Re = 1000$; the effect of: (a) the kernel choice, (b) $h/\Delta r$, (c) the number of particles N in the WCSPH approach; (d) the particle number N in both ISPH-PPS and ISPH-GPS techniques.

$h/\Delta r = 2.31$ up to about 0.8% for $h/\Delta r = 1.5$, cf. Fig. 3.11(b). Interestingly, the parameter $h/\Delta r$ has no significant effect on $\rho_{\text{rms}}(t)$. The impact of the particle number N on $\bar{\rho}$ and ρ_{rms} , obtained with WCSPH, is presented in Fig. 3.11(c). The density r.m.s., independently on the number of particles in domain, stabilises after about $t = 1$ and remains less than 1% of initial density. Moreover, with increasing N the density r.m.s. goes down. In the case of ISPH solvers, the growth of the r.m.s. stops only after obtaining the steady-state solution (roughly at $t = 120$), cf. Fig. 3.11(d). Intriguing is the fact that for the ISPH approach, ρ_{rms} increases with the number of particles. For ISPH-PPS the r.m.s. of the steady-state solution changes: from 7% for $N = 1600$ up to 9% for $N = 14400$. For ISPH-GPS the density field is additionally affected by the projections between the particles and the grid. These projections cause additional smoothing and the density field r.m.s. of the steady-state solution varies: for $N = 1600$ about 6%, $N = 3600$ about 6% and $N = 14400$ about 7% of initial density.

In the case of the Rayleigh-Taylor instability (cf. Fig. 3.12) and 3D lid-driven cavity (figure not shown), the comparison of density errors shows similar behaviour

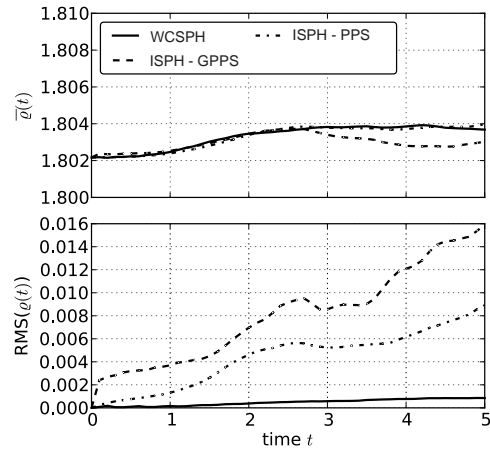


Figure 3.12: The density mean value and the r.m.s. obtained for the Rayleigh-Taylor instability (only the upper phase of $\rho_U = 1.8\rho_0$) using WCSPH and both ISPH approaches.

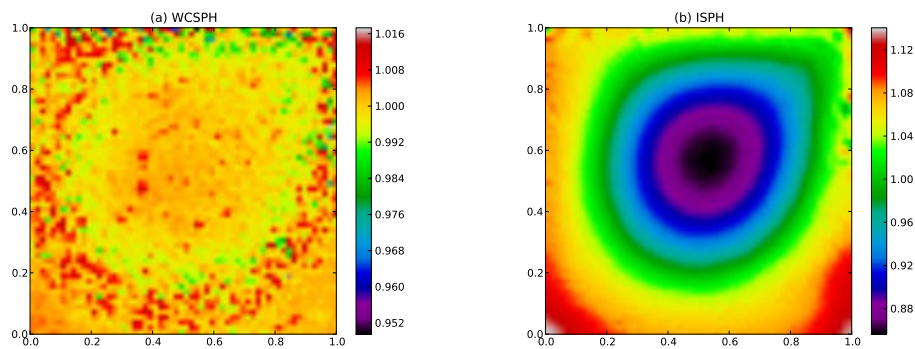


Figure 3.13: The lid-driven cavity (2D) flow: density field at the steady-state solution.

as in the case of 2D lid-driven cavity.

This discrepancy between WCSPH and ISPH density error values is caused by the completely different mechanisms of computing the dynamical pressure in the Navier-Stokes equation. Since in the case of the WCSPH approach the suitably-chosen equation of state is used, the density field exhibits short-scale density waves presented in Fig. 3.13(a). In the case of ISPH, particles move with the velocity projected onto a divergence-free space to achieve (2.20), but there is no constraint to assure that particles move at the ‘correct’ positions to assure homogeneous distribution and, therefore, constant density. This is the reason why, during the computations, the density field strongly deviates from the level of the initial state, cf. Fig. 3.13(b). Since the Projection Methods give such considerable density errors, it is meaningful to conceive an additional correction procedure, cf. Sect. 3.6. Distorted density field can have a big impact on accuracy of simulations (cf. Sect. 3.7.1).

3.6 Incompressible SPH with density correction

In the previous section we have shown that in the ISPH approach the density errors accumulate during computations. To solve this problem, Pozorski and Wawreńczuk (2002) suggested to apply the second correction (a similar approach was later proposed, in the multi-phase flow context, by Hu and Adams (2007)). Let us consider incompressible fluid with initially uniform density $\rho_0(\mathbf{r}) = \rho_0$. After the time step performed with the ISPH approach, the corrected velocity field \mathbf{u}^{n+1} satisfies the divergence-free condition; however, this procedure does not explicitly guarantee that $\rho(\mathbf{r}) = \text{const}$. The idea of Pozorski and Wawreńczuk consists in performing an additional correction to the particle positions

$$\mathbf{r}_a^{n+1} = \tilde{\mathbf{r}}_a^{n+1} - \frac{1}{\rho_0} \nabla p_a^* = \mathbf{r}_a^n + \mathbf{u}_a^{n+1} \delta t - \frac{1}{\rho_0} \nabla p_a^*, \quad (3.5)$$

where \mathbf{u}_a^{n+1} and $\tilde{\mathbf{r}}_a^{n+1}$ are respectively the divergence-free velocity field and particle positions obtained after the ISPH time step, Eqs. (2.38) and (2.40), while p_a^* appears as a correction field computed from

$$\frac{1}{\rho_0} \nabla \cdot \left(\frac{\rho^n}{\rho_0} \nabla p^* \right) = 1 - \frac{\tilde{\rho}^{n+1}}{\rho_0}, \quad (3.6)$$

where $\tilde{\rho}^{n+1}$ is the density obtained after the ISPH time step; both ρ^n and $\tilde{\rho}^{n+1}$ are computed using Eq. (2.28). The Poisson Eq. (3.6) is obtained from the request that

$$\rho^{n+1}(\mathbf{r}) = \sum_b m_b W(\mathbf{r} - \mathbf{r}_b^{n+1}, h) = \sum_b m_b W\left(\mathbf{r} - \tilde{\mathbf{r}}_b^{n+1} + \frac{1}{\rho_0} \nabla p_b^*, h\right) = \rho_0(\mathbf{r}), \quad (3.7)$$

and then applying the Taylor series expansion around $\mathbf{r} - \tilde{\mathbf{r}}_b^{n+1}$ (\mathbf{r} denotes any point in the flow domain).

Since, performing such a correction, the second Poisson equation has to be solved, the computational effort is increased. However, in practice, the correction is applied only if the density error exceeds a certain threshold value. Usually, there is no necessity to compute the correction at each time step; on the other hand, in some cases, the procedure may need to be performed iteratively several times in one time

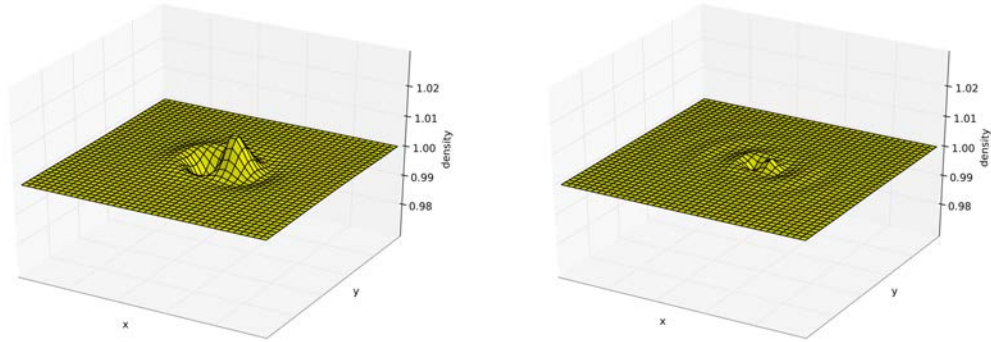


Figure 3.14: The density field with local disturbance; left: the initial state (regular set of particles with one particle displaced), right: after 50 correction iterations.

step. Figure 3.14 shows how an initial disturbance of the density field (a regular set of particles with one particle displaced) is corrected with (3.6).

To solve the test problems, we decided to utilise ISPH-PPS with particle positions correction performed once per time step. Since both Poisson equations are solved on particles, we have a fully grid-free approach. The velocity profiles of 2D lid-driven cavity problem ($Re = 1000$) are presented in Fig. 3.15. There are no noticeable differences between the velocities obtained using ISPH solver with (Fig. 3.15) and without (Fig. 3.6) the density correction. However, comparing the density fields, cf. Fig. 3.16, with the results obtained without the density correction, cf. Figs. 3.11, 3.12 and 3.13(b), the advantages of this approach become obvious: the growth of the r.m.s. density stops after $t = 5$ and stays at a level less than 0.1%. The regularisation of the particles' distribution is also visible in the histograms of the distance to the nearest neighbour of each particle: the comparison of histograms for ISPH-PPS with and without the correction procedure is presented in Fig. 3.17. Another convincing argument for the utility of the Pozorski and Wawreńczuk approach is the computational effort. As in the case of WCSPH, the density error does not accumulate, and, despite the use of two Poisson solvers, the computational time (for $N = 14400$) is about 3 times shorter (and about 2 times longer than ISPH-PPS), so the use of the density correction algorithm seems to be still profitable. However, this approach still requires a large amount of available memory, and, therefore, it is of limited use for very large numbers of particles. On the other hand, it is interesting to note a higher convergence rate with increasing number of particles in domain, as compared to the solutions obtained by Lee et al. (2008) (Fig. 6) and Xu et al. (2009) (Fig. 25). We suppose that a better convergence rate in our case is due to an optimal choice of computational parameters ($h/\Delta r$, kernel type and b.c.).

For the Rayleigh-Taylor instability, the calculated particle positions at times $t = 1, 3$ and 5 are presented in Fig. 3.18. The comparison with the reference interface shapes (Grenier et al., 2009) shows quite a good agreement. What is more, there are no considerable differences between ISPH with and without the density correction term. Moreover, as in the case of the lid-driven cavity, the use of such a correction assures that the density error (Fig. 3.16) is kept below the desired level and the computational time is still acceptable (in comparison with WCSPH). Similar

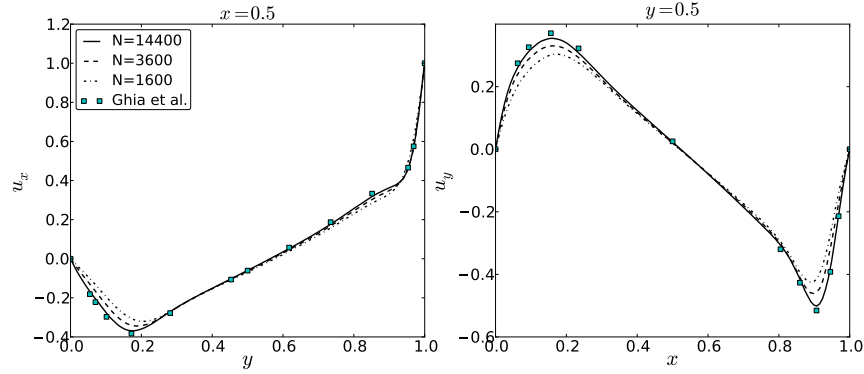


Figure 3.15: The lid-driven cavity (2D) velocity profiles at the steady-state against Ghia et al. (1982) reference data ($Re = 1000$); results obtained using ISPH with PPS and the density correction (Pozorski and Wawreńczuk, 2002) for the Wendland (1995) kernel, $h/\Delta r = 2$ and different number of particles N .

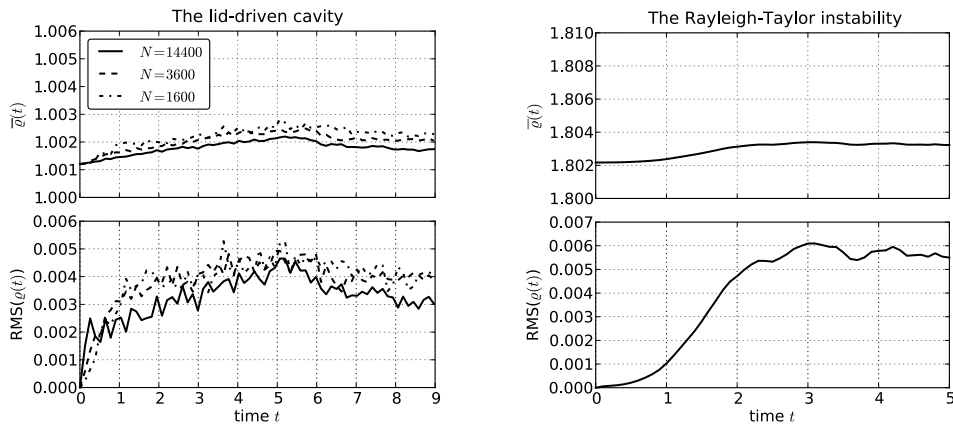


Figure 3.16: The density mean value and r.m.s. obtained using the ISPH approach with PPS and the density correction (Pozorski and Wawreńczuk, 2002); (a) 2D lid driven cavity ($Re = 1000$), (b) the Rayleigh-Taylor instability ($Re = 420$); the results obtained for the Wendland (1995) kernel and $h/\Delta r = 2$.

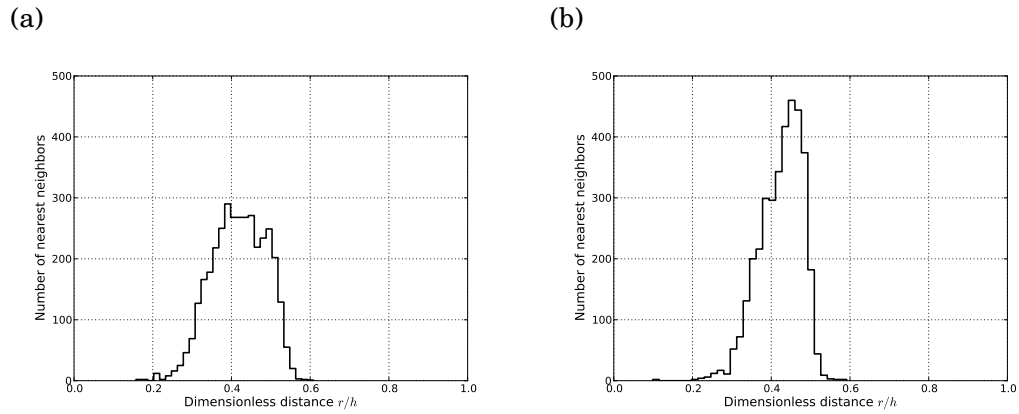


Figure 3.17: Histograms of the distance between the nearest pairs of the particles; the results obtained for the ISPH-PPS approach (a) without and (b) with the density correction procedure.

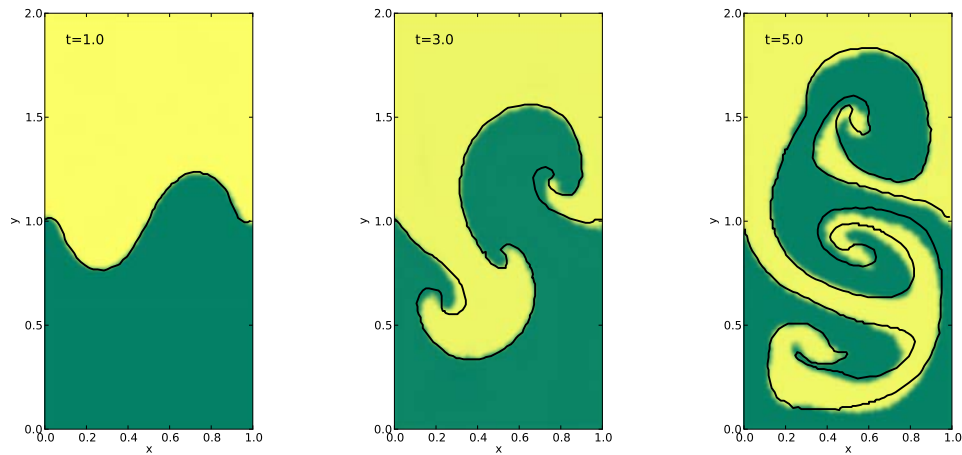


Figure 3.18: The Rayleigh-Taylor instability ($Re = 420$): ISPH-PPS with density correction (Pozorski and Wawreńczuk, 2002); the black lines denote the interface position obtained from the Level-Set computation (312×624 cells) (Grenier et al., 2009).

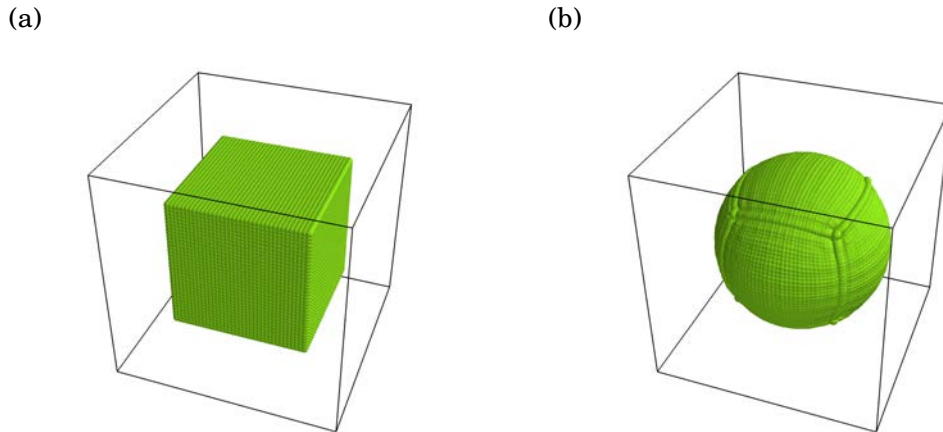


Figure 3.19: Particle distribution (only the inner phase) of the cube-to-sphere deformation test: (a) the initial state, (b) the steady-state solution obtained with the CSF method (Brackbill et al., 1992; Morris, 2000).

situation occurs in the case of three-dimensional lid-driven cavity. Velocity field is undistorted (cf. Fig. 3.8), while the density field corrected.

3.7 The need to use the density correction procedure

The main advantage of the ISPH approach is the lack of time step constraint (the CFL condition, Eq. 2.43) due to speed of sound, and thus, the possibility of using longer time steps. Of course, the CPU time required in ISPH to advance the solution by a time step is longer than in WCSPH. However, we have shown that for the lid-driven cavity cases, the ISPH approach is more efficient for the number of particles considered. Generally, this result is not always true. In many situations, when the flow is governed by forces that have a higher impact on the admissible time step than the sound speed constraint, the ISPH method may become inefficient. Such a situation occurs for very viscous fluids or for flows governed by the surface-tension phenomena.

3.7.1 Cube-to-sphere droplet deformation (3D)

The simplest three-dimensional flow case governed by surface-tension phenomena is the cube-to-sphere droplet deformation. It involves a cubical box of fluid with the edges of length L containing the inner phase of centred cubical volume of another fluid of the edges $a = 0.6L$.

The density of both phases is ρ and the viscosity coefficient ν . The influence of surface tension is described by the Weber number, $We = \rho a u^2 / \sigma$ (where σ is the surface tension coefficient, while u is a characteristic velocity), whereas the capillary number, $Ca = \rho \nu u / \sigma$, accounts also for viscosity. Here, we chose $Ca^2 / We = \nu^2 \rho / a \sigma = 2/30$. The capillary number, based on the maximum velocity in the domain, is about 0.45. Since the surface tension is present, the initially cubical volume of the inner phase ultimately takes the spherical shape, cf. Fig. 3.19. From the Laplace law the

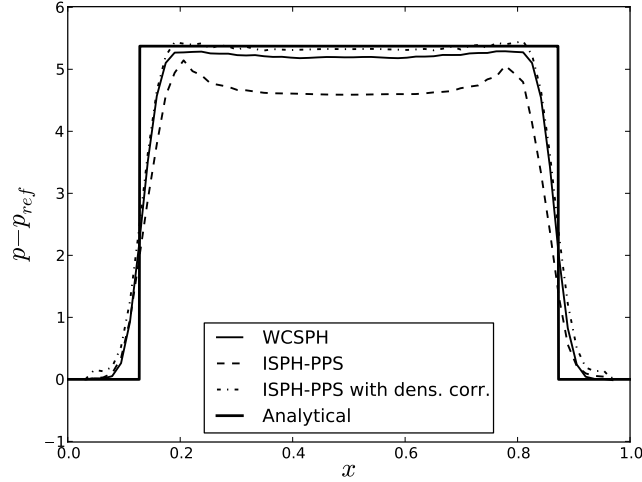


Figure 3.20: The cube-to-sphere deformation test: the computed pressure profiles at the steady-state solution (against the analytical solution).

pressure inside the formed droplet must be higher than in the surrounding fluid and should undergo a jump across the interface

$$\Delta p = \sqrt[3]{\frac{4\pi}{3} \frac{2\sigma}{a}}. \quad (3.8)$$

For modelling the surface-tension phenomena we use the Continuum Surface Force (CSF) technique (Brackbill et al., 1992; Morris, 2000), cf. Chapter 5. The simulation was performed with $N = 216000$ particles ($60 \times 60 \times 60$), $h/\Delta r = 2$ and the Wendland kernel using WCSPH, ISPH-GPS, ISPH-PPS, and ISPH-PPS with density correction procedure. Unfortunately, the ISPH-GPS method did not converge to the final, spherical shape. However, this outcome was expected: because of the used projection of the quantities between particles and mesh this approach is not suitable for modelling sharp pressure discontinuities. For other variants of incompressible SPH, the steady-state pressure profiles are presented in Fig. 3.20. This result clearly indicates the necessity of using the density correction procedure for ISPH.

The cube-to-sphere droplet deformation case has been chosen to show that the ISPH method is not the best choice for many applications. The CFL condition related to the surface-tension (based on the capillary-wave phase velocity) is (Brackbill et al., 1992; Morris, 2000)

$$\delta t_\sigma \leq 0.25 \left(\frac{\rho h^3}{2\pi\sigma} \right)^{\frac{1}{2}}, \quad (3.9)$$

what for our case reduces, independently on the SPH version, to $\delta t \leq 0.0013$ (normalised with the surface tension time scale $\sqrt{\rho a^3/\sigma}$). For WCSPH $\delta t_{CFL}/\delta t_\sigma \approx 2.8$ and $\delta t_{CFL}/\delta t_\nu \approx 2.4$, while for ISPH $\delta t_{CFL}/\delta t_\sigma \approx 30$ and $\delta t_{CFL}/\delta t_\nu \approx 26$. The ISPH-PPS method with and without density correction, due to the Poisson equation com-

putations, have been slower than the WCSPH method by a factor of 9 and 5, respectively. This makes the ISPH methods less useful for this type of problems.

3.8 Conclusions

In this chapter two basic SPH incompressibility treatments (in several variants) were considered. To validate these, four flow cases were simulated: 2D lid-driven cavity at $Re = 1000$, 3D lid-driven cavity at $Re = 100$, 2D Rayleigh-Taylor instability at $Re = 420$ and 3D cube-to-sphere droplet deformation. Summarising, in comparison to the previous tests presented by Lee et al. (2008) and Xu et al. (2009), in all of the SPH incompressibility treatments the velocity field exhibits a better convergence with increasing particle number. Detailed study of the incompressibility treatments revealed some advantages and shortcomings of the approaches. The main advantage of the ISPH is a lower computational cost (than WCSPH) for considered single-phase cases. When modelling the incompressible 3D lid-driven cavity test case, the WCSPH approach reveals to be slower by a factor of around 1.5 with respect to ISPH. However, a price for this is a higher memory demand, which for large numbers of particles in the domain can lead to a loss of performance (the processor-memory communication). Moreover, due to the high memory usage in ISPH, when a larger number of cores is requested, the WCSPH approach could turn out to be more efficient (thread synchronisation for parallel simulations). Therefore, going further in the direction of increasing number of particles, more promising approach seems to be WCSPH. What is more, both the ISPH-GPS and the ISPH-PPS solvers in their original formulation suffer from the density error accumulation.

For fluid flows where to properly model the velocity field the correct density field is of importance (some such cases have been presented in the paper), an interesting alternative to WCSPH is the ISPH approach with the separate density correction (Sect. 3.6). In this approach, the density accumulation error can be kept below a specified threshold while still retaining the grid-free formulation. The particle discretisation errors influence all the flow variables, but density, which is assumed by definition. Yet, as shown in Sect. 3.7.1, the ISPH-PPS approach with double density correction, although still producing correct results, may then become inefficient for multiphase flows governed by surface tension forces or very viscous flows. It is opportune to note that, as such, none of the present ISPH approaches can be used to properly model gas-liquid flows such as a bubble rising in water, where the divergence-free condition is satisfied only for the liquid phase. Such flows can be relatively easily modelled with the WCSPH approach, where each phase is described with a different equation of state. Also, there is still the need of appropriate wall b.c. for SPH simulations in complex geometries (arbitrary shape of the boundary).

The study has also shown the importance of correct choice of computational parameters: the kernel formula W , its smoothing length h for given inter-particle distance $h/\Delta r$, and the number of particles N in the domain. The impact of those parameters on 2D results has been analysed and optimal kernel has been found (the Wendland formula, $h/\Delta r = 2$).

Chapter 4

Multiphase SPH

4.1 Introduction

One of the main advantages of the Smoothed Particle Hydrodynamics over the Eulerian approaches is that there is no need of a numerical grid. Consequently, in SPH there is no necessity to reconstruct the shape of the interface (contrary to the Eulerian approaches), since it is directly obtained from the set of computational particles. Therefore, the standard interface advection test such as Zalesak's rotating disk (Zalesak, 1979) are not necessary (the initial shape of rotating disk does not change at all) and since there is no additional numerical diffusion related to the interface handling, the volume of each phase is exactly conserved. However, in the SPH approach, there are many ways to implement key points, such as the choice of the SPH form of governing equations, treatment of the incompressibility constraint, boundary conditions or implementation of the surface-tension phenomena. The main purpose of this chapter is to propose a critical analysis of the SPH variants of governing equations to see the influence on the multiphase flow simulations. Special attention is given to the comparison of four WCSPH approaches. The first, so-called standard formulations, is based on previously mentioned symmetrical equations (2.32), (2.34) and (2.24). The other three were proposed to improve multi-phase SPH by Colagrossi and Landrini (2003), Hu and Adams (2006) and Grenier et al. (2009). It is important to note that the truly incompressible (based on the projection method) multiphase approaches (capable of flow calculations with high density ratio) also exist. However, due to the computational efficiency (cf. Chapt. 3), their usefulness is limited, and, therefore, those approaches are not discussed here. A large part of this chapter is devoted to the problem with a spurious fragmentation of the interface, which is a phenomenon not occurring in the Eulerian methods. The main reason of this phenomenon is a lack of mechanism assuring immiscibility of phases in SPH. In this chapter, in addition to the review of the remedies which are available in the literature (Colagrossi and Landrini, 2003; Das and Das, 2009; Grenier et al., 2009; Monaghan, 2012), the new variant of the correction procedure is proposed and validated.

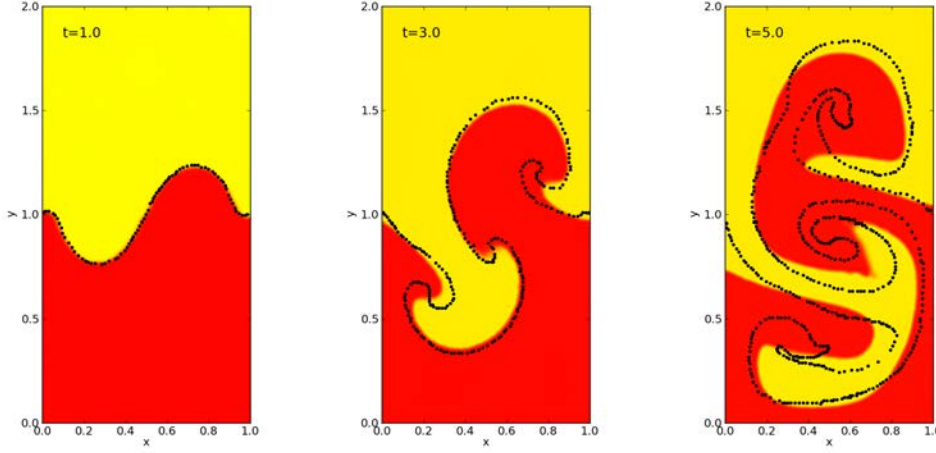


Figure 4.1: The simulations of the Rayleigh-Taylor instability at $Re = 420$; the interface position obtained with the standard SPH approach (Eqs. (2.32), (2.34), (2.24)); the black points denote the reference data computed with the Level-Set formulation (312×634 cells) (Grenier et al., 2009).

4.1.1 Standard formulation

Figure 4.1 presents the SPH simulations of the Rayleigh-Taylor instability, introduced in Sect. 3.4, compared to the Level-Set reference solutions (312×624 cells) obtained by Grenier et al. (2009). Presented data were computed at $t = 1, 3, 5$, normalised with the convective time scale $T_{\text{conv}} = \sqrt{L/g}$, and solved using Eqs. (2.32), (2.34) and (2.24), called here the standard formulation. Unfortunately, for the developed flow ($t = 5$) the SPH results are not in good accordance with the Level-Set data. This discrepancy is caused by the use of Eq. (2.32) which is derived from (2.16) using the identities

$$\rho \nabla \cdot \mathbf{u} \equiv \nabla \cdot (\rho \mathbf{u}) - \mathbf{u} \cdot \nabla \rho \quad (4.1)$$

and

$$\frac{\nabla p}{\rho} = \nabla \left(\frac{p}{\rho} \right) + \frac{p}{\rho^2} \nabla \rho. \quad (4.2)$$

Since the second r.h.s. terms of Eqs. (4.1) and (4.2) involve a computation of density gradient $\nabla \rho$, which is very high on the interface; this is a source of some instabilities affecting surroundings of the interface. Figure 4.2(left) shows the N-S pressure term calculated for one-dimensional discontinuity in density ($\rho_R/\rho_L = 2$) with non-zero pressure $p = 1$. The N-S pressure term is highly distorted close to the interface. Some early papers incorrectly describe this phenomenon as ‘artificial surface-tension’, cf. Hoover (1998).

4.1.2 Colagrossi and Landrini formulation

To solve the problem with the instabilities occurring on the interface when the standard formulation is used, Colagrossi and Landrini (2003) suggested to use another form of the N-S pressure term (cf. Sect. 2.2) proposed by Bonet and Lok (1999),

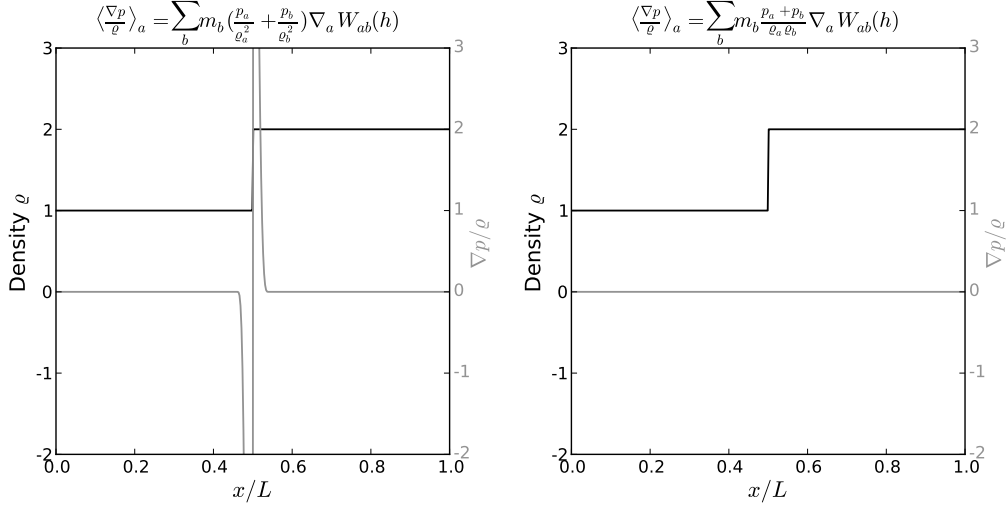


Figure 4.2: The N-S pressure term calculated for one-dimensional discontinuity in density ($\rho_R/\rho_L = 2$) with non-zero pressure $p = 1$; (left) the standard formulation, (right) the Colagrossi and Landrini (2003) formulation; $h/L = 0.02$.

cf. Eq. (2.33)

$$\left\langle \frac{1}{\rho} \nabla p \right\rangle_a = \frac{1}{\rho_a} \sum_b \Omega_b (p_a + p_b) \nabla_a W_{ab}(h), \quad (4.3)$$

as well as a different form of the continuity equation (cf. Eq. (2.26))

$$\frac{d\rho_a}{dt} = \rho_a \sum_b \Omega_b \mathbf{u}_{ab} \cdot \nabla_a W_{ab}(h). \quad (4.4)$$

Eqs. (4.3) and (4.4) are variationally consistent (Bonet and Lok, 1999; Monaghan, 2005a) and preserve linear and angular momenta. From the practical point of view, this formulation is nothing more than avoiding to compute gradients of density. Eqs. (4.3) and (4.4) are written here without explicit use of density under sum favouring the volume $\Omega_b = m_b/\rho_b$, which, assuming constant volume of particles in incompressible flow, does not change across the interface. Figure 4.2(right) shows the improvement in the quality of the N-S pressure term calculation, over the standard formulation, Fig. 4.2(left), for the case of one-dimensional discontinuity in density ($\rho_R/\rho_L = 2$) with non-zero pressure $p = 1$.

The Rayleigh-Taylor instability solution obtained with the Colagrossi and Landrini formulation is presented in Fig. 4.3. With this new approach, the SPH solutions are very close to the Level-Set data computed by Grenier et al. (2009). However, despite dealing with multi-phase flow correctly, since the Colagrossi and Landrini formalism is based on computation of velocity divergence $\nabla \cdot \mathbf{u}$, the density and velocity fields can suffer from the inconsistency, cf. Sect. 2.2. Therefore, using this approach there is a necessity to use higher order time-integration schemes.

4.1.3 Hu and Adams formulation

To construct the SPH method that deals properly with multi-phase flows and simultaneously maintains the density field consistent with others, Hu and Adams

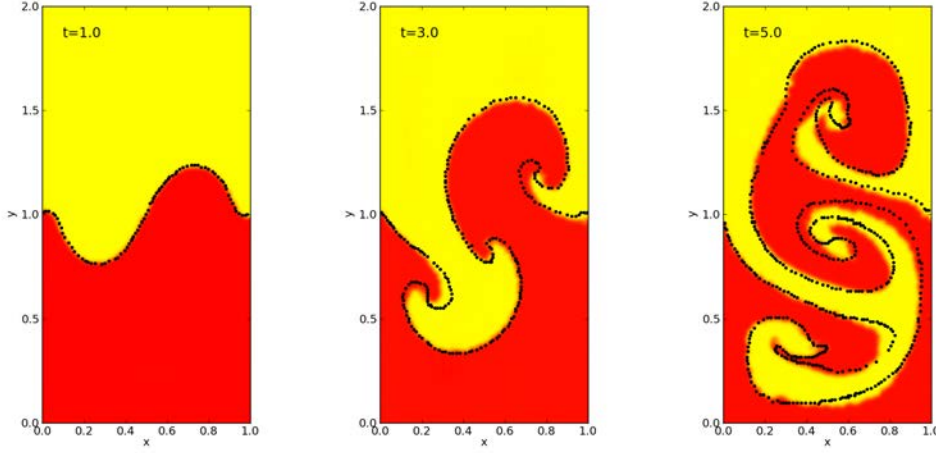


Figure 4.3: The Rayleigh-Taylor instability at $Re = 420$; the interface position obtained with the Colagrossi and Landrini (2003) formalism against the Level-Set formulation (the black points) (Grenier et al., 2009).

(2006) developed a multi-phase SPH method in which neighbouring particles only contribute to the specific volume and not to the density. Since the standard SPH approximations (2.12) and (2.16), due to particle inconsistency, cf. Liu and Liu (2006), do not allow to exactly reproduce even constant or bi-linear functions, Hu and Adams decided to use corrected, Shepard (1968) kernels in the form as the moving-least-square (MLS) approximation which reproduces a constant function explicitly (zeroth order consistency)

$$w(\mathbf{r} - \mathbf{r}_a, h) = \frac{W(\mathbf{r} - \mathbf{r}_a, h)}{\sum_b W(\mathbf{r} - \mathbf{r}_b, h)} = \frac{W(\mathbf{r} - \mathbf{r}_a, h)}{\Theta(\mathbf{r})}, \quad (4.5)$$

where $\Theta(\mathbf{r})$ is the SPH measure of particle number density. Since such a chosen function is not normalised as $W(\mathbf{r})$, cf. Eq. 2.4

$$\int_{\Omega} w(\mathbf{r} - \mathbf{r}_a, h) d\mathbf{r} = \int_{\Omega} \frac{1}{\Theta(\mathbf{r})} W(\mathbf{r} - \mathbf{r}_a, h) d\mathbf{r} = \left\langle \frac{1}{\Theta} \right\rangle_a \approx \frac{1}{\Theta_a}, \quad (4.6)$$

it is more reasonable to use particle-averaged integral approximation for the field quantities and their spatial derivatives

$$A(\mathbf{r}_a) = \Theta_a \int_{\Omega} A(\mathbf{r}) w(\mathbf{r} - \mathbf{r}_a, h) d\mathbf{r}, \quad (4.7)$$

$$\nabla A(\mathbf{r}_a) = -\Theta_a \int_{\Omega} A(\mathbf{r}) \nabla w(\mathbf{r} - \mathbf{r}_a, h) d\mathbf{r}. \quad (4.8)$$

Since $\nabla w(\mathbf{r} - \mathbf{r}_a)$ can be expressed as

$$\nabla w(\mathbf{r} - \mathbf{r}_a) = \frac{1}{\Theta(\mathbf{r})^2} \sum_b [W(\mathbf{r} - \mathbf{r}_b, h) \nabla W(\mathbf{r} - \mathbf{r}_a, h) - W(\mathbf{r} - \mathbf{r}_a, h) \nabla W(\mathbf{r} - \mathbf{r}_b, h)], \quad (4.9)$$

Eq. (4.8) can be rewritten into

$$\nabla A(\mathbf{r}_a) = -\Theta_a \sum_b \int_{\Omega} \frac{A(\mathbf{r})}{\Theta(\mathbf{r})^2} [W(\mathbf{r} - \mathbf{r}_b, h) \nabla W(\mathbf{r} - \mathbf{r}_a, h) - W(\mathbf{r} - \mathbf{r}_a, h) \nabla W(\mathbf{r} - \mathbf{r}_b, h)] d\mathbf{r}. \quad (4.10)$$

Using Eq. (2.1), and, assuming $\nabla W(\mathbf{r})$ is an odd function, the r.h.s. of the above equation can be approximated as

$$\langle \nabla A(\mathbf{r}) \rangle_a = \Theta_a \sum_b \left(\frac{A_a}{\Theta_a^2} + \frac{A_b}{\Theta_b^2} \right) \nabla_a W_{ab}(h). \quad (4.11)$$

Using the above equation to approximate the N-S pressure term we obtain

$$\left\langle \frac{\nabla p}{\varrho} \right\rangle_a = \frac{1}{m_a} \sum_b \left(\frac{p_a}{\Theta_a^2} + \frac{p_b}{\Theta_b^2} \right) \nabla_a W_{ab}(h). \quad (4.12)$$

Since, as in the cases (2.32) and (4.3), a force between two freely chosen particles is antisymmetric with swapping positions

$$\left(\frac{p_a}{\Theta_a^2} + \frac{p_b}{\Theta_b^2} \right) \nabla_a W_{ab}(h) = - \left(\frac{p_b}{\Theta_b^2} + \frac{p_a}{\Theta_a^2} \right) \nabla_b W_{ba}(h), \quad (4.13)$$

the linear and angular momentum are conserved.

To avoid the inconsistency of the density and velocity fields caused by the use of the continuity equation in form (2.19), Hu and Adams decided to take the advantage of the use of density definition. However, since the use of Eq. (2.27), which is derived from the standard SPH approximations, causes the smoothing of density field across the interface, cf. Fig. 4.4(left), which implies distortions in pressure field. Therefore, to avoid this difficulty, the authors suggested to use the modified form

$$\varrho_a = m_a \sum_b W_{ab}(h). \quad (4.14)$$

Using this approach, the sharp density discontinuities at the interface can be treated naturally, cf. Fig. 4.4(right). What is important, (4.14) is variationally consistent with (4.12), cf. Grenier et al. (2009).

The viscous N-S term is approximated using the inter-particle-averaged ($\bar{\cdot}$) shear stress in the form proposed by Flekkoy et al. (2000)

$$\bar{\Pi}_{ab} = \overline{\mu(\nabla \mathbf{u} + (\nabla \mathbf{u})^T)}_{ab} = \frac{\mu}{r_{ab}^2} (\mathbf{r}_{ab} \mathbf{u}_{ab} + \mathbf{u}_{ab} \mathbf{r}_{ab}). \quad (4.15)$$

Assuming that the interface separating phases of different viscosity is placed centrally between particles a and b , assuming continuity of shear stress and velocity across the interface, Eq. (4.15) can be written as

$$\bar{\Pi}_{ab} = \frac{2\mu_a \mu_b}{\mu_a + \mu_b} \frac{1}{r_{ab}^2} (\mathbf{r}_{ab} \mathbf{u}_{ab} + \mathbf{u}_{ab} \mathbf{r}_{ab}). \quad (4.16)$$

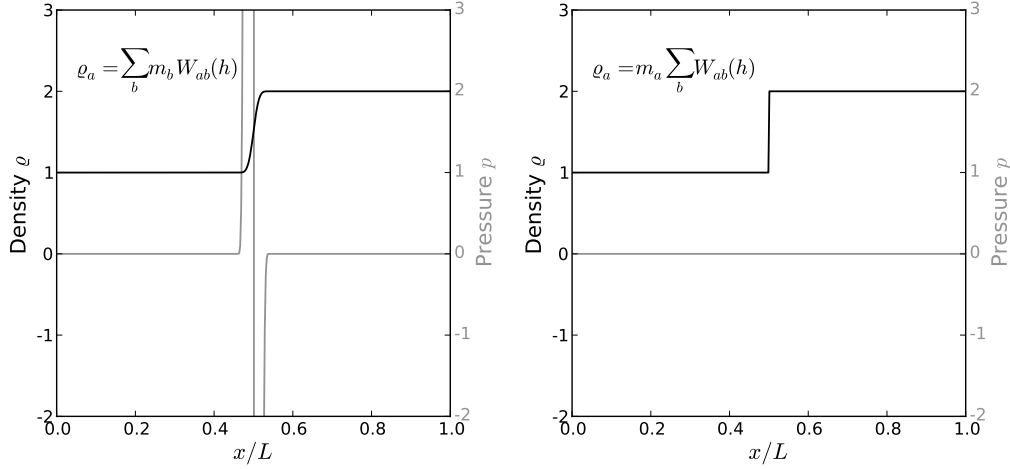


Figure 4.4: Density and pressure fields calculated for one-dimensional discontinuity in density ($\rho_R/\rho_L = 2$, $p = 0$); density field calculated using: (left) Eq. (4.14), (right) Eq. (4.14); $h/L = 0.02$.

Approximating the field $\bar{A}(\mathbf{r})$ under the integral in Eq. (4.10) by its centrally inter-particle-averaged value $\bar{A}_{ab} = (A_a + A_b)/2$, Hu and Adams obtained

$$\langle \nabla A(\mathbf{r}) \rangle_a = \Theta_a \sum_b \left(\frac{1}{\Theta_a^2} + \frac{1}{\Theta_b^2} \right) \bar{A}_{ab} \nabla_a W_{ab}(h). \quad (4.17)$$

Inserting Eq. (4.16) into a tensor form of Eq. (4.17), and, applying the incompressibility condition, the multi-phase N-S viscous term can be written as

$$\left\langle \frac{1}{\rho} (\nabla \cdot \mu \nabla) \mathbf{u} \right\rangle_a = \frac{1}{m_a} \sum_b \frac{2\mu_a \mu_b}{\mu_a + \mu_b} \left(\frac{1}{\Theta_a^2} + \frac{1}{\Theta_b^2} \right) \frac{\mathbf{r}_{ab} \cdot \nabla_a W_{ab}(h)}{r_{ab}^2 + \eta^2} \mathbf{u}_{ab}, \quad (4.18)$$

where, as in the case of Eq. (2.34), $\eta = 0.01h$ is small regularising parameter added to avoid potential singularities.

The Rayleigh-Taylor instability test performed with the Hu and Adams approach is presented in Fig. 4.5. In comparison with the Colagrossi and Landrini (2003) model, both approaches yield similar shapes of the interface. But, the Hu and Adams algorithm reproduces more details that were obtained with the Level-Set method. However, due to the use of Eq. (4.14) this approach still suffers from the deficiency of particles near free fluid surfaces. To solve this problem, Grenier et al. (2009) have proposed some extensions to the Colagrossi and Landrini approach inspired by Hu and Adams formulation.

4.1.4 Grenier et al. formulation

To allow calculations of multiphase flows with an accurate treatment of the discontinuity of quantities through the interface and, simultaneously, to simulate flows with free surfaces, Grenier et al. (2009) proposed another SPH formulation which is

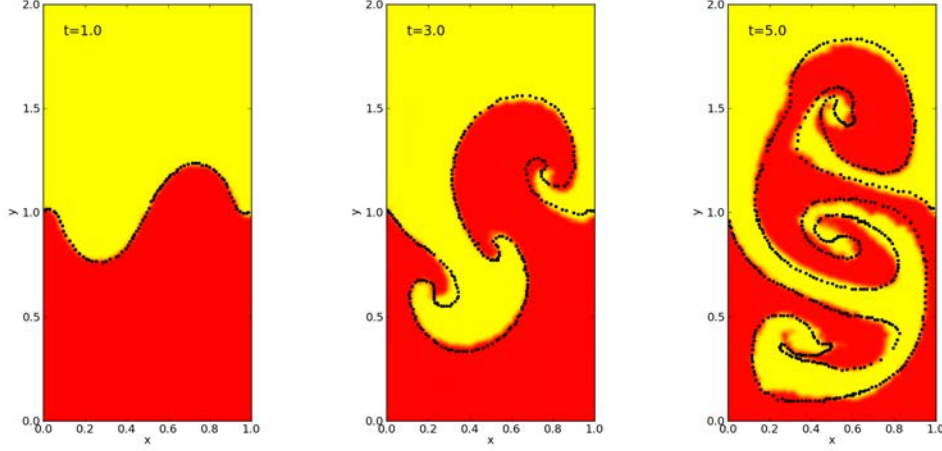


Figure 4.5: The Rayleigh-Taylor instability at $Re = 420$; the interface position obtained with the Hu and Adams (2006) formalism; the black points represent the interface with the Level-Set formulation (the black points) (Grenier et al., 2009).

based, similarly to Hu and Adams (2006), on the re-normalisation of kernels. However, Grenier et al. proposed to re-normalise it in different manner, where particles not only contribute through their geometrical distribution, cf. Eq. (4.5), but, also, by their volumes Ω

$$w(\mathbf{r} - \mathbf{r}_a, h) = \frac{W(\mathbf{r} - \mathbf{r}_a, h)}{\sum_b W(\mathbf{r}_a - \mathbf{r}_b)\Omega_b} = \frac{W(\mathbf{r} - \mathbf{r}_a, h)}{\Gamma(\mathbf{r}_a)}. \quad (4.19)$$

Such a correction ensures that w is always normalised, independently on the number of particles under the kernel hat

$$\int_{\Omega} w(\mathbf{r} - \mathbf{r}_a, h) d\mathbf{r} = \frac{\int_{\Omega} W(\mathbf{r} - \mathbf{r}_a, h) d\mathbf{r}}{\Gamma(\mathbf{r}_a)} = \frac{\sum_c W(\mathbf{r}_c - \mathbf{r}_a)\Omega_c}{\sum_b W(\mathbf{r}_a - \mathbf{r}_b)\Omega_b} = 1. \quad (4.20)$$

Since w has all the same properties as $W(\mathbf{r}, h)$, cf. Sect. 2.1, the SPH approximations for the field quantities and their spatial derivatives have forms

$$A(\mathbf{r}_a) = \int_{\Omega} A(\mathbf{r})w(\mathbf{r} - \mathbf{r}_a, h) d\mathbf{r} \quad (4.21)$$

$$\nabla A(\mathbf{r}_a) = - \int_{\Omega} A(\mathbf{r})\nabla w(\mathbf{r} - \mathbf{r}_a, h) d\mathbf{r}. \quad (4.22)$$

To evaluate density field, Grenier et al. decided to use the density definition performing approximations independently for each phase

$$\varrho_a = \sum_{b \in \chi(a)} m_b w_{ab}^{\chi}(h), \quad (4.23)$$

where

$$w_{ab}^{\chi}(h) = \frac{W_{ab}(h)}{\sum_{c \in \chi(a)} W_{ac}(h)\Omega_c}, \quad (4.24)$$

and, the indicator $\chi(a)$ identifies belonging of particle a to a given phase. However, due to the re-normalisation of the kernel, spatial distribution of particles has no influence on the density field. Therefore, the density field is not evaluated by the particle distribution, but, the evolution of particle volume Ω

$$\frac{1}{\mathfrak{S}_a} \frac{d\mathfrak{S}_a}{dt} = \langle \nabla \cdot \mathbf{u} \rangle_a, \quad (4.25)$$

where $\mathfrak{S}_a = \Omega_a / \Omega_a^0$, while Ω_a^0 denotes the initial volume of particle a .

To construct the SPH approximation of the N-S pressure term, Grenier et al. use the principle of virtual works (PVW) to derive it from the SPH divergence operator

$$\langle \nabla \cdot \mathbf{u} \rangle_a = \frac{1}{\Gamma_a} \sum_b \mathbf{u}_{ba} \nabla_a W_{ab}(h) \Omega_b. \quad (4.26)$$

Finally, the N-S pressure term has the form

$$\left\langle \frac{\nabla p}{\varrho} \right\rangle_a = \frac{1}{\varrho_a} \sum_b \left(\frac{p_a}{\Gamma_a} + \frac{p_b}{\Gamma_b} \right) \nabla_a W_{ab}(h) \Omega_b. \quad (4.27)$$

The viscous N-S term, similarly to Eq. (4.18) is approximated with the use of the inter-particle-averaged shear stress

$$\left\langle \frac{1}{\varrho} (\nabla \cdot \mu \nabla) \mathbf{u} \right\rangle_a = \frac{1}{m_a} \sum_b \frac{2\mu_a \mu_b}{\mu_a + \mu_b} \left(\frac{1}{\Gamma_a} + \frac{1}{\Gamma_b} \right) \frac{\mathbf{r}_{ab} \cdot \nabla_a W_{ab}(h)}{r_{ab}^2 + \eta^2} \mathbf{u}_{ab} \Omega_b. \quad (4.28)$$

Summarising, for each time step, the density, calculated from Eq. (4.23) determines pressure obtained from the equation of state (2.36). Then, volume, velocity and positions are calculated from Eqs. (4.25), (4.27), (4.28) and (2.35). Unfortunately, similarly to Colagrossi and Landrini (2003), due to numerical errors, the volume (density) and velocity fields can become inconsistent, cf. Sect. 2.2. Therefore, using this approach there is a necessity to use higher order time-integration schemes. Unfortunately, despite many validation tests presented by the authors, we could not obtain any solutions in reasonable time. The method requires very small time steps or (it seems to us) higher than the second order time-stepping algorithms.

4.2 Micro-mixing phenomenon

Figure 4.6 presents the Rayleigh-Taylor instability (the case discussed previously) at $t = 5$ obtained using the multiphase Hu and Adams (2006) formulation. The zoomed segment of the domain shows that close to the interface, in the distance comparable to the range of kernel smoothing (black circles), particles of both phases have a tendency to mix, affecting the interface sharpness. The main reason of this phenomenon is a lack of mechanism assuring immiscibility of phases in SPH. In the Eulerian approaches location of interface is given explicitly, therefore, this problem does not occur in these methods. A similar behaviour was also reported by Colagrossi and Landrini (2003) and by Grenier et al. (2009), but these authors suggested that the problem appears only when surface tension is negligible. However, it will be shown that this statements are incorrect.

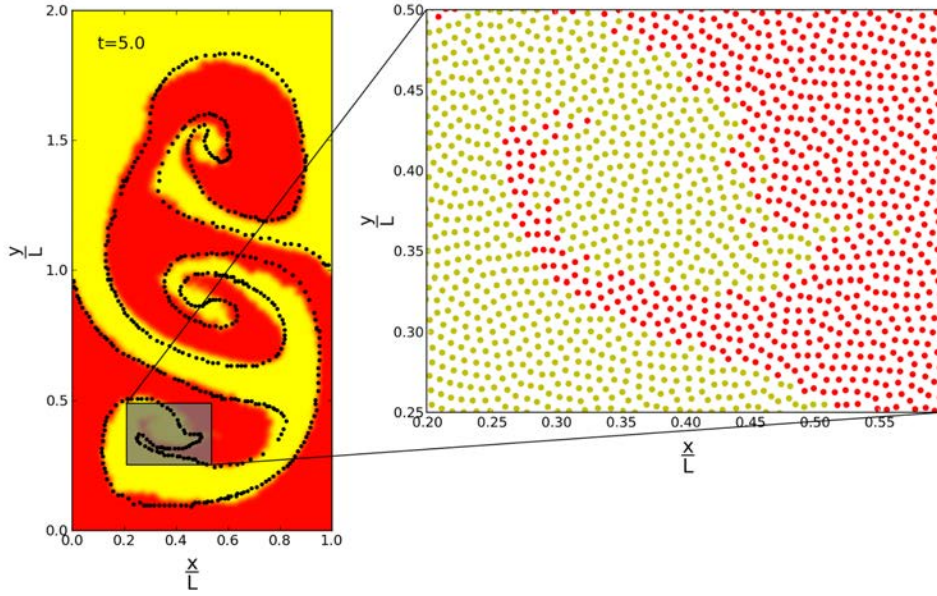


Figure 4.6: The Rayleigh-Taylor instability at $Re = 420$; density ratio between phases $\rho_U/\rho_L = 1.8$; the interface position obtained with the Hu and Adams (2006) formalism; a zoomed segment of domain shows a spurious fragmentation of the interface (particle mixing); black circles represent the range of kernel smoothing.

To prevent this and to control the interface sharpness, Colagrossi and Landrini (2003) decided to modify the equation of state as

$$p = p_0 \left[\left(\frac{\rho}{\rho_0} \right)^\gamma - 1 \right] - \varepsilon \rho^2, \quad (4.29)$$

where the last term has the form similar to the van der Waals part which is responsible for attraction (cohesion force) and ε is an empirical parameter. Using the modified equation of state separately for each phase, the global effect is a small repulsion on the interface. Instead of using explicitly Eq. (4.29), the additional term can be introduced to the N-S equation

$$\Xi_a = -\varepsilon \sum_{b \in \chi(a)} (\rho_a^2 + \rho_b^2) \nabla_a W_{ab}(h) \Omega_b. \quad (4.30)$$

However, the authors were not able to obtain accurate solutions without the use of additional, introduced by Monaghan (1989), correction to the velocity field, commonly known as XSPH.

Another remedy for sub-kernel mixing phenomena was proposed by Grenier et al. (2009). Similarly to Colagrossi and Landrini, in the way to prevent inter-phase penetration, a small repulsive force on the interface was applied by introducing an additional term to the Navier-Stokes equation

$$\Xi_a = \varepsilon \sum_{b \notin \chi(a)} \left(\left| \frac{p_a}{\Gamma_a} \right| + \left| \frac{p_b}{\Gamma_b} \right| \right) \nabla_a W_{ab}(h) \Omega_b. \quad (4.31)$$

The above relation is expressed in the Grenier et al. (2009) multiphase formulation with the use of normalised kernel, cf. Sect. 4.1.4. However, the main difference between approaches (4.30) and (4.31) is a direct use of pressure field to determine a magnitude of correction. For cases where pressure in the domain can significantly change or, even, for cases where the pressure is treated as a sum of dynamical pressure (from the equation of state) and the hydrostatic pressure, the approach (4.31) cannot be used. Recently, Monaghan and Rafiee (cited without detail by Monaghan (2012)) suggested another solution, where an additional force on the interface is introduced through the term

$$\Xi_a = 0.08 \left(\frac{\rho_d - \rho_l}{\rho_d + \rho_l} \right) \sum_b m_b \left| \frac{p_a + p_b}{\rho_a \rho_b} \right| \nabla_a W_{ab}(h), \quad (4.32)$$

where ρ_d is a density of denser phase and ρ_l is a density of the lighter one. The value 0.08 is given from the empirical studies. However, it is not clear how these parameters are obtained and what is the range of usability. Yet another idea was proposed by Das and Das (2009), where special inter-particle force is applied by adding molecular-like interaction

$$\Xi_a = \frac{\varepsilon}{m_a} \sum_b \begin{cases} (P_d^6 - P_d^4) \mathbf{r}_{ab}/r_{ab}^2, & \text{if } P_d \geq 1, \\ 0, & \text{if } P_d < 1, \end{cases} \quad (4.33)$$

where $P_d = (h_a + h_b)/2r_{ab}$ (for the variant of variable h). And again, the role of this term is to introduce a small repulsive force between phases.

In the present work, we propose, yet another approach, similar to Eq. (4.31), but, using the Hu and Adams formulation (cf. Sect. 4.1.3) and without explicit pressure dependency. Starting from Eq. (4.17), assuming $\bar{A}_{ab} = 1$ and applying summation over the other phase only, the additional term may be written as

$$\Xi_a = \frac{\varepsilon}{m_a} \sum_{b \in \chi(a)} \left(\frac{1}{\Theta_a^2} + \frac{1}{\Theta_b^2} \right) \nabla_a W_{ab}(h). \quad (4.34)$$

This term will be used in the further part of this work as the interface sharpness correction procedure.

Figure 4.7 shows the recalculated problem of the Rayleigh-Taylor instability, presented previously in Sect. 4.1.3, with the interface sharpness correction term (4.34) for $\varepsilon = 0.15$. The comparison of the particle distributions near the interface using the SPH approach with and without the sharpness correction procedure is presented in Fig. 4.8. However, in the considered R-T instability, the density difference between phases is not very high ($\rho_U/\rho_L = 1.8$, cf. Sect. 3.4), therefore, the existence of the micro-mixing phenomena has no strong impact on the accuracy. The problem became very important for all cases where the density difference between phases is high.

One of the most common cases where huge density difference may appear is a problem of an air bubble rising in water. For testing purposes, two-dimensional test case of gas bubble submerged in liquid is considered. The rectangular domain of size $L_x = 6R$ and $L_y = 10R$, where R is the bubble radius, is taken. The gaseous particles are initially distributed at

$$\left(x - \frac{L_x}{2} \right)^2 + \left(y - \frac{L_y}{2} \right)^2 < R^2. \quad (4.35)$$

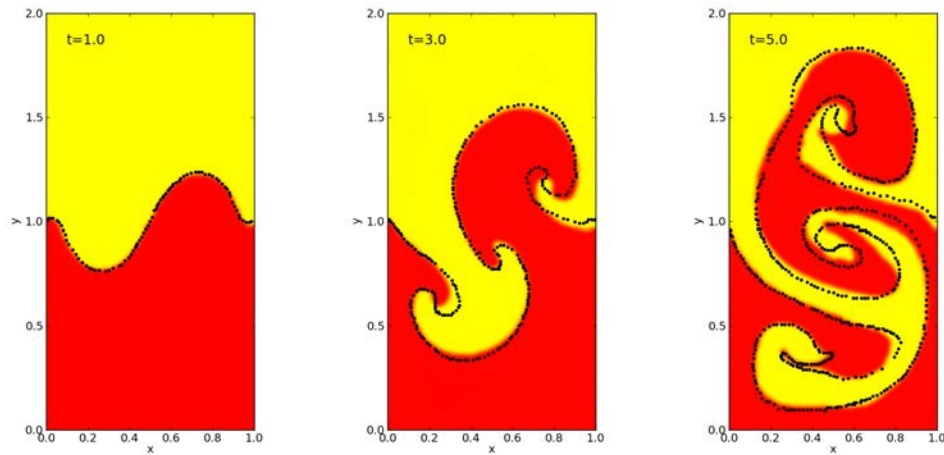


Figure 4.7: The Rayleigh-Taylor instability at $Re = 420$; the interface position obtained using the Hu and Adams (2006) formalism with Eq. (4.34) to control the interface sharpness ($\epsilon = 0.15$); the black points represent the interface with the Level-Set formulation (Grenier et al., 2009).

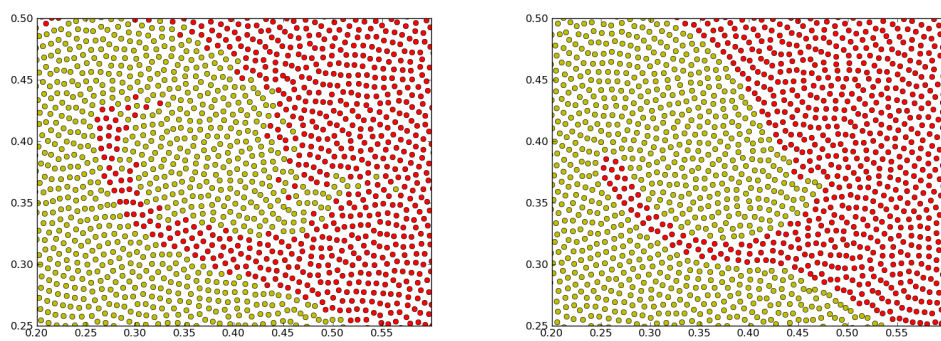


Figure 4.8: The particle distributions near the interface without (left) and with (right) the sharpness correction procedure.

The density ratio of liquid (L) and gas (G) phases is $\rho_L/\rho_G = 1000$, while the kinematic viscosity $\nu_L/\nu_G = 1/128$. In the case of negligible surface tension, the flow can be described only by the Reynolds number

$$Re = \frac{\sqrt{(2R)^3 g}}{\nu_L}, \quad (4.36)$$

where g is the absolute value of the gravity. The SPH simulations were performed using the Hu and Adams approach with particles initially regularly distributed on 120×200 lattice. The gas inside bubble was treated as compressible ($\gamma = 1.4$). Figure 4.9 presents an evolution of air bubble rising in water for $Re = 1000$, no surface tension, and different values of sharpness control parameter $\varepsilon = 0, 0.35, 1.5$. The SPH results are compared to the data obtained using the Level-Set method by Sussman et al. (1994) (the black diamonds). In the case with no sharpness correction procedure ($\varepsilon = 0$), cf. Fig. 4.9(left), due to the sub-kernel mixing, the interface is highly distorted. Since the density difference between phases is high and there is no mechanism assuring immiscibility of phases in SPH, lighter particles, representing gaseous phase, can easily penetrate liquid phase, causing degradation of accuracy. This example shows the necessity to use the interface sharpness correction in multiphase SPH. In the case of $\varepsilon = 0.35$, cf. Fig. 4.9(center), the comparison with the reference data shows that both approaches yield similar shapes of the interface. Initially circular bubble deforms to take a horseshoe shape and finally splits into parts. Choosing too high a value of parameter ε , cf. Fig. 4.9(right), again, the interface position is strongly distorted (but accuracy is much higher than in the case $\varepsilon = 0$). Therefore, it is essential to detect the range of values of ε for which the interface sharpness correction is useful.

To measure the accuracy of the SPH calculation of the interface position for different values of ε , we decided to introduce two quantities: the mean deviation of the color function ($c = 0$ for liquid phase and $c = 1$ for gaseous phase, for details, cf. Sect 5.2), calculated using the SPH approach, from the exact value ($c = 1/2$) expected on the interface

$$S_c = \sqrt{\frac{1}{M} \sum_i \left(\frac{1}{2} - \langle c \rangle(\mathbf{r}_i) \right)^2}, \quad (4.37)$$

where sum is over the M reference points (obtained by Sussman et al. (1994)) describing the position of interface (the black diamonds in Fig. 4.9), and, the mean value of gradient norms of color functions calculated using the SPH method at the points obtained from reference data denoting the position of interface

$$S_{\nabla c} = \frac{1}{M} \sum_i \|\langle \nabla c \rangle(\mathbf{r}_i)\|. \quad (4.38)$$

Figure 4.10 presents the calculations of S_c (left) and $S_{\nabla c}$ (right) for values of ε in range between 0 and 1.5. In both accuracy measurements, the highest accuracy is reached for the range between $\varepsilon = 0.2$ and 0.5. However, it is important to note, that the proper choice of parameter ε may be different for different types of flow. But, for systems which possess some similarities, the use of S_c or $S_{\nabla c}$ allows to quickly find

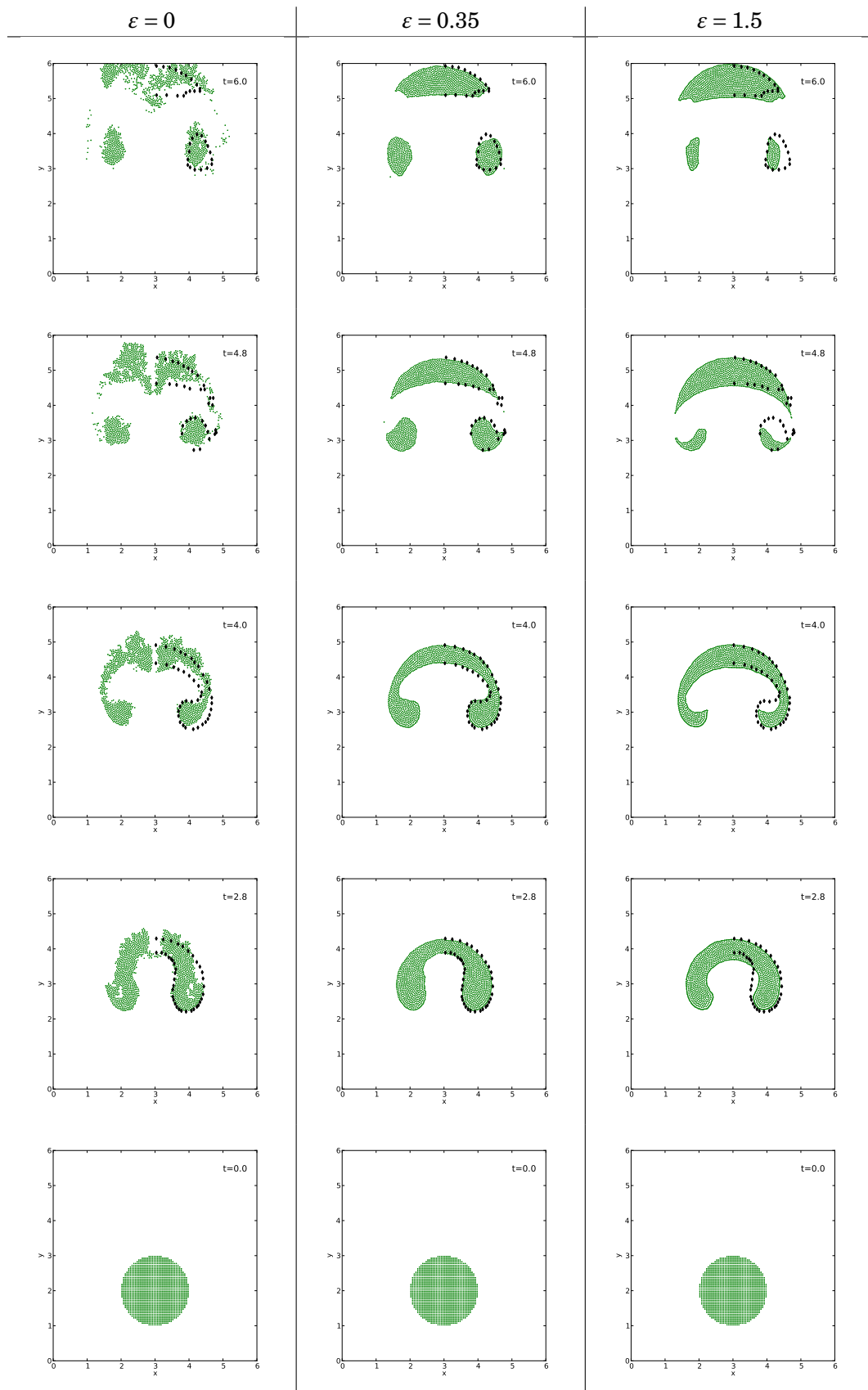


Figure 4.9: Evolution of an air bubble rising in water with high Reynolds number (still laminar) and no surface-tension ($Re = 1000$, density ratio 1000/1); the green points denote SPH solutions computed with different values of sharpness control parameter ε ; the black diamonds represent the interface obtained with the Level-Set method by Sussman et al. (1994).

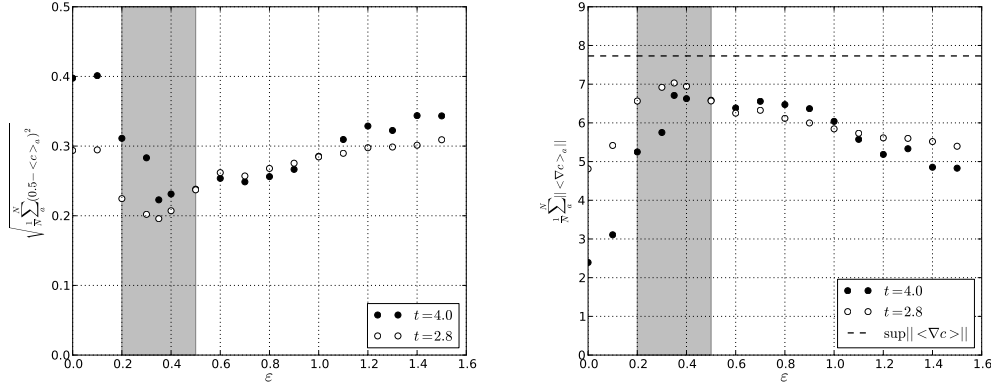


Figure 4.10: The measure of accuracy for different values of parameters ε using: (left) S_c and (right) $S_{\nabla c}$; the grey box denotes the region of the highest accuracy ($\varepsilon = 0.2 - 0.5$); the dashed line at right plot represent the highest possible value of $S_{\nabla c}$ for the given h .

an approximate value of ε corresponding to the highest accuracy of the interface position calculation.

In both (Colagrossi and Landrini, 2003) and (Grenier et al., 2009), the authors suggest that the problem of micro-mixing phenomena appears only when surface tension is negligible. However, in both papers, the authors do not present any results for flow with surface tension. The most common numerical model of surface tension force is the one based on the Continuum Surface Force (CSF) method proposed by Brackbill et al. (1992) (for details, cf. Chapter 5). One of the key points of this approach is that the surface tension is converted into the force per unit volume, and, as a consequence, the force is acting on particles in the transition zone of the size of the kernel range, cf. Fig. 4.11. So, it is obvious that the use of the CSF technique cannot provide any mechanism protecting the system from micro-mixing. Figure 4.12 presents the SPH simulation of an air bubble rising in water with the presence of high surface tension (the CSF technique). In the case without the interface sharpness correction, Fig. 4.12(left), the interface position is highly distorted. For $\varepsilon = 0.5$, Fig. 4.12(right), the interface shape is very stable. Summarizing, in the author opinion, the only way to avoid micro-mixing phenomena in SPH (at the hydrodynamic level), without introducing any empirical parameters, is the use of a hybrid SPH-Level Set or SPH-Front Tracking methods. However, such approaches are still not well developed.

4.3 Conclusions

Due to the fact that SPH is a fully Lagrangian technique and there is no necessity to handle the interface position as it is obligatory in Eulerian methods, during the last ten years, the SPH approach has been greatly developed to deal with free-surface and multi-phase flows. Comparing different formulations of governing equations presented in this work, it is easy to notice how some small details may

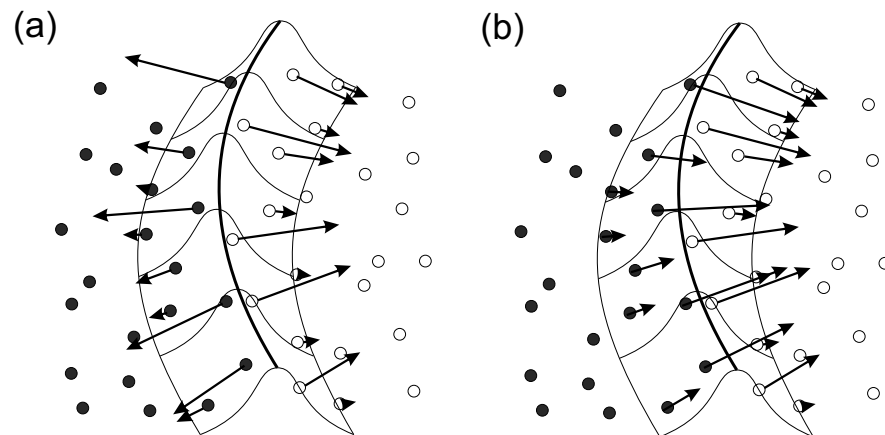


Figure 4.11: Sketch of the transition zone at the interface; (a) the repulsion provided by the interface sharpness correction procedure, (b) the surface tension force provided by the CSF technique.

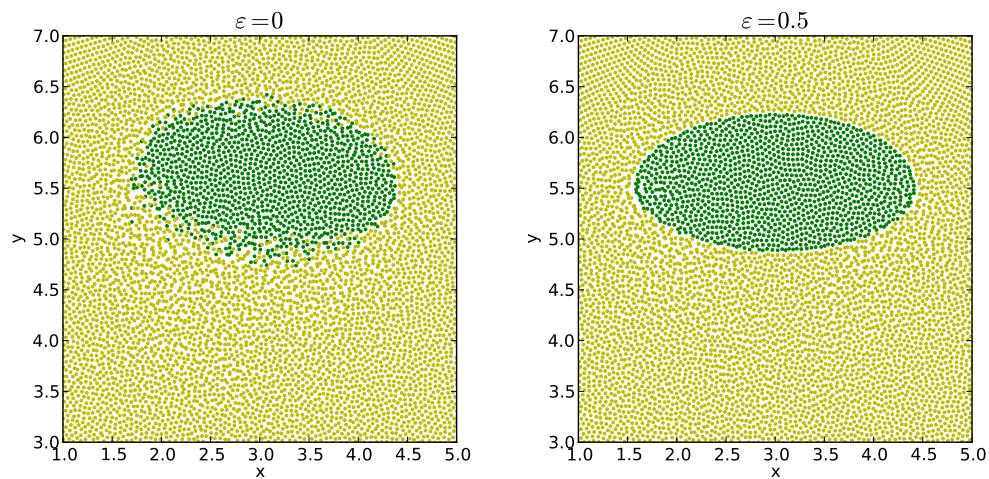


Figure 4.12: An air bubble rising in water at $E\ddot{o} = 1$ and $Mo = 10^{-12}$ (for details, cf. Chapter 6); the green points denote SPH solutions simulated without (left) and with (right) the sharpness control procedure ($\varepsilon = 0.5$); the presence of high surface tension does not prevent from the sub-kernel phase mixing; pictures taken at $t = 4$, before a beginning of wobbling.

have strong impact on the results. So far, it seems that, for simulations of multiphase flow, the Hu and Adams approach is the most useful among the presented formalisms. But, this is not yet an ideal solution. Its main limitation is the lack of ability to perform calculations of free-surface flows. Potentially, the method of wider applicability (able to simulate free-surface flows and, also, variation of particle volumes) seems to be the approach proposed by Grenier et al.; however, this approach, in our tests, requires to use unacceptably small time steps. However, the main advantage of the SPH approach, which is no necessity to handle the position of the interface, unfortunately, implies the new problem – the spurious fragmentation of the interface. The main reason of this phenomenon is a lack of mechanism assuring immiscibility of phases in SPH. In this chapter, all the remedies which are available in the literature were discussed, and, a new variant of sharpness correction procedure was proposed and validated. However, despite the significant improvement in accuracy observed using the sharpness correction procedures, it is clear that further studies to resolve this problem are necessary.

Chapter 5

Surface-tension force in SPH

5.1 Introduction

In the SPH approach, there are many ways to implement the surface-tension effects. One of the most interesting approaches is the proposition of Nugent and Posch (2000), later improved in Tartakovsky and Meakin (2005), and Tartakovsky et al. (2009), where a modified van der Waals equation of state is used to provide the surface tension force by ‘micro-scale’ interaction among particles. However, because of dependency on micro-scale parameters, this solution is hard to use in engineering applications. Among the macroscopic approaches, two of them, based on the Continuum Surface Force model are the most frequently used. The first, basic, concept consists in the SPH computation of a local curvature of an interface. In the second approach, the surface tension force is computed using a surface stress tensor (CSF-SST). These approaches are described in Sections 5.3 and 5.4. The discussion of the SPH surface-tension models is preceded by Section 5.2 describing the methods of computing normal vectors to the interface. The validation of the surface tension models is performed with two standard numerical tests: the square-droplet deformation and the water droplet in air oscillation.

5.2 Computation of the vector normal to interface

To distinguish between phases, each particle carries a constant integer identifier. Since particles move during simulation, there is no necessity to handle the interface shape as it is done in the Volume of Fluid or Level-Set methods. In the presented work we use the colour function that changes by unity across the interface (two-phase flows)

$$c_a = \begin{cases} 1, & \text{if particle } a \text{ belongs to phase 1,} \\ 0, & \text{if particle } a \text{ belongs to phase 2.} \end{cases} \quad (5.1)$$

Now, with such a defined function, the normal vector to the interface can be obtained using

$$\mathbf{n} = \frac{\nabla c}{[c]}, \quad (5.2)$$

where $[c]$ is the jump in c across the interface (here $[c]$ is always 1).

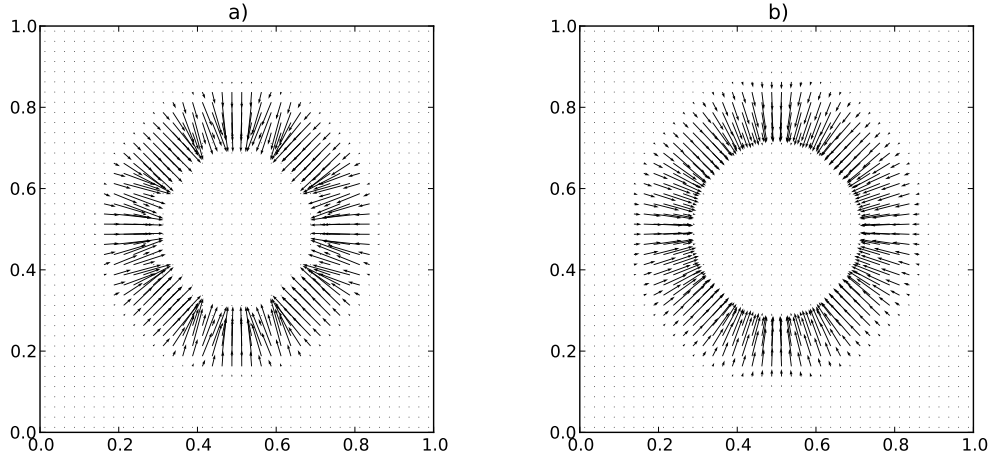


Figure 5.1: Field of vectors normal to the interface obtained using: a) expression (5.3), b) smoothed colour field, Eqs. (5.4) and (5.6)

The simplest SPH expression of ∇c is given by the use of Eq. (2.16)

$$\mathbf{n}_a = \sum_b \frac{m_b}{\rho_b} c_b \nabla_a W_{ab}(h). \quad (5.3)$$

However, more accurate solutions for the normal vectors can be obtained when the colour field is firstly smoothed by the convolution with a high order kernel (Morris, 2000)

$$\tilde{c}_a = \sum_b \frac{m_b}{\rho_b} c_b W_{ab}. \quad (5.4)$$

What is more, Eq. (5.2), by the use of the identity

$$\nabla c \equiv \nabla c - c \nabla 1, \quad (5.5)$$

can be expressed into the symmetrical SPH form

$$\mathbf{n}_a = \sum_b \frac{m_b}{\rho_b} (\tilde{c}_b - \tilde{c}_a) \nabla_a W_{ab}(h), \quad (5.6)$$

which ensures that for constant colour field the normal vectors vanish explicitly. For a test case of circular interface, Fig. 5.1 presents the fields of normal vectors obtained using both approaches. The comparison of them shows that the method involving the colour function smoothing procedure gives much more realistic results.

Alternatively, Eq. (5.2) can be expressed in the SPH formalism, using any of formulae for gradients presented in the Chapter 4. In the Hu and Adams (2006) formalism, Eq. (5.2) has the form

$$\mathbf{n}_a = \Theta_a \sum_b \left(\frac{c_a}{\Theta_a^2} + \frac{c_b}{\Theta_b^2} \right) \nabla_a W_{ab}(h). \quad (5.7)$$

5.3 Continuum Surface Force model (CSF)

The first surface-tension model in SPH was introduced by Morris (2000). It is based on the Continuum Surface Force (CSF) technique proposed by Brackbill et al. (1992). The key point of this approach is to compute the local curvature of an interface. The surface tension is converted into the force per unit volume

$$\mathbf{F}_s = \mathbf{f}_s \delta_s, \quad (5.8)$$

where δ_s is a suitably-chosen surface delta function, and,

$$\mathbf{f}_s = \sigma \kappa \hat{\mathbf{n}} + \nabla_s \sigma, \quad (5.9)$$

where \mathbf{f}_s is the force per unit area, σ is the surface tension coefficient, κ is the local curvature of the interface, and $\hat{\mathbf{n}}$ is the unit vector normal to the interface. The second r.h.s. term in Eq. (5.9), linked with the Marangoni effect, is neglected in the present work. The normal unit vectors $\hat{\mathbf{n}}$ can be calculated using the colour function (Sect. 5.2)

$$\hat{\mathbf{n}} = \frac{\mathbf{n}}{|\mathbf{n}|} = \frac{\nabla c}{|\nabla c|}. \quad (5.10)$$

The curvature of the interface can be obtained with the relation

$$\kappa = -\nabla \cdot \hat{\mathbf{n}}. \quad (5.11)$$

In the SPH formalism, the simplest expression for the divergence of $\hat{\mathbf{n}}$ is constructed with Eq. (2.16)

$$\langle \nabla \cdot \hat{\mathbf{n}} \rangle_a = \sum_b \frac{m_b}{\rho_b} \hat{\mathbf{n}}_b \cdot \nabla_a W_{ab}(h). \quad (5.12)$$

Here, as in the case of (5.6), much more accurate solutions are obtained using the symmetrical form

$$\langle \nabla \cdot \hat{\mathbf{n}} \rangle_a = \sum_b \frac{m_b}{\rho_b} (\hat{\mathbf{n}}_b - \hat{\mathbf{n}}_a) \cdot \nabla_a W_{ab}(h). \quad (5.13)$$

Alternatively, $\hat{\mathbf{n}}$ can be calculated using the Hu and Adams formalism

$$\langle \nabla \cdot \hat{\mathbf{n}} \rangle_a = \Theta_a \sum_b \left(\frac{\hat{\mathbf{n}}_a}{\Theta_a^2} + \frac{\hat{\mathbf{n}}_b}{\Theta_b^2} \right) \cdot \nabla_a W_{ab}(h). \quad (5.14)$$

Unfortunately, independently of the use of either Eqs. (5.12), (5.13) or (5.14), large errors of curvature may occur. The reason is that the computations of curvature require normalised vectors $\hat{\mathbf{n}}$. In the regions located far from the interface, but still in the smoothed transition zone where \mathbf{n} is small but yet non-zero, the normalisation procedure (5.10) leads to increase the computational errors (the normalised vectors may have an erroneous direction). To solve this problem, Morris (2000) has proposed an approach that uses special criteria to determine the normal vectors that can lead to errors. To normalise the normal vectors \mathbf{n} , following criteria are used

$$\hat{\mathbf{n}}_a = \begin{cases} \mathbf{n}_a / |\mathbf{n}_a|, & \text{if } N_a = 1, \\ 0, & \text{otherwise} \end{cases} \quad (5.15)$$

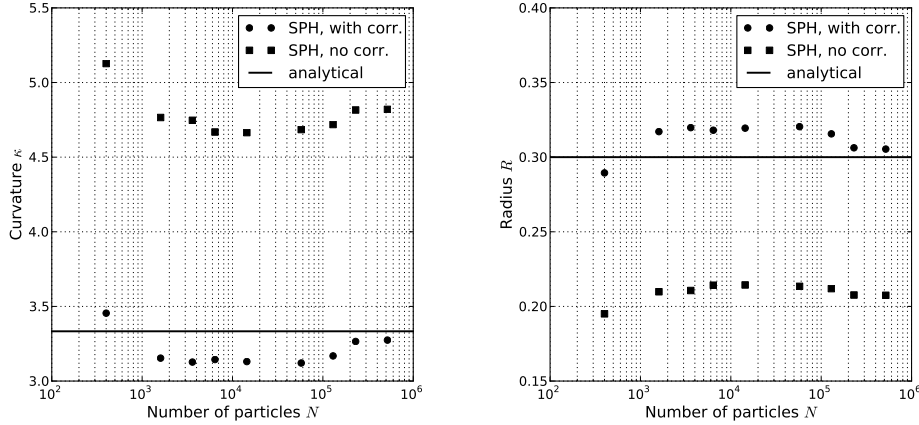


Figure 5.2: The convergence of the SPH solutions of curvature and radius for the circular phase of radius $R = 0.3$ (cf. Fig. 5.1); results obtained for different number N of particles in the domain; the SPH solutions obtained with and without the correction proposed by Morris (2000).

and

$$N_a = \begin{cases} 1, & \text{if } \mathbf{n}_a > \epsilon, \\ 0, & \text{otherwise} \end{cases} \quad (5.16)$$

where the parameter ϵ is here chosen to be $0.01/h$ (after Morris), but different criteria can also be applied.

However, due to the reduction of normals in the SPH sum, to assure the consistency, the renormalisation is necessary. Therefore, using the relation (5.13) the SPH curvature estimation has the form

$$\kappa_a = - \frac{\sum_b \frac{m_b}{\rho_b} \min(N_a, N_b) (\hat{\mathbf{n}}_b - \hat{\mathbf{n}}_a) \cdot \nabla_a W_{ab}(h)}{\sum_b \frac{m_b}{\rho_b} \min(N_a, N_b) W_{ab}(h)}. \quad (5.17)$$

The surface delta function can be calculated in many ways. Here, it is employed as

$$\delta_s = |\mathbf{n}|. \quad (5.18)$$

Finally, the surface tension force can be included into the system by adding a new term

$$\frac{d\mathbf{u}_a^{\text{surf}}}{dt} = \frac{\sigma_a \kappa_a}{\rho_a} \hat{\mathbf{n}}_a, \quad (5.19)$$

to the N-S equation.

Figure 5.2 presents the convergence of the SPH solutions of curvature and radius for the circular interface of radius $R = 0.3$. The comparison of the results shows that the solution computed with the correction proposed by Morris is much more realistic.

The main disadvantages of the CSF approach are the lack of exact conservation of linear and angular momentum and problems with computing curvature of small contact angles between phases. However, this method is expected to be the most stable as the resolution is increased.

5.4 CSF - Surface Stress Tensor model (CSF-SST)

The second model, introduced by Lafaurie et al. (1994), will be called here the Continuum Surface Force - Surface Stress Tensor (CSF-SST) method. In this approach, the surface-tension force per unit volume is expressed as the divergence of the capillary pressure tensor Π_s :

$$\mathbf{F}_s = -\nabla \cdot \Pi_s, \quad (5.20)$$

$$\Pi_s = -\sigma(\mathbf{I} - \hat{\mathbf{n}}\hat{\mathbf{n}})\delta_s, \quad (5.21)$$

where \mathbf{I} denotes the unit spherical tensor (the Kronecker delta δ_{ij}). As in the case of CSF model, to improve the accuracy, only normal vectors satisfying (5.15) can be chosen to have an influence on the result. A suitable, symmetrical SPH approximation for this technique may be written, similarly to the Colagrossi and Landrini N-S pressure term (Sect. 4.1.2), as

$$\frac{d\mathbf{u}_a^{\text{surf}}}{dt} = -\sum_b m_b \frac{\Pi_{sa} + \Pi_{sb}}{\rho_a \rho_b} \nabla_a W_{ab}(h). \quad (5.22)$$

Using the formulation of Hu and Adams (Sect. 4.1.3), we obtain the form

$$\frac{d\mathbf{u}_a^{\text{surf}}}{dt} = -\frac{1}{m_a} \sum_b \left(\frac{\Pi_{sa}}{\Theta_a^2} + \frac{\Pi_{sb}}{\Theta_b^2} \right) \nabla_a W_{ab}(h). \quad (5.23)$$

This method is fully conservative. However, it is widely known that SPH momentum conserving formulations are potentially unstable when attractive forces affect the particles (Sweagle et al., 1995). Unfortunately, since a trace of the tensor \mathbf{I} is equal to the number of dimensions D , while

$$\text{Tr}(\hat{\mathbf{n}}\hat{\mathbf{n}}) = 1, \quad (5.24)$$

the negative pressure contribution (tension) is

$$p^- = \frac{D-1}{D} \sigma \delta_s. \quad (5.25)$$

The only influence of p^- is the net force and it has no contribution to surface tension, so, in the places where the pressure p dominates p^- a stable solution is expected. However, increasing the resolution (decreasing the smoothing length h), the maximal value of δ_s increases. The local contribution of p^- growth resulting in unstable solution.

Therefore, to avoid the stability problems, Morris (2000) proposed to use a modified version of stress tensor (5.21)

$$\Pi_s^* = \Pi_s - \sigma \max(\delta_s) \mathbf{I}. \quad (5.26)$$

In the present work, we decided to use its more precise variant (smaller contribution to the repulsive net force)

$$\Pi_s^* = \Pi_s - \sigma \frac{D-1}{D} \max(\delta_s) \mathbf{I}. \quad (5.27)$$

Another solution was proposed by Hu and Adams (2006). The authors decided to use a modified version of stress tensor (5.21) in the form

$$\Pi_s = -\sigma \left(\frac{1}{D} \mathbf{I} - \hat{\mathbf{n}}\hat{\mathbf{n}} \right) \delta_s. \quad (5.28)$$

Since $\text{Tr}(\mathbf{I}/D - \hat{\mathbf{n}}\hat{\mathbf{n}}) = 0$, the pressure p^- is eliminated.

However, despite using the methods correcting the stability in the present work, it was not possible to completely eliminate the instability issues, see next section.

5.5 Numerical validation tests

5.5.1 Square-droplet deformation

To validate and compare the surface tension models, the square-droplet deformation test was decided to be calculated. Similarly to the three-dimensional cube-to-sphere droplet deformation test presented in Sect. 3.7, the considered here two-dimensional case involves cubical box of fluid with the edges of length L containing the inner phase of centred cubical volume of another fluid of the edges $a = 0.6L$. The density of both phases is ρ and the viscosity coefficient ν . The influence of surface tension is described by the Weber number, $We = \rho a u^2 / \sigma$, whereas the capillary number, $Ca = \rho \nu u / \sigma$, accounts also for viscosity. Here, we chose $Ca^2 / We = \nu^2 \rho / a \sigma = 2/30$. The capillary number, based on the maximum velocity in the domain, was 0.07. Since the surface tension is present, an initially square patch deforms in time to take the circular shape. From the Laplace law the pressure within formed droplet must be higher than in the surrounding fluid and should change across the interface satisfying the condition

$$\nabla p = \frac{\sigma}{R} = \frac{\sigma \sqrt{\pi}}{a}, \quad (5.29)$$

where R is the droplet radius.

The evolution of particle distributions obtained using the CSF and CSF-SST models is presented in Fig. 5.3. Both simulations were performed using the spatial resolution $N = 60 \times 60$ particles initially homogeneously distributed in the domain and $h/\Delta r = 2$. All results are suitably normalized by the droplet radius R in space and the surface tension time scale $t_\sigma = \sqrt{\rho a^3 / \sigma}$ in time. The evolution of velocity field is presented in Fig. 5.4.

Since the CSF approach is non-conservative, particles near the interface chaotically move (parasitic currents) even when the steady-state solution is reached. Despite these artifacts, the steady-state solution is stable and its influence on the solution decreases when the resolution increases. The situation is much worse in the case of the CSF-SST approach. Due to the instabilities, described in Sect. 5.4, which appear with conservative approaches only, after obtaining the steady-state solution, the particle clustering phenomenon starts to affect both the velocity and density fields. The phenomenon intensifies until the simulation breaks down. What is more, increasing resolution the system becomes more sensitive to this disorder.

The steady-state pressure profiles obtained using both the CSF and CSF-SST approaches are presented in Fig. 5.5, where they are compared to the analytical

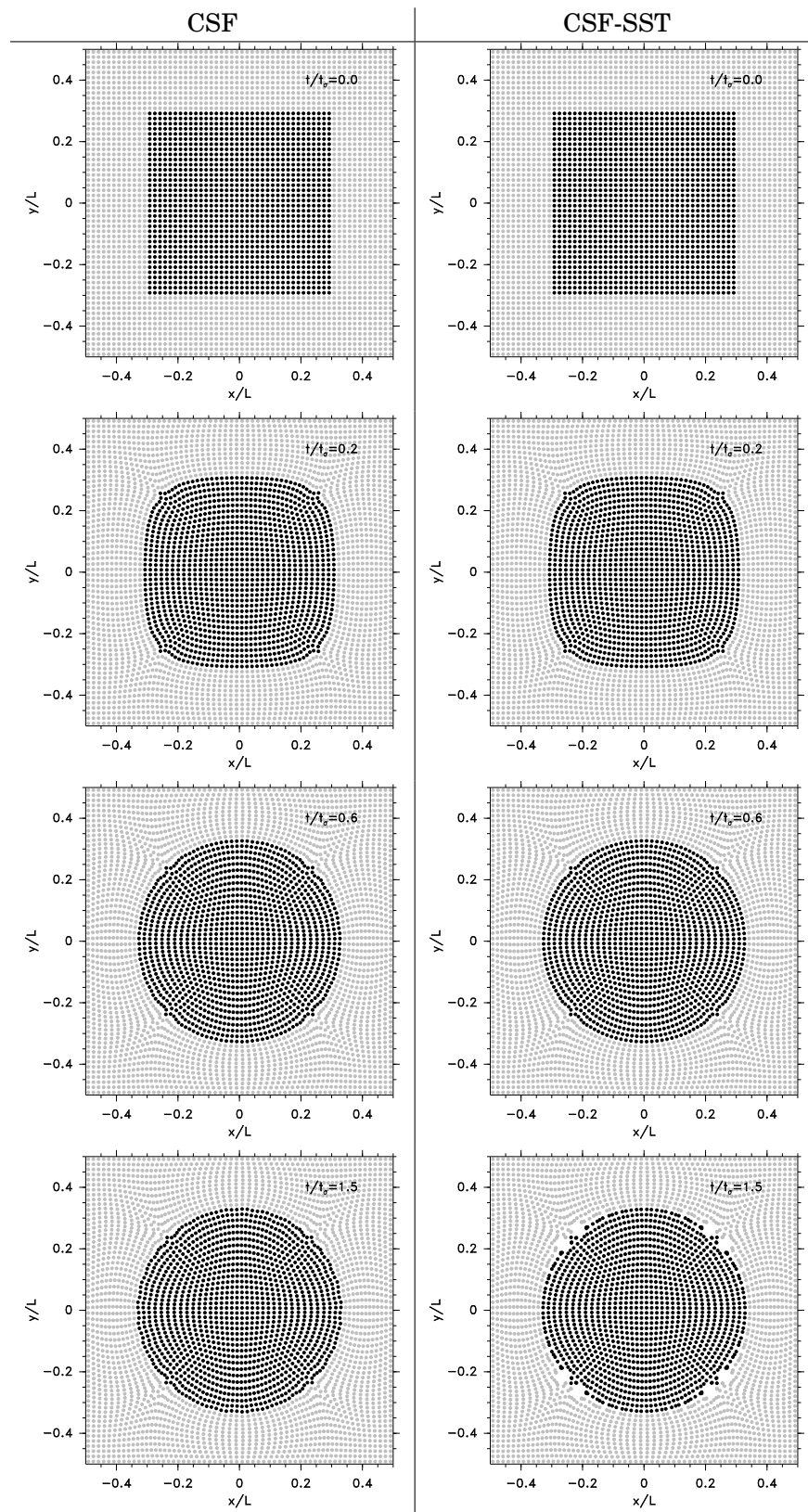


Figure 5.3: The evolution of particle distribution in the square-droplet deformation test ($N = 60 \times 60$) obtained with: (left) CSF and (right) CSF-SST methods.

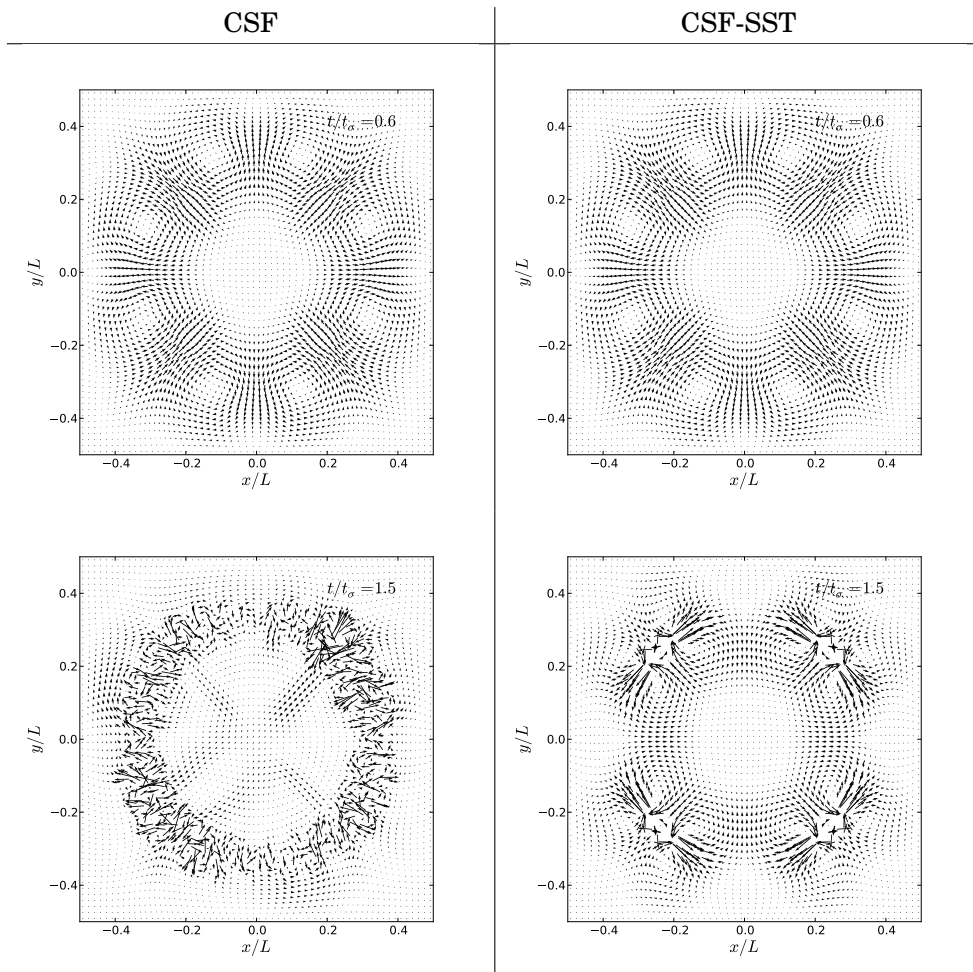


Figure 5.4: The evolution of velocity field in the square-droplet deformation test ($N = 60 \times 60$) obtained with: (left) CSF and (right) CSF-SST methods.

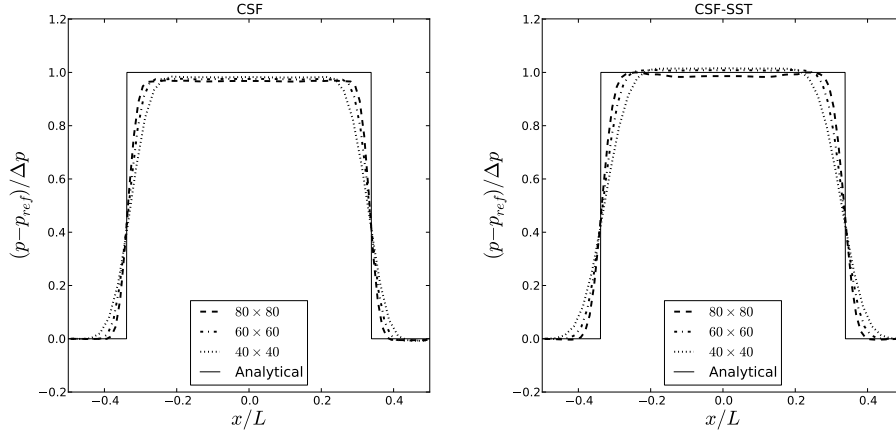


Figure 5.5: Pressure profiles in the steady-state solution of the square-droplet deformation obtained using: (left) CSF and (right) CSF-SST surface tension model; evaluation of the influence of number of particles N ($h/\Delta r = 2$) on the pressure prediction; results are compared to the analytical solution (5.29).

solution (5.29). To evaluate the influence of the number of particles N on the prediction of the pressure field, the case was calculated with $N = 40 \times 40$, 60×60 and 80×80 particles in the domain. The presented results were obtained for $t/t_\sigma = 0.6$, it is before the CSF-SST instabilities appear (here $t/t_\sigma < 0.7$). In both methods, since the surface tension force is converted into the force per unit volume, the pressure profile is smoothed in length comparable with the kernel smoothing range.

5.5.2 Capillary wave

One of the most common two-dimensional dynamic multiphase test cases is a circular droplet oscillating under the action of surface tension force. Here, we decided to simulate oscillation of droplet corresponding to an air-liquid system: the density and dynamic viscosity ratio between droplet and surrounding gas were respectively $\rho_D/\rho_G = 1000$ and $\mu_D/\mu_G = 100$. The simulations were performed in the square box of size L . The droplet of radius $R = 0.1875L$ was placed at the centre of the domain. The initial perturbation was given by the divergence-free velocity field in the form

$$\begin{aligned} u_x &= u_0 \frac{x}{r_0} \left(1 - \frac{y^2}{r_0 r} \right) \exp\left(-\frac{r}{r_0}\right), \\ u_y &= u_0 \frac{y}{r_0} \left(1 - \frac{x^2}{r_0 r} \right) \exp\left(-\frac{r}{r_0}\right), \end{aligned} \quad (5.30)$$

where $u_0 = 4\sqrt{R^3 \rho_D / \sigma}$, $r_0 = 0.25R$, while r is the distance to the droplet center. Lamb (1932) showed that the frequency of oscillations of a two-dimensional droplet is given by

$$\omega_n = \sqrt{\frac{(n^3 - n)\sigma}{\rho_D R^3}}, \quad (5.31)$$

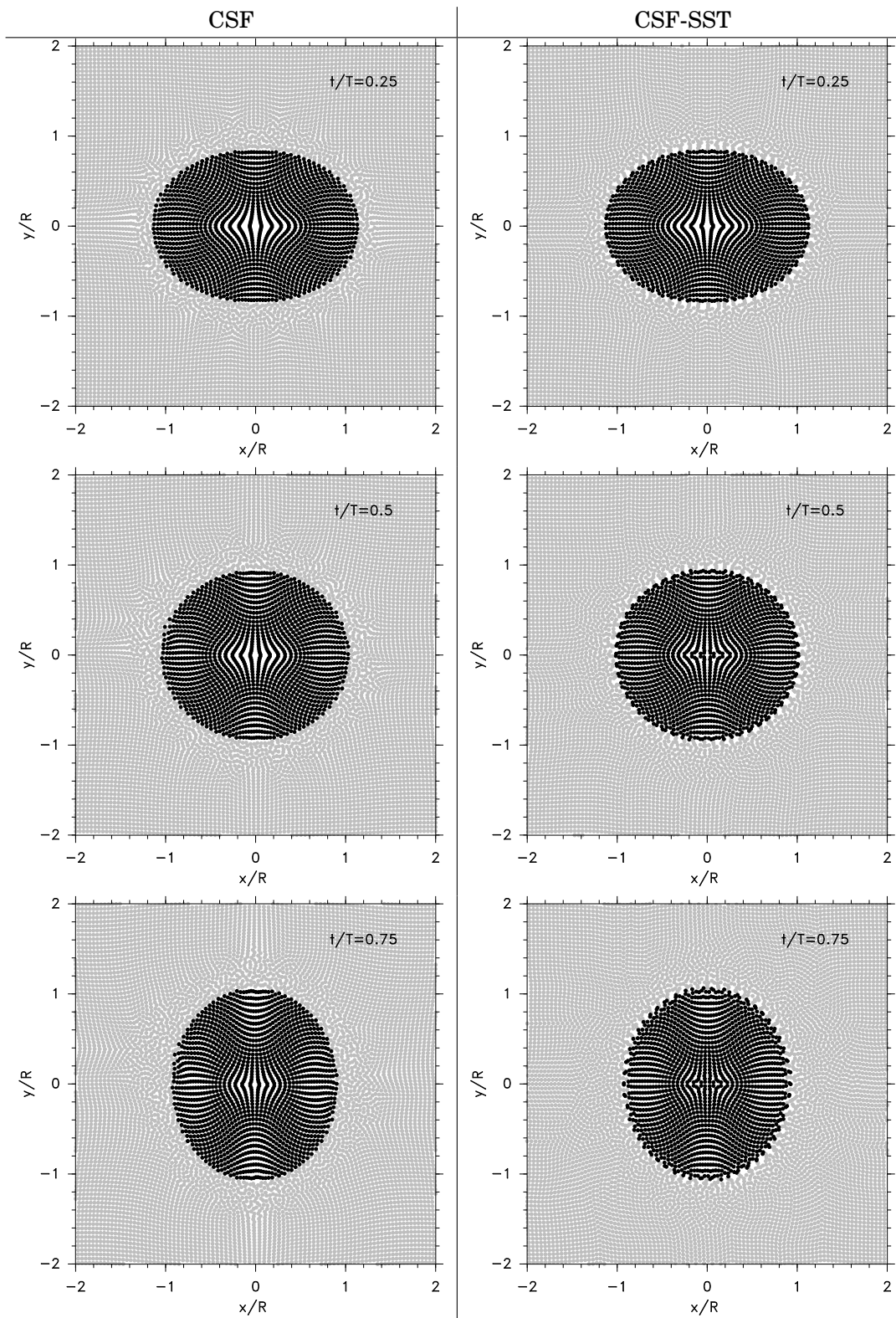


Figure 5.6: The evolution of particle positions in the droplet oscillation test ($N = 120 \times 120$) obtained with: (left) CSF and (right) CSF-SST methods.

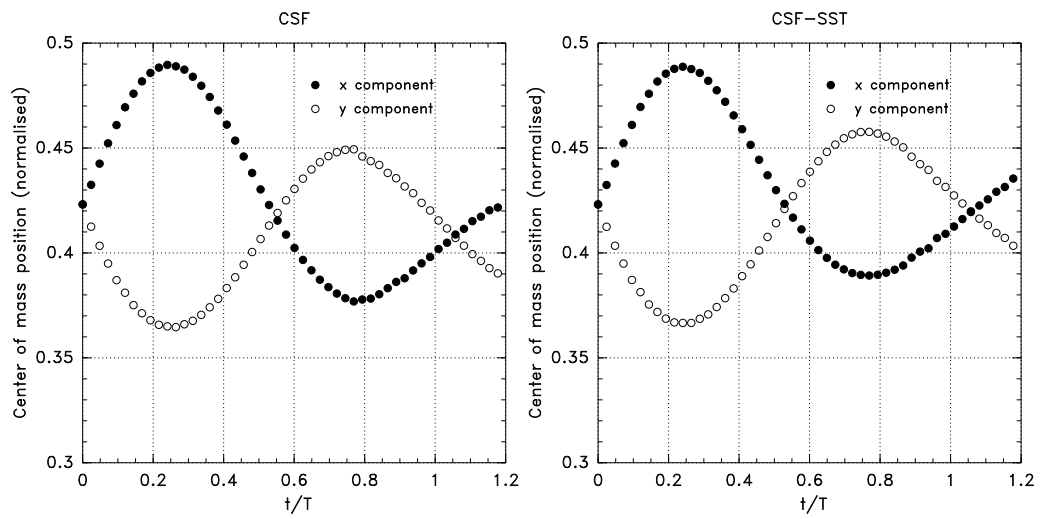


Figure 5.7: Oscillation of the centre of mass position (normalised with R) of the droplet's upper right quarter; the results obtained using: (left) CSF and (right) CSF-SST methods.

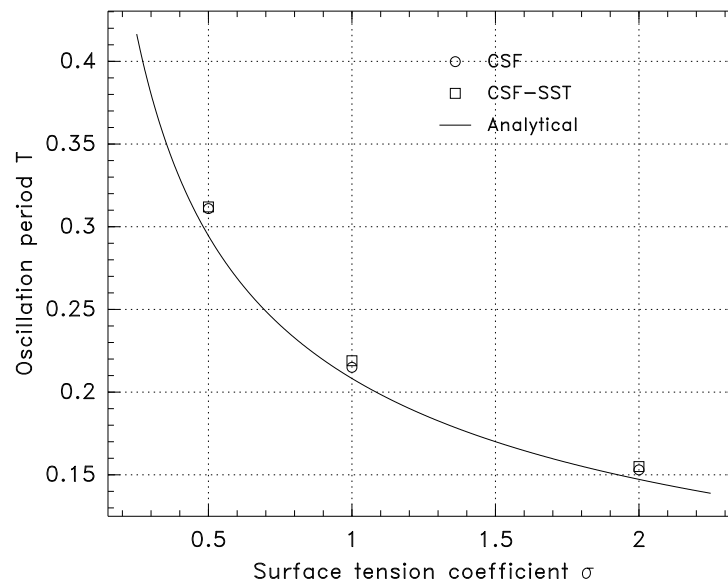


Figure 5.8: Droplet oscillation period obtained from the SPH simulation as a function of the surface tension coefficient; results compared to the analytical solution (5.32).

where n is the mode of oscillation. For $n = 2$, corresponding to our case, the theoretical oscillation period is

$$T = 2\pi \sqrt{\frac{R^3 \rho_D}{6\sigma}}. \quad (5.32)$$

Simulations were performed for $N = 120 \times 120$ particles, initially homogeneously distributed in the domain, $h/\Delta r = 2$ and the Wendland kernel (2.11). As in the case of square-droplet deformation, the influence of surface tension can be described by the Weber number $We = \rho_D R u^2 / \sigma$ and the capillary number $Ca = \mu_D u / \sigma$. Here, we chose $Ca^2 / We = \mu_D^2 / R \sigma \rho_D = 0.055$. The capillary number, based on u_0 , was 0.065. The evolution of particle distributions obtained with CSF and CSF-SST models is presented in Fig. 5.6. All results are suitably normalised by the droplet radius R in space and the theoretical value of period T (5.32) in time. In the case of the CSF-SST method, as in the square-droplet deformation test, some artifacts caused by numerical instabilities are visible close to the interface.

Figure 5.7 presents oscillation of the centre of mass position of the droplet's upper right quarter (normalised with R). Since the CSF method is not conservative, there is small fluctuation of the centre of mass evidenced by a slight shift of the point of intersection of x and y components. This effect is not noticeable in the CSF-SST method. What is more, despite the presence of instabilities in the flow, this method is stable.

To validate the correctness of the CSF and CSF-SST formulations, we compared the oscillation period calculated using the SPH method with the theoretical result (5.32). Figure 5.8 shows the droplet oscillation period as a function of the surface tension coefficient. In both methods, the results show very good agreement with the reference data.

5.6 Conclusions

Validation of surface-tension models, performed with the square-droplet deformation and the droplet oscillation test cases, shows that these phenomena can be very accurately predicted with the Smoothed Particle Hydrodynamics method. Both the CSF and CSF-SST techniques show a very good agreement with the reference data. The first approach (CSF) involves the estimation of the curvature and then computation of the surface-tension force from Eq. (5.19). This method is very stable, but it suffers from the lack of exact conservation of linear and angular momentum. The second approach (CSF-SST) uses the gradient of stress tensor to estimate the surface-tension force. It is a fully conservative approach but potentially unstable. Therefore, for time consuming tests like 3D bubbles rising in water (cf. Chapter 6), we decided that it is safer to use the CSF approach.

Chapter 6

Simulations of bubbles rising through liquids using SPH¹

6.1 Introduction

Bubble rising through viscous liquids is one of the most common gas-liquid flow phenomena (Brennen, 2005) and, as such, is encountered in various industrial processes. For that reason, the dynamics of rising bubbles has been the subject of many numerical and experimental investigations and there is an ongoing need to develop numerical methods well-suited for capturing the intricate details of these bubbly flows.

Up to now, the vast majority of CFD studies carried out to address this issue have been based on Eulerian approaches. These methods are, generally, accurate but present the inconvenience of having to reconstruct additionally the location of the gas-liquid interface within computational cells. Yet, some Eulerian methods have been shown to be very accurate for two-phase flow simulations with sharp interfaces. The most commonly known approach is the Volume of Fluid (VOF) method (Hirt and Nichols, 1981), which is conceptually simple and accounts very well for topological changes of the interface. For the simulation of bubbles, Van Sint Annaland et al. (2005) proposed a new three-dimensional VOF algorithm that determines interface locations based on a piecewise linear interface representation. Later, Bonometti and Magnaudet (2006) studied the transition of spherical cap bubbles to toroidal ones using VOF with an interface-capturing method for two-phase flows. The most recent Eulerian simulations of single bubble dynamics were performed by Hua and Lou (2007) and Hua et al. (2008) using Front Tracking (FT) algorithm and by Pianet et al. (2010) using the Smooth VOF technique. In all these papers, the authors have validated their method against the experiments of Bhaga and Weber (1981).

Numerical studies of single bubble dynamics have also been performed using the Lattice Boltzmann Method (LBM) approach. For example, Sankaranarayanan et al. (2003, 1999) used a multi-component method to simulate bubble dynamics and

¹The original material presented in this chapter has been published as: K. Szewc, J. Pozorski, J-P. Minier, 'Simulations of single bubbles rising through viscous liquids using Smoothed Particle Hydrodynamics', *Int. J. Multiphase Flow.* **50** (2013) 98-105.

validated their results by comparison with a front-tracking finite-difference method. For very low Reynolds numbers, other LBM simulations were performed by Takada et al. (2000) and Frank et al. (2006) where the free energy model was used while Amaya-Bower and Lee (2010) also presented results for single rising gas bubbles using LBM based on the Cahn-Hilliard diffuse interface approach.

In Section 6.2, the dynamics of single bubbles rising through a liquid is studied using the Smoothed Particle Hydrodynamics (SPH) approach. To the best of our knowledge, SPH has not yet been widely used for two-phase flows and there is still a lack of proper validation for fully three-dimensional multiphase flows with high density ratios, further compounded by surface tension and gravitation force influence. The only exception is the paper of Das and Das (2009) who simulated bubbling in a stagnant liquid pool through a submerged orifice.

However, in the most practical problems, bubbles do not move as a single, but rather large groups of moving bubbles. Dealing with such issues as boiling phenomena, where typically bubbles move collectively, there is a need to investigate the usefulness of the SPH approach to simulate such dense bubble swarms. Therefore, in the Section 6.3, we decided to validate SPH to simulate the process of bubble coalescence caused by the interaction through wake.

The bubble rising case (for $\mu_G/\mu_L \rightarrow 0$ and $\rho_G/\rho_L \rightarrow 0$) is fully described by two dimensionless quantities: the Eötvös number ($E\ddot{o}$) and the Morton number (Mo), defined as

$$E\ddot{o} = \frac{gD^2\rho_L}{\sigma}, \quad (6.1)$$

$$Mo = \frac{g\mu_L^4}{\rho_L\sigma^3}, \quad (6.2)$$

where D is the diameter of an initially spherical bubble, while ρ , μ , σ and g are, respectively, the density, dynamic viscosity, surface tension coefficient and the acceleration of gravitation. The subscripts L and G denote respectively liquid and gas phase. Therefore, the bubble shape and the Reynolds number Re , defined as

$$Re = \frac{\rho_L DU_T}{\mu_L}, \quad (6.3)$$

where U_T its terminal rising velocity, are fully determined from the set of $E\ddot{o}$ and Mo numbers. The bubble shape and Re are obtained from the simulation and can be further assessed with respect to experiments and compared with predictions of other numerical models.

In this chapter, the SPH multiphase flow model is used with the Hu and Adams (2006) formulation to properly handle large density differences, cf. Sect. 4.1.3. The surface tension is modelled using the Continuum Surface Force method, cf. Section 5.3. We present simulation results for the bubble velocity, the drag coefficient C_D and the topological changes of bubbles as they rise through viscous liquid for different regimes. The SPH results are validated against the experimental data of Bhaga and Weber (1981) and compared with other numerical results obtained with Front Tracking (Hua et al., 2008) and Lattice Boltzmann Method (Amaya-Bower and Lee, 2010; Cheng et al., 2010).

Table 6.1: The physical parameters and bubble shapes for the considered validation cases, following the experiment of Bhaga and Weber (1981).

Case	$E\ddot{o}$	Mo	Shape
A	17.7	711	oblate ellipsoidal
B	32.2	$8.2 \cdot 10^{-4}$	oblate ellipsoidal (disk)
C	243	266	oblate ellipsoidal (cap)
D	115	$4.63 \cdot 10^{-3}$	spherical cap

6.2 Single bubbles

Table 6.1 provides the values of $E\ddot{o}$ and Mo numbers describing the cases used for the validation purposes. To reduce the overall computational effort, the number of cases, for which the comparison with other methods and with experimental data has been investigated, has been limited to four. Each of these cases correspond to cases from the paper of Bhaga and Weber (1981), Fig. 2(b-e), and it can be seen that these four cases represent a wide range of shape regimes.

For all the cases considered, a regular domain with the edges of lengths $L_x = L_y = L$ and $L_z = 1.2L$, has been taken. The gaseous particles are initially located at

$$\left(x - \frac{L_x}{2}\right)^2 + \left(y - \frac{L_y}{2}\right)^2 + \left(z - \frac{L_z}{4}\right)^2 < \left(\frac{D}{2}\right)^2 = \left(\frac{L}{2\alpha}\right)^2, \quad (6.4)$$

while the liquid particles fill the remaining space. Parameter α is the ratio of the domain width L and the bubble diameter D . Such a parametrisation helps to perform the sensitivity analysis with respect to the wall confinement effect. The gas-liquid density and viscosity ratio are respectively $\rho_L/\rho_G = 1000$ and $\mu_L/\mu_G = 100$. Simulations have been performed using the optimal kernel properties proposed in Ch. 3 (Szewc et al., 2012a): the Wendland kernel (2.11) and $h/\Delta r = 2$, where Δr is a measure of the inter-particle distance (initial distance between particles). The liquid is weakly compressible ($\gamma = 7$) but the gaseous phase is treated as compressible with $\gamma = 1.4$ in Eq. (2.36). Comparing different 2D and 3D SPH simulations of rising bubbles with results obtained using other numerical methods, cf. Sect. 4.2 we have found $\varepsilon = 0.5$ as an optimal value. For this value neither particle mixing nor unphysical topology changes have been observed. At the boundary, the no-slip condition is assured by the Ghost-Particle method (cf. Sect. 2.5).

First, we decided to perform the standard validation test involving a stationary bubble submerged in a liquid (no gravitation force). From the Laplace law, the pressure inside the bubble must be higher than in the surrounding fluid and should undergo a jump across the interface

$$\Delta p = \frac{4\sigma}{D}, \quad (6.5)$$

for the spherical bubbles. Since the considered case is stationary, there is no problem with micro-mixing phenomena. Therefore, we decided to simulate the case A with ($\varepsilon = 0.5$) and without ($\varepsilon = 0$) the interface sharpness correction, cf. Fig 6.1. The simulations have been performed for $N = 80 \times 80 \times 96$ ($N_x \times N_y \times N_z$) particles in

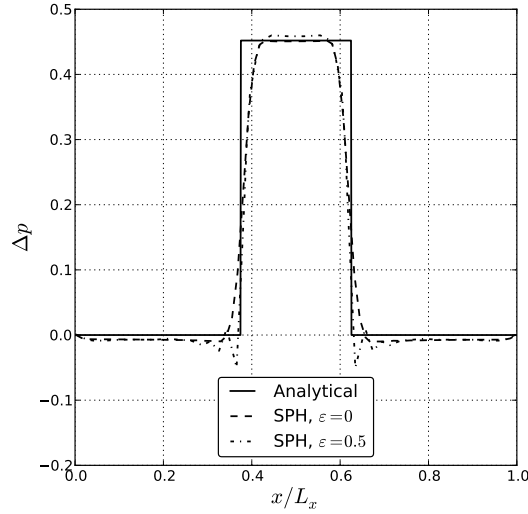


Figure 6.1: Comparison of pressure profiles, through a centre of stationary bubble (case A), between analytical solution and SPH computations with $\epsilon = 0.5$ and without $\epsilon = 0$ the interface sharpness correction procedure.

the domain. The presented results show that for both cases the SPH approach predicts the pressure jump very accurately. However, in the case of $\epsilon = 0.5$ some small artefacts are noticeable close to the interface; this is a result of additional repulsive force applied there.

Next, we evaluated the influence of the number of particles $N = N_x \times N_y \times N_z$ (resolution) on the prediction of the Reynolds number Re , the statistical error σ_{Re} and the computational time (for $\alpha = 4$), cf. Fig. 6.2. Since SPH is Lagrangian method, the particles change their positions during simulation. Therefore, the mean Reynolds number, computed after obtaining the steady-state solution, suffers from the random error σ_{Re} from about 4% for $N = 60 \times 60 \times 72$ down to 1.5% for $N = 100 \times 100 \times 120$. The simulations, parallelised to eight threads on AMF FX-8120 processor, took from 24 h for $N = 60 \times 60 \times 72$ up to 112 h of CPU time for $N = 100 \times 100 \times 120$ particles. Weighting between accuracy and computational time, we have decided to use $N = 100 \times 100 \times 120$ particles in the domain.

Next, to study the wall confinement effect, we checked the influence of the domain size on the bubble terminal rising velocity. Figure 6.3 shows the prediction of the Reynolds number for the case B (for which the domain width has the biggest impact on the terminal velocity), for different values of parameter α . Similarly to other authors, eg. Hua et al. (2008) or Amaya-Bower and Lee (2010), our analysis shows that the domain size is sufficient for the bubble rising simulations without confinement effects. All subsequent simulations have been performed with $\alpha = 5$, for there is no notable change in the predicted Reynolds number as the parameter α is increased beyond this value.

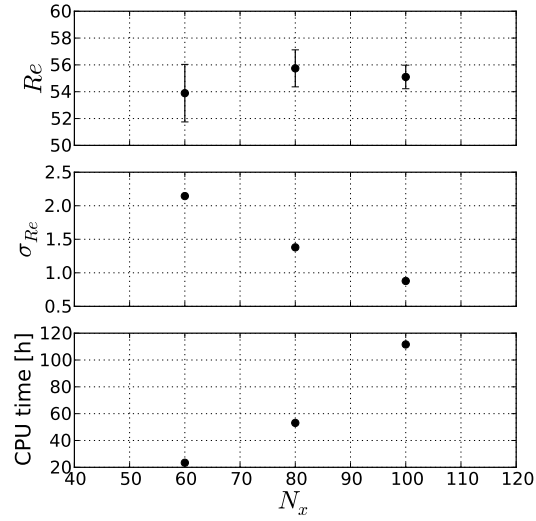


Figure 6.2: The effect of number of particles $N = N_x \times N_y \times N_z$ (spatial resolution) on the prediction of the Reynolds number Re , the random error σ_{Re} and the computational time; simulations preformed at $E\ddot{o} = 32.2$ and $Mo = 8.2 \cdot 10^{-4}$ (case B).

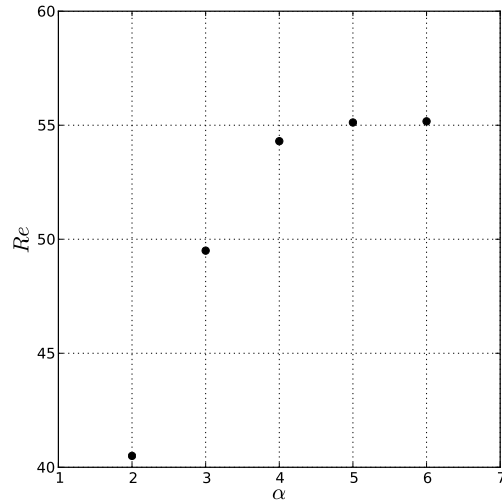


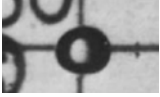



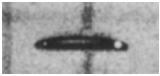



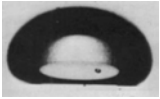






Figure 6.3: Sensitivity analysis of the wall confinement effect on the prediction of the Reynolds number for $E\ddot{o} = 32.2$ and $Mo = 8.2 \cdot 10^{-4}$ (case B). Parameter α denotes the width of the computational domain measured in number of bubble diameters D , $\alpha = L/D$.

Table 6.2: Comparison of 3D SPH simulation results with Front-Tracking by Hua et al. (2008), Lattice Boltzmann Method by Amaya-Bower and Lee (2010) and experiment by Bhaga and Weber (1981).

Case	SPH	FT	LBM	Experiment
A			no reference data	
B				
C				
D				

6.2.1 Shape

The results of 3-D SPH simulations are summarised in Table 6.2 which provides a comparison of present results with the reference data. The second column contains both the 3-D image of bubble composed of the SPH particles which represent the gaseous phase, and the 2-D cross-section through the center of bubble presenting the position of the interface defined as the surface of $c = 0.5$. The 3rd and 4th columns contain the images of the bubble shapes obtained with respectively FT (Hua et al., 2008) and LBM (Amaya-Bower and Lee, 2010). The last column provides the photographs of the final bubble shapes by Bhaga and Weber (1981). This comparison shows that the SPH approach is in a very good qualitative accordance with the reference data. Furthermore, it is seen that the SPH method can give accurate solutions even for cases corresponding to higher Re number and strong deformations (cf. case D) where, unfortunately, the LBM method has been reported to fail. A more quantitative comparison of the SPH and the front tracking is shown in Figure 6.4. It presents the interface position (2D cross-sections through the centre of bubble) calculated for the case C using both approaches. This comparison shows that the SPH approach is, for such cases, in good agreement with the front tracking method.

On the other hand, the main weakness of the SPH approach is the necessity of avoiding spurious fragmentation of the interface. Choosing too low a value of the sharpness control parameter ε in Eq. (4.34) may result in a completely wrong

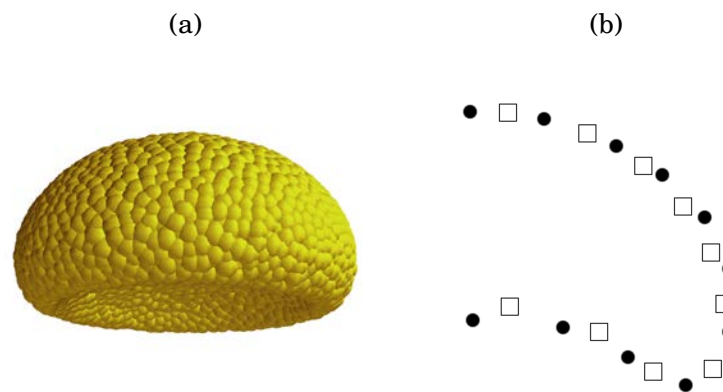


Figure 6.4: SPH simulation of rising bubble at $Bo = 243$ and $Mo = 266$ (case C); (a) rendered air bubble, (b) comparison of the interface position (vertical cross-section through the centre of bubble) for SPH (\bullet) and the front tracking method by Hua et al. (2008) (\square).

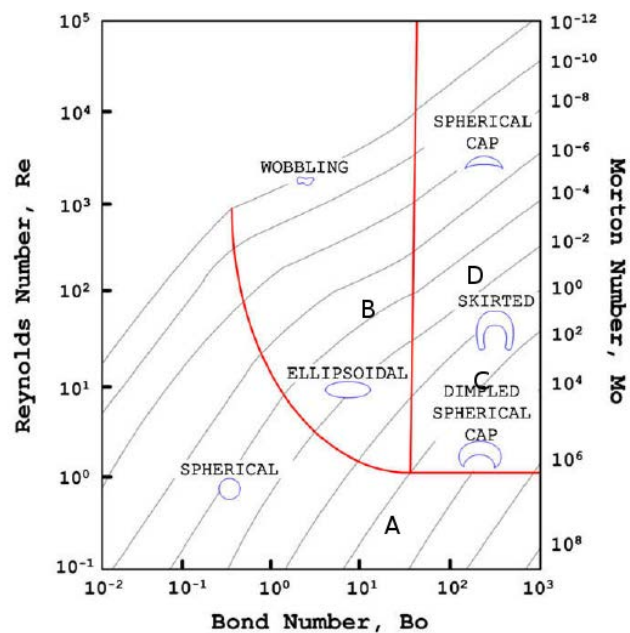


Figure 6.5: Shape regime map; from the paper of Amaya-Bower and Lee (2010); calculated cases are indicated on the map.

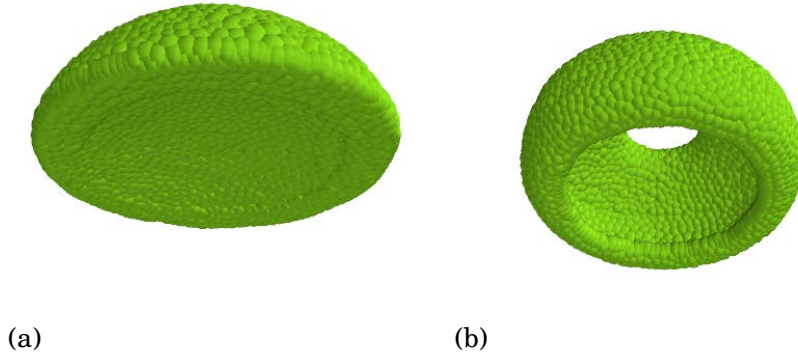


Figure 6.6: SPH simulations of rising bubble at $E\ddot{o} = 115$ and $Mo = 4.63 \cdot 10^{-3}$: (a) expected solution, (b) too low value of the sharpness control parameter ε in Eq. (4.34).

bubble evolution, as presented in Fig. 6.6. It is very interesting to note that this wrong solution is very similar to the one obtained by LBM.

6.2.2 Terminal velocity

In the present work, bubble rising velocities have been calculated using the formula

$$\mathbf{U} = \frac{1}{N_{\text{gas}}} \sum_{a \in \text{gas}} \mathbf{u}_a, \quad (6.6)$$

where N_{gas} denotes a number of gaseous particles.

Figure 6.7 displays these bubble rising velocities calculated by the SPH approach and expressed as a dimensionless quantity, $U^* = U(\rho_L D / \mu)$, in terms of the dimensionless time, $t^* = t\sqrt{g/D}$. Numerical results are presented for the evolution of U^* as a function of time and it is seen that a steady-state, or terminal velocity, is reached. A special attention should be paid to the cases of high Reynolds number (B and C), where, at the beginning of simulations, oscillations of rising (or vertical) velocity can appear. This behaviour is due to the interface sharpness correction procedure. For high Reynolds flows, respectively higher repulsive force shall be placed on the interface which leads to velocity field oscillations at the initial phase of motion. This behaviour, however, has no significant effect on the field quantities and the dynamics of bubble at a later stage of rising. Table 6.3 presents the predicted Reynolds numbers obtained with the present SPH method as well as for other numerical methods and are compared to experimental evidence. The largest inconsistency, which has been obtained for the case D, compared to the experimental data, is limited to 7%. This appears as very good results since, by comparison, the discrepancies of FT and LBM can go up to 25%.

6.2.3 $C_D - Re$ correlation

It is often more practical to compute drag coefficient which can be expressed in the form

$$C_D = \frac{4gD}{3U_T^2} = \frac{4E\ddot{o}^{\frac{3}{2}}}{3Re^2 Mo^{\frac{1}{2}}}. \quad (6.7)$$

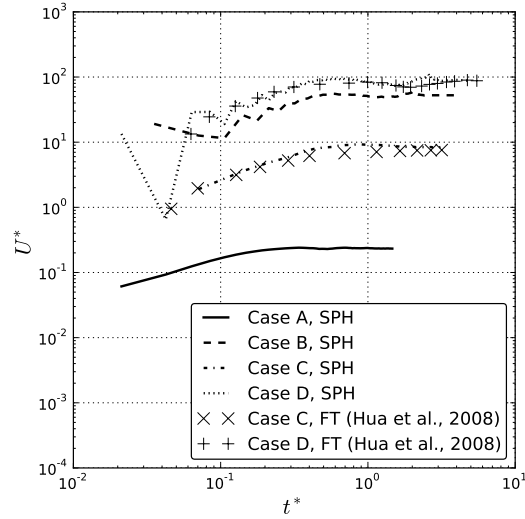


Figure 6.7: Normalised bubble rise velocities, predicted using SPH, for the cases A-D.

Table 6.3: Comparison of the Reynolds numbers (based on the terminal velocity) computed using SPH, FT (Hua et al., 2008), LBM (Amaya-Bower and Lee, 2010) and experiment (Bhaga and Weber, 1981).

Case	SPH	FT	LBM	Experiment
A	0.232	0.182	-	0.232
B	55.1	54.8	51.7	55.3
C	8.15	7.6	6.2	7.77
D	88.0	89.6	78.9	94.0

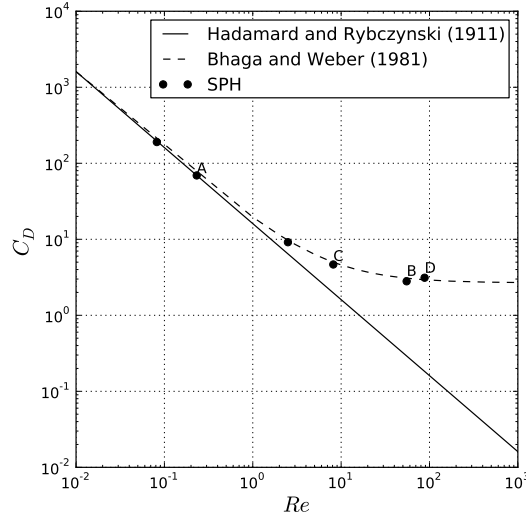


Figure 6.8: Drag coefficient - Reynolds number relationship comparison between the SPH solution, the analytical solution for nearly spherical bubbles by Hadamard (1911) and Rybczynski (1911) and the experimental correlation by Bhaga and Weber (1981).

It is important to note that C_D is usually presented as a function of Re (which, in turn, depends on $E\ddot{o}$ and Mo).

For spherical or nearly-spherical bubbles, the drag coefficient can be predicted by Hadamard (1911) and Rybczynski (1911) theory. Assuming that $\mu_G/\mu_L \rightarrow 0$ and $\rho_G/\rho_L \rightarrow 0$, the Hadamard-Rybczynski equation can be expressed as

$$C_D = 16/Re. \quad (6.8)$$

Even for non-spherical bubbles, provided that the Morton number is greater than $Mo = 4 \cdot 10^{-3}$, the drag coefficient C_D and the bubble shape depend only on the Reynolds number; Bhaga and Weber (1981) proposed the experimental correlation in this regime

$$C_D = (2.67^{0.9} + (16/Re)^{0.9})^{1/0.9}. \quad (6.9)$$

Figure 6.8 presents the numerical results obtained with the SPH method compared to both (6.8) and (6.9) correlations. The comparison has been performed by calculating C_D via the analytical relation (6.7). It is seen that SPH solutions show very good comparison with both experimental results and analytical formula (in the range of applicability of the model). Also, as reported by many workers (Bhaga and Weber, 1981), the limit $C_D = 2.67$ for $Re \gtrsim 100$ is confirmed here.

6.3 Bubble-bubble interaction

Since in the most of practical problems, bubbles do not move as a single, but rather in large groups of moving bubbles, we decided to consider here the simple case of a bubble-bubble interaction: two bubbles of the same volume interacting

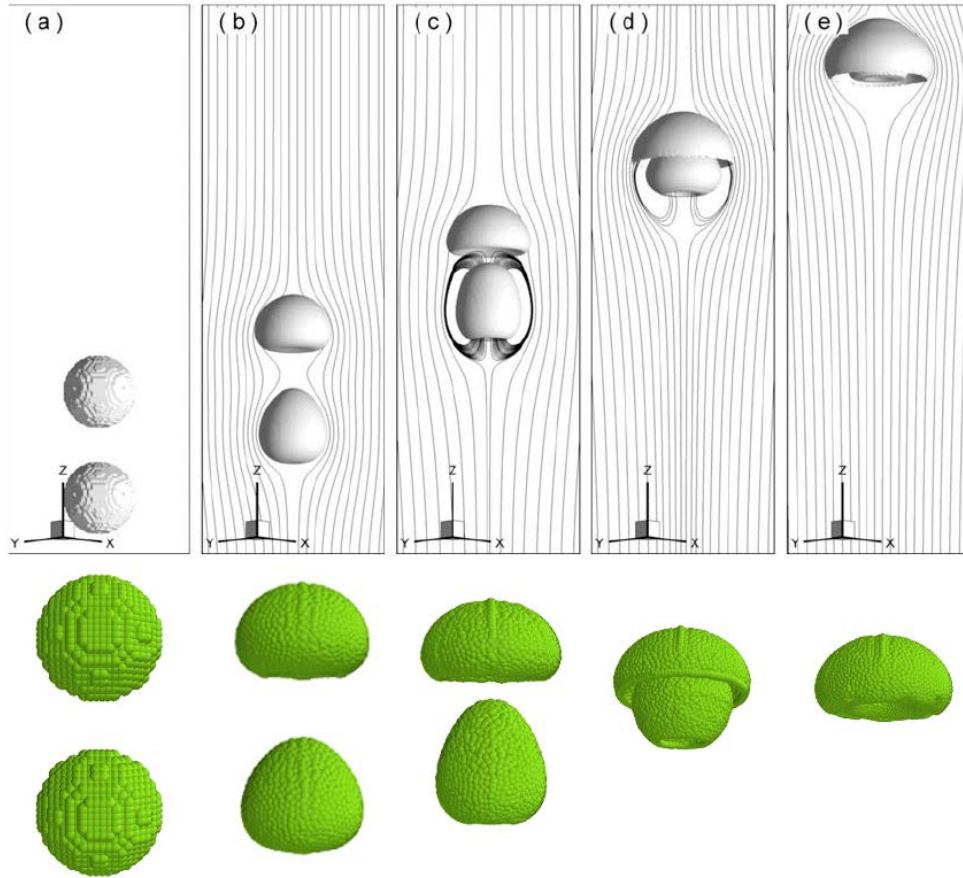


Figure 6.9: LBM (upper) and SPH (lower) simulations of bubble shapes evolution for the coalescence of two bubbles at times: (a) $t = 0.0$, (b) $t = 2.4$, (c) $t = 4.8$, (d) $t = 7.2$, (e) $t = 9.6$; LBM results obtained by Cheng et al. (2010).

through the wake. For problem considered here, a regular domain with the edges of lengths $L_x = L_y = L$ and $L_z = 2.0L$, has been taken. Two spherical bubbles with the same diameter $D = 0.2L$ are initially placed at the vertical positions $z = 1.5D$ and $z = 3D$. In this case, as for the single bubbles, the gas-liquid density and viscosity ratio are respectively $\rho_L/\rho_G = 1000$ and $\mu_L/\mu_G = 100$. Simulations were performed with $N = 80 \times 80 \times 160$ particles in the domain. The liquid is treated as weakly compressible, while the gaseous phase as compressible fluid. The no-slip condition is applied at the boundary. The results of bubble coalescence simulation, qualitatively compared to the results obtained by Cheng et al. (2010) using LBM, are presented in Fig. 6.9. Bubbles start to rise due to the buoyancy force and a wake is formed behind each bubble. Both interact through the wake which results in a stretch deformation (vertical direction) of lower bubble, cf. Fig. 6.9(c). The lower bubble also rises faster. Finally, cf. Fig. 6.9(d), the bubbles coalesce to form one big bubble. Figure 6.10 displays the time-history of mean bubble rising velocities calculated using the SPH approach expressed as dimensionless quantities (as in the case of single bubbles). Obtained results are compared with the LBM simulations by Cheng et

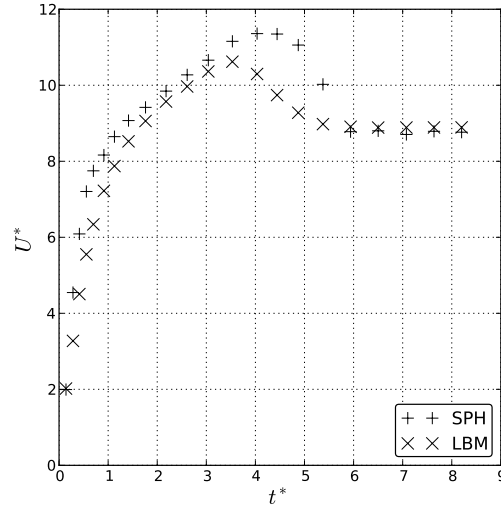


Figure 6.10: Comparison of the rise velocity for coalescence of two bubbles simulated using SPH and LBM Cheng et al. (2010).

al. (2010). Evolution of the mean rising velocity, in particular, the terminal rising velocity obtained using both methods are very close to each other. However, the LBM result shows that the maximum mean velocity occurs at $t^* = 3.5$. In the case of the SPH approach, the maximum mean velocity occurs at $t^* = 4$. Unfortunately, there is no evidence which method gives a result closer to reality. Therefore, further studies on the simulations of bubble-bubble interaction using the SPH approach (as well as with other methods) are necessary.

6.4 Conclusions

In the present chapter, the usefulness of the SPH approach to capture the intricate details of bubbles rising in a fluid was demonstrated. The first, fully 3D, SPH studies on the dynamics of rising bubbles through viscous fluids were presented. For that purpose, a multi-phase SPH formulation that can address large density differences was retained, while surface tension effects were explicitly accounted for through the CSF model. Numerical simulations were performed for different regimes (corresponding to different relative importance of surface tension, viscosity and buoyancy effects) and the predicted topological changes as well as terminal velocity and drag coefficients of bubbles were compared to the experimental and other numerical data, namely the Front-Tracking and the Lattice Boltzmann methods. This comparison showed very good agreement with the reference approaches. However, since in many situations bubbles typically move collectively, there is still need to investigate the usefulness of the SPH approach to simulate dense bubble swarms. Our first results, involving two bubble interaction through wake are very promising, but, further, detailed analysis is necessary.

Chapter 7

Heat transfer modelling using SPH

7.1 Introduction

Simulations of heat transfer are very important in many industrial, geophysical and astrophysical problems. In most of cases, the geometry of the flow is complicated and materials are not homogeneous. Due to these inconveniences, the Lagrangian framework of Smoothed Particle Hydrodynamics gives here a big advantage over Eulerian methods. In Section 7.2 a short introduction to the SPH implementation of heat transfer phenomena is presented. A new SPH form of energy equation is also introduced and validated for heat transfer in homogeneous and inhomogeneous slabs. Section 7.3 presents an extensive discussion about the natural convection phenomena. The usefulness of the Boussinesq approximation is also discussed and a new variant of the Smoothed Particle Hydrodynamics (SPH) simulations of natural convection is introduced. In many situations, where the density may vary significantly under the influence of temperature non-uniformities, the classical Boussinesq approximation fails. To characterise such situations, the Gay-Lussac dimensionless number is useful as a measure of density variations in non-isothermal flows. The novel points of the proposed modelling beyond the Boussinesq regime include the proper implementation of the buoyancy force and a smart connection between particle volume and incompressibility constraint. To examine the correctness of the new approach, numerical results are confronted with available reference data.

7.2 Conduction modelling

A general form of the energy equation (without phase change) for fluid flow may be written as

$$\rho \frac{de}{dt} = \nabla \cdot (k \nabla T) - p(\nabla \cdot \mathbf{u}) - (\tau \nabla \mathbf{u}) + Y, \quad (7.1)$$

where e is the internal (thermal) energy, T is temperature, k is thermal conductivity, τ is the viscous stress tensor and Y is a source of energy (for example: the absorbed radiation).

Assuming that the fluid is incompressible, the heat production due to viscous dissipation is negligible, and finally that there is no external source of energy, Eq. (7.1) can be reduced into the form

$$\rho \frac{de}{dt} = \nabla \cdot (k \nabla T). \quad (7.2)$$

To rewrite it in terms of the temperature, it is natural to use the relation defining the specific heat capacity c_p

$$\rho c_p \frac{dT}{dt} = \nabla \cdot (k \nabla T). \quad (7.3)$$

For constant conductivity k , the energy equation arises into the following form

$$\frac{dT}{dt} = \left(\frac{k}{\rho c_p} \right) \Delta T = a \Delta T, \quad (7.4)$$

where a is the thermal diffusivity coefficient.

After Cleary and Monaghan (Cleary, 1998; Cleary and Monaghan, 1999), the simplified energy equation, Eq. (7.3), in the SPH form may be expressed as

$$\frac{dT_a}{dt} = \frac{4}{\rho_a c_{pa}} \sum_b \frac{k_a k_b}{k_a + k_b} \frac{T_{ab} \mathbf{r}_{ab}}{r_{ab}^2 + \eta^2} \cdot \nabla_a W_{ab}(h) \Omega_b, \quad (7.5)$$

where $T_{ab} = T_a - T_b$.

However, in the present work, we decided to introduce a new SPH form of Eq. (7.3), which, based on the Hu and Adams (2006) formalism, is constructed on the basis of normalised kernels. Using the centrally inter-particle-averaged gradient formula, cf. Eq. (4.17), the divergence of conductive heat flux $k \nabla T$ can be expressed in the SPH formalism as

$$\langle \nabla \cdot (k \nabla T) \rangle_a = \Theta_a \sum_b \left(\frac{1}{\Theta_a^2} + \frac{1}{\Theta_b^2} \right) \overline{(k \nabla T)_{ab}} \cdot \nabla_a W_{ab}(h). \quad (7.6)$$

The term $\overline{(k \nabla T)_{ab}}$ can be obtained using the idea proposed by Cleary and Monaghan (1999). Performing the simple one-dimensional finite-difference analysis, Cleary and Monaghan showed that the approximated formula

$$\overline{(k \nabla T)_{ab}} \approx \frac{2k_a k_b}{k_a + k_b} \frac{T_{ab} \mathbf{r}_{ab}}{r_{ab}^2} \quad (7.7)$$

ensures the continuity of heat flux across material interfaces. Inserting (7.7) into (7.6), the simplified energy equation, Eq. (7.3), achieves the form

$$\frac{dT_a}{dt} = \frac{2}{m_a c_{pa}} \sum_b \frac{k_a k_b}{k_a + k_b} \left(\frac{1}{\Theta_a^2} + \frac{1}{\Theta_b^2} \right) \frac{T_{ab} \mathbf{r}_{ab}}{r_{ab}^2 + \eta^2} \cdot \nabla_a W_{ab}(h), \quad (7.8)$$

where η , as in the case of Eq. (2.34), is added to avoid potential singularities.

7.2.1 Heat conduction in slabs

The simplest configuration that allows us to assess the new SPH formulation of heat transfer is a finite, one-dimensional slab of size L , where two opposite sides (left and right) have fixed temperatures T^l and T^r , respectively. For the testing purposes, two qualitatively different cases are considered here: homogeneous and inhomogeneous (in the sense of material properties). In the homogeneous case, the thermal diffusivity is $a = 0.001$. In the inhomogeneous case, the slab is divided at $x = 0.5L$ into two parts (left and right) with different material properties: $c_v^r/c_v^l = 1.5$, $k^r/k^l = 3$, $\rho^r/\rho^l = 2$ (the thermal diffusivity is chosen equal for both sides $a^r = a^l = 0.001$). For both cases considered here $T^r - T^l = 1$. The initial temperature distribution in the slab is presented in Figs. 7.1(left) and Figs. 7.2(left). For both cases, the approximate analytical solution, obtained for infinite slabs, is (Carslaw and Jaeger, 1965)

$$T = T^l + T^c \begin{cases} \operatorname{Erfc}\left(\frac{0.5-x}{2\sqrt{a^l t}}\right), & \text{if } x < 0.5, \\ 1 + \frac{k^l}{k^r} \sqrt{\frac{a^r}{a^l}} \operatorname{Erf}\left(\frac{x-0.5}{2\sqrt{a^r t}}\right), & \text{if } x > 0.5, \end{cases} \quad (7.9)$$

where

$$T^c = \frac{k^r/\sqrt{a^r}}{k^r/\sqrt{a^r} + k^l/\sqrt{a^l}} (T^r - T^l). \quad (7.10)$$

The SPH simulations were performed using Eq. (7.8) and the resolution $N = 40$ particles, initially homogeneously distributed in the domain ($h/\Delta r = 2$).

The temperature profiles of the SPH computations compared to the analytical solutions are presented in Figs. 7.1(right) and Figs. 7.2(right). All presented quantities are normalised so that

$$x^* = \frac{x}{L}, \quad t^* = \frac{t}{L^2/a}, \quad T^* = \frac{T - T_l}{T_r - T_l}. \quad (7.11)$$

The results were obtained at $t^* = 0.015$ (transient solution). For both cases the comparison of SPH with the analytical solution shows a very good accordance for both single and multi-component systems.

7.3 Natural convection¹

7.3.1 Introduction

Natural convection phenomena, due to their relevance to many scientific and technical issues such as nuclear reactor systems, foundry devices, geophysical and astrophysical processes, etc., have been intensively studied in the literature. In particular, due to geometrical simplicity, square and rectangular wall-heated cavities have been widely explored. The most-cited benchmark solutions were provided by De Vahl Davis (1983) using second-order central difference scheme. He

¹The original material presented in this section has recently been published as: K. Szewc, J. Porszski, A. Tanière, 'Modeling of natural convection with Smoothed Particle Hydrodynamics: Non-Boussinesq formulation', *Int. J. Heat Mass Trans.* **54** (2011) 4807-4816.

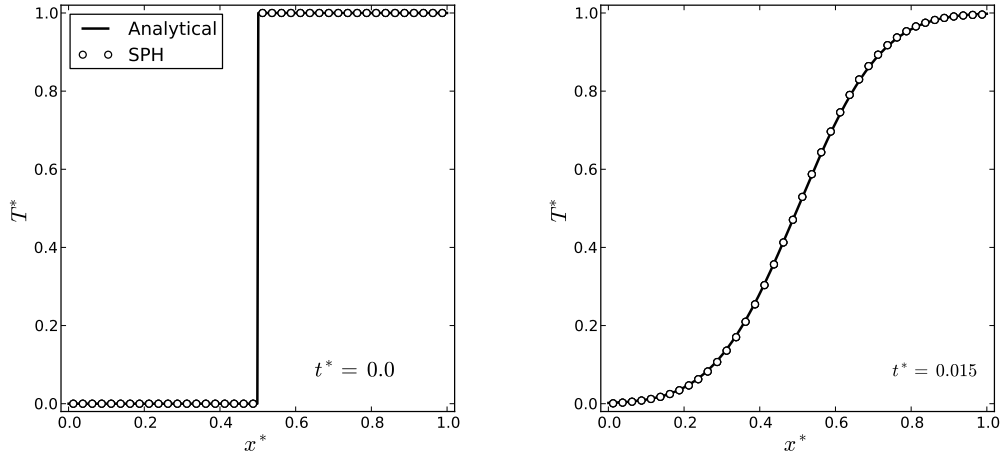


Figure 7.1: The SPH computations of temperature profile (dots) across the homogeneous slab ($\alpha = 0.001$) for: (left) initial state $t^* = 0$ and (right) $t^* = 0.015$; the analytical solutions (Carslaw and Jaeger, 1965) are given by the solid line; all the results expressed in the dimensionless form.

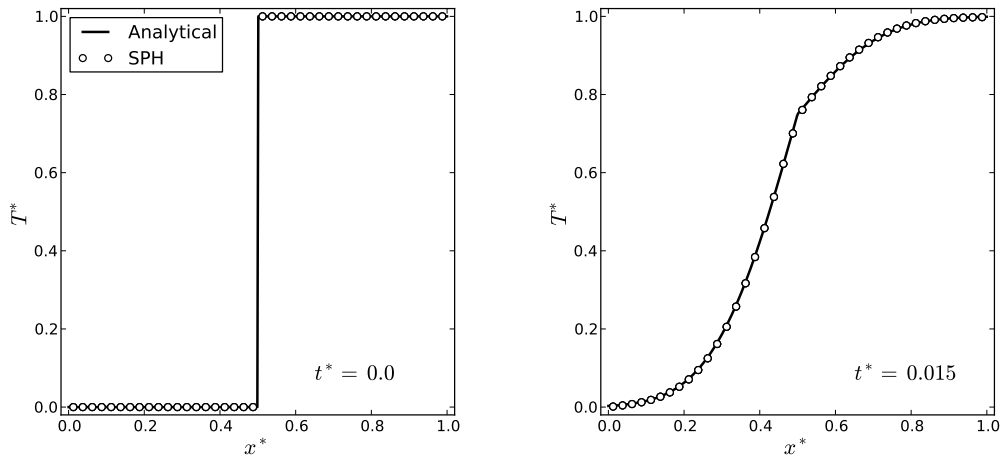


Figure 7.2: The SPH temperature computations (dots) across the inhomogeneous slab ($c_v^r/c_v^l = 1.5, k^r/k^l = 3, \rho^r/\rho^l = 2, \alpha^r = \alpha^l = 0.001$) for: (left) initial state $t^* = 0$ and (right) $t^* = 0.015$; the analytical solutions (Carslaw and Jaeger, 1965) are given by the solid line; all the results expressed in the dimensionless form.

performed simulations of steady-state natural convection in a horizontally-heated square cavity at the Rayleigh numbers up to $Ra = 10^6$. His studies were continued by numerous researchers to extend the range up to $Ra = 10^8$ by Le Quere (1991) and $Ra = 10^{11}$ by Lage and Bejan (1991). Evolution of the CFD methods led to benchmark solutions performed using other approaches such as Discrete Singular Convolution (DSC) by Wan et al. (2001) and the Lattice Boltzmann Method (LBM) by Kao and Yang (2007).

All the above-mentioned papers are based on the Boussinesq approximation. However, the natural convection is often driven by large temperature differences leading to considerable density variations. In these cases the Boussinesq approximation fails. This situation takes place in foundry processes and astrophysical MHD simulations. In the literature, papers dealing with the non-Boussinesq regime are rare. The square side-heated cavity simulations of natural convection caused by large density variations were performed in the compressible Eulerian approach by Pessa and Piva (2009), Vierendeels et al. (2004) and Becker and Braack (2002).

As briefly recalled in Sections 2.2 and 7.2, field quantities as density and temperature in SPH are modelled exactly at moving particles. Therefore, an implementation of the Boussinesq approximation in SPH is straightforward (Sec. 7.3.2). It is done by extending the Navier-Stokes equation with an additional term. The SPH simulations under Boussinesq approximation were presented by Cleary and Monaghan (1999). The novel SPH approach of performing simulations in the non-Boussinesq regime is described in Section 7.3.3. The key points of this technique are the proper implementation of the buoyancy force and a smart connection between particle volume and incompressibility constraint (WCSPH), cf. Sect. 7.3.3. This new approach is fully applicable for multiphase flows.

7.3.2 Boussinesq approximation

The most common implementation of natural convection is based on the Boussinesq approximation. It states that for small departures from the isothermal flow the fluid may still be treated as incompressible in the sense of independence of the pressure, but small density differences $\delta\rho$ may be caused by small temperature changes δT

$$\delta\rho = \left(\frac{\partial\rho}{\partial T}\right)_p \delta T = -\rho_0\beta\delta T, \quad (7.12)$$

where β is the coefficient of thermal expansion and

$$T = T_0 + \delta T, \quad (7.13)$$

$$\rho = \rho_0 + \delta\rho, \quad (7.14)$$

T_0 and ρ_0 being the initial temperature and density. The pressure field may be split into two parts

$$p = p_{\text{hs}} + \delta p, \quad (7.15)$$

where δp denotes the hydrodynamic pressure. The hydrostatic pressure p_{hs} at depth y (2D case), assuming no variation of density field, is given by relation

$$p_{\text{hs}} = \rho_0 g y + p_{\text{ref}}, \quad (7.16)$$

where p_{ref} is a reference pressure.

Let us consider the pressure term of the Navier-Stokes equation (2.18). Substituting from (7.13) and (7.14) and omitting higher order terms, we have (Landau and Lifschitz, 1987)

$$\frac{\nabla p}{\varrho} = \frac{\nabla p_{\text{hs}}}{\varrho_0} + \frac{\nabla \delta p}{\varrho_0} - \frac{\nabla p_{\text{hs}}}{\varrho_0^2} \delta \varrho. \quad (7.17)$$

Bringing together eqs. (7.12), (7.16) and (7.17), we write the Navier-Stokes equation into the common Boussinesq approximation form

$$\frac{d\mathbf{u}}{dt} = -\frac{\nabla \delta p}{\varrho_0} + \nu \Delta \mathbf{u} - \beta \mathbf{g} \delta T. \quad (7.18)$$

For the flow in the Boussinesq approximation, two relevant dimensionless quantities are: the Prandtl number

$$Pr = \frac{\nu}{\alpha}, \quad (7.19)$$

which describes the ratio of momentum to thermal diffusivity (fluid properties) and the Rayleigh number

$$Ra = \frac{g \beta \mathbb{L}^3 \Theta}{\nu \alpha}, \quad (7.20)$$

where \mathbb{L} and Θ are respectively a characteristic length scale and temperature difference. The value of Ra expresses the ratio between buoyancy and viscosity within the fluid for a given Prandtl number.

The SPH formulation of the Boussinesq approximation is straightforward. Except for the buoyancy term $-\beta \mathbf{g} \delta T$, there is no external force that comes into play in the Navier-Stokes equation. The pressure is governed by the equation of state (2.36), while the density and temperature are computed using eqs. (2.24) and (7.5).

7.3.3 Non-Boussinesq (general) regime

The Gay-Lussac number

Let us consider the situation where the temperature changes can no longer be assumed small. Then, the density field may vary significantly, which causes the three assumptions of Boussinesq approximation to become invalid. The first is the formula of hydrostatic pressure (7.16). Instead, the hydrostatic pressure at depth y should be calculated according to the relation

$$p_{\text{hs}}(x, y) = \int_0^y \varrho(x, y') g dy' + p_{\text{ref}}. \quad (7.21)$$

The second is the negligence of higher order terms in eq. (7.17). And the last one is the lack of influence of variable density on thermal diffusivity. In such a case, when the density is explicitly subject to temperature variations, an additional dimensionless quantity - the Gay-Lussac (Ga) number

$$Ga = \beta \Theta \quad (7.22)$$

should be introduced. This number describes the level of density variations caused by the temperature field. It may be shown (Pesso and Piva, 2009) that the Boussinesq approximation is retrieved as Ga goes to zero.

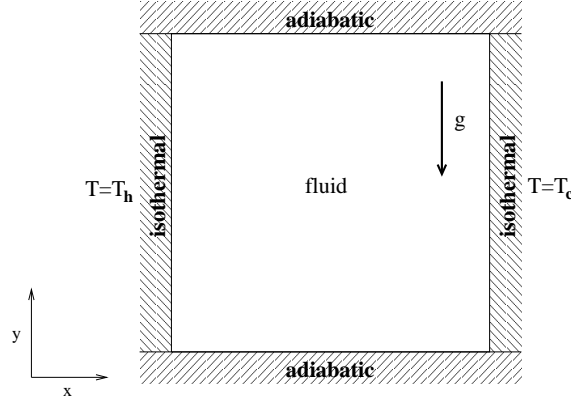


Figure 7.3: A scheme of a differentially heated square cavity.

SPH formulation

To simulate non-isothermal flows beyond the Boussinesq assumption using SPH, we suggest a new, more general formulation. At each time step, the density ρ is computed utilising relation (2.24). It is corrected next, due to changing temperature, by the common relation

$$\rho^{\text{cor}} = \rho(1 - \beta\delta T) \quad (7.23)$$

where δT is the difference between the local and reference temperature, eq. (7.13). Moreover, beyond the linearity of thermal expansion it is possible to use a general relation in the form

$$\rho^{\text{cor}} = f(\rho, \delta T). \quad (7.24)$$

In the case of SPH, the incompressibility constraint may be expressed in a smart way as the requirement of constant particle volumes Ω_a . In each time step it can be determined from

$$\Omega_a = \frac{1}{\sum_b W_{ab}(h)} = \frac{1}{\Theta_a}, \quad (7.25)$$

where Θ_a is the SPH measure of particle number density, cf. Sect. 4.1.3. Therefore, to compute the pressure we use modified equation of state (2.36)

$$p_a = \frac{c^2 \rho_0}{\gamma} \left[\left(\frac{\Omega_0}{\Omega_a} \right)^\gamma - 1 \right], \quad (7.26)$$

where only spatial distribution of particles is included.

After these steps, the Navier-Stokes equation (2.18), and the energy equation (7.5) are solved using the corrected density values only.

7.3.4 Flow in a differentially heated square cavity

Boussinesq approximation

A differentially heated square cavity is presented in Fig. 7.3. The left and right boundaries are isothermal, maintained respectively at T_c (cold) and T_h (hot); both horizontal walls are adiabatic. The governing equations in a non-dimensional form

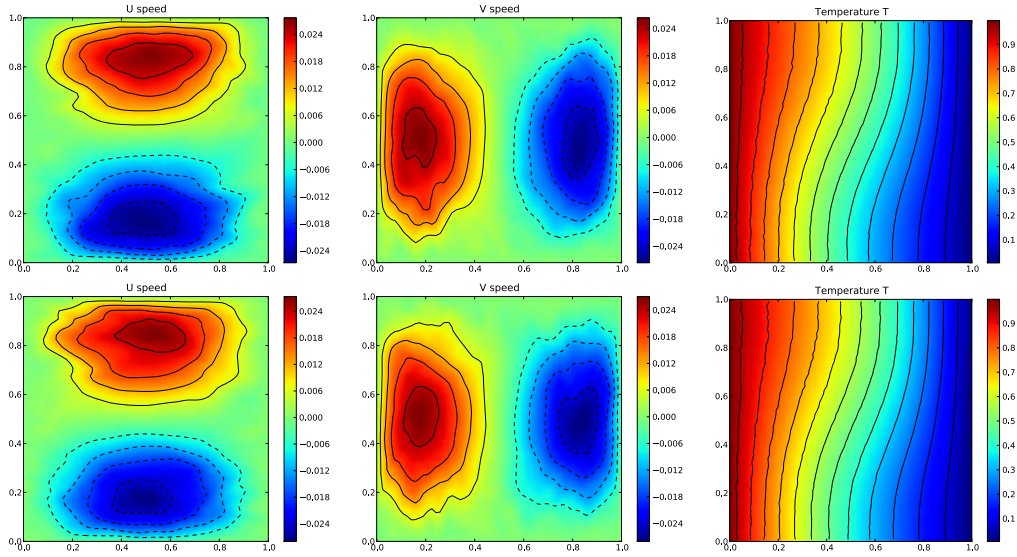


Figure 7.4: Horizontal velocity (left plots), vertical velocity (middle plots) and temperature field (right plots) for horizontally-heated square cavity at $Ra = 10^3$ and $Pr = 0.71$ (steady-state solution). Top plots: SPH with Boussinesq approximation; bottom plots: SPH with the new approach ($Ga = 0.071$).

are given as

$$\frac{\partial u_i^*}{\partial x_i^*} = 0, \quad (7.27)$$

$$\frac{\partial u_i^*}{\partial t^*} + u_j^* \frac{\partial u_i^*}{\partial x_j^*} = -\frac{\partial p^*}{\partial x_i^*} + Pr \frac{\partial^2 u_i^*}{\partial x_j^* \partial x_j^*} + RaPrT^* \delta_{i2} \quad (7.28)$$

$$\frac{\partial T^*}{\partial t^*} + \frac{\partial u_j^* T^*}{\partial x_j^*} = \frac{\partial^2 T^*}{\partial x_j^* \partial x_j^*}, \quad (7.29)$$

and

$$x_i^* = \frac{x_i}{L}, u_i^* = \frac{u_i L}{a}, p^* = \frac{pL^2}{\rho a^2}, t^* = \frac{tL^2}{a}, T^* = \frac{T - T_c}{T_h - T_c}. \quad (7.30)$$

where L is the size of the cavity, while the Rayleigh number is defined with $\mathbb{L} = L$ and $\Theta = T_h - T_c$, cf. Eq. (7.20).

In order to validate our methodology, natural convection in the differentially-heated cavity is studied at $Ra = 10^3$, 10^4 and 10^5 with $Pr = 0.71$. Simulations were performed using 900, 3600 and 8100 particles in the domain. Obtained results are compared with data provided by De Vahl Davis (1983), Kao and Yang (2007) and Wan et al. (2001). Figures 7.4, 7.5 and 7.6 show the velocity and temperature fields obtained using the Boussinesq approximation and with the new, general formulation. Independently of the Rayleigh number, both methods perform similarly. Since in the presented new approach the density varies, it is necessary to account for the Gay-Lussac Ga non-dimensional parameter in the flow picture. Data presented in Figs. 7.4, 7.5 and 7.6 were obtained for $Ga = 0.071$. In this regime density may vary about 7%, therefore it is still the Boussinesq regime.

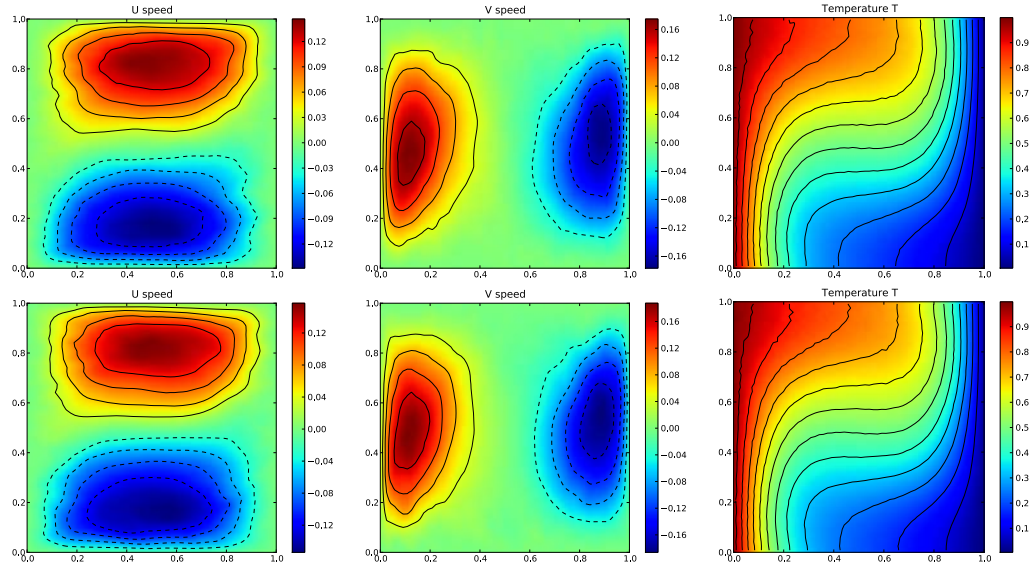


Figure 7.5: Horizontal velocity (left plots), vertical velocity (middle plots) and temperature field (right plots) for horizontally-heated square cavity at $Ra = 10^4$ and $Pr = 0.71$ (steady-state solution). Top plots: SPH with Boussinesq approximation; bottom plots: SPH with the new approach ($Ga = 0.071$).

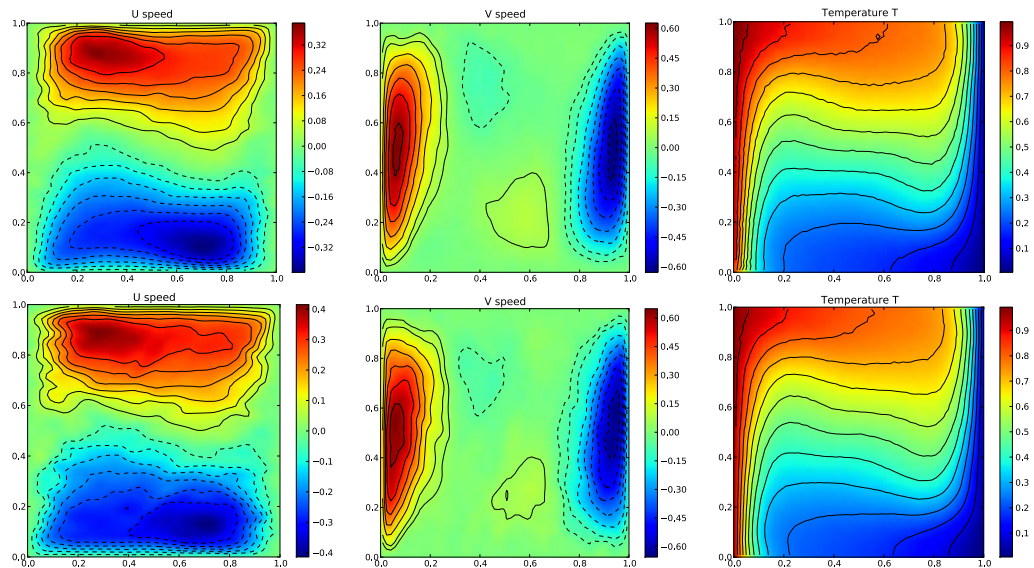


Figure 7.6: Horizontal velocity (left plots), vertical velocity (middle plots) and temperature field (right plots) for horizontally-heated square cavity at $Ra = 10^5$ and $Pr = 0.71$ (steady-state solution). Top plots: SPH with Boussinesq approximation; bottom plots: SPH with the new approach ($Ga = 0.071$).

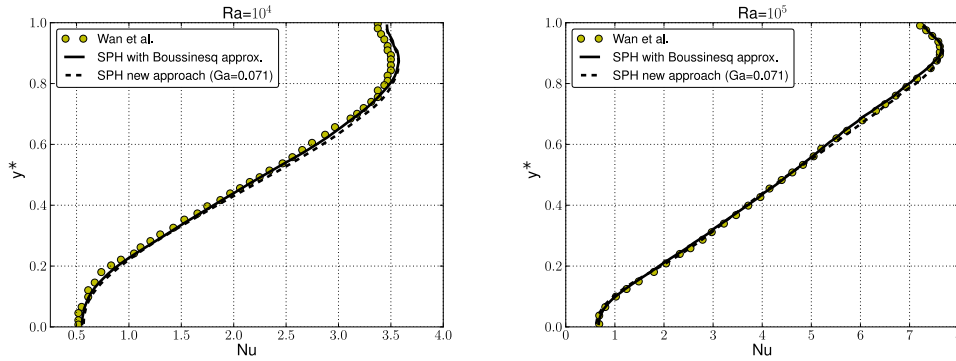


Figure 7.7: The local Nusselt number distribution along the cold wall for: $Ra = 10^4$ (left) and $Ra = 10^5$ (right). Reference data obtained by Wan et al. (2001) using DSC technique.

The local Nusselt number Nu , which describes the ratio of convective to conductive heat transfer across the wall, is defined as

$$Nu(y) = \left. \frac{\partial T^*}{\partial x^*} \right|_{y \in wall}. \quad (7.31)$$

Figure 7.7 shows SPH computations of the local Nusselt number distribution along the cold wall obtained both with the Boussinesq approximation and with the proposed approach. Reference data were computed by Wan et al. (2001) using DCS method. In both SPH variants, the local Nusselt number distributions look very realistic.

For the majority of design problems, the knowledge of the average Nusselt number is more useful. The average Nusselt number is obtained through the integration

$$\overline{Nu} = \frac{1}{L} \int_0^L Nu(y) dy. \quad (7.32)$$

Computed values of \overline{Nu} at different Rayleigh numbers obtained with different methods and spatial resolutions are presented in Table 7.1. Since SPH is Lagrangian method, the particles change their positions during simulation. Therefore, the average Nusselt numbers, computed after obtaining steady-state solution, suffer from the random error $\Delta \overline{Nu}$ from 0.03 for 30x30 particles down to 0.01 for 90x90. However, SPH solutions are in good accordance with data obtained using other methods. For all the cases of Ra , SPH computations of \overline{Nu} value are underrated on the average about 4% to the reference data. The closest to SPH is the solution performed by Wan et al. (2001) using DSC.

Non-Boussinesq regime

However, the most important advantage of the new approach shows up when density varies significantly under the influence of temperature. In this regime, the Boussinesq approximation fails. Such a flow may be described with three dimensionless numbers. As in the regime of the Boussinesq approximation: the Prandtl (Pr), the Rayleigh (Ra), and additionally the Gay-Lussac number (Ga).

Table 7.1: Comparison of the averaged Nusselt numbers (\overline{Nu}) obtained at different Rayleigh numbers for the steady-state solution.

Ra	10^3	10^4	10^5
De Vahl Davis (1983)	1.118	2.243	4.519
Kao and Yang (2007) (LBM)	1.113	2.238	4.508
Wan et al. (2001) (FEM)	1.117	2.254	4.598
Wan et al. (2001) (DSC)	1.073	2.155	4.358
SPH (30x30) with Boussinesq approx.	1.06	2.17	4.42
SPH (60x60) with Boussinesq approx.	1.04	2.16	4.33
SPH (90x90) with Boussinesq approx.	1.04	2.16	4.32
SPH (30x30) with variable density ($Ga = 0.071$)	1.06	2.22	4.55
SPH (60x60) with variable density ($Ga = 0.071$)	1.04	2.18	4.34
SPH (90x90) with variable density ($Ga = 0.071$)	1.04	2.18	4.34

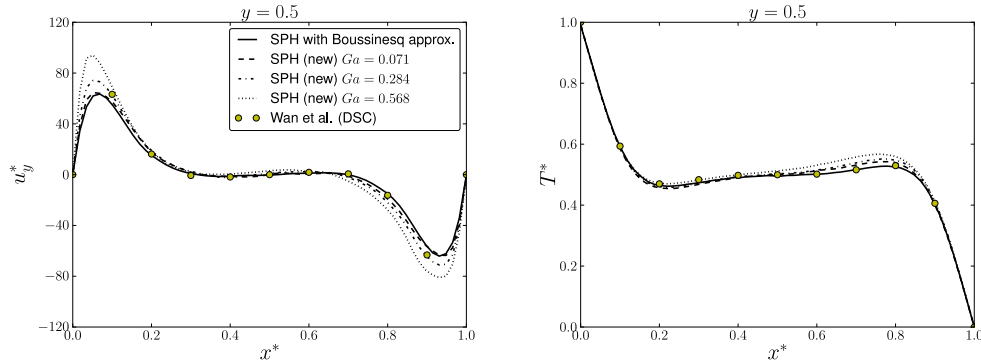


Figure 7.8: The steady-state velocity and temperature profiles obtained at $Ra = 10^5$ from SPH with the standard Boussinesq approximation and with the new approach for $Ga = 0.071$, $Ga = 0.284$ and $Ga = 0.568$. Reference data was obtained by Wan et al. (2001) using DSC technique with the Boussinesq approximation.

We decided to simulate a differentially heated square cavity at $Ra = 10^5$ for selected Gay-Lussac numbers: $Ga = 0.071$, 0.284 , 0.568 , with $Pr = 0.71$. In the initial state the fluid is discretized with 3600 homogeneously distributed particles. Figure 7.8 shows calculated steady-state velocity and temperature profiles. In comparison to the velocity profiles obtained by Wan et al. (2001), both the new approach with $Ga = 0.071$ and the standard Boussinesq formulation behave similarly (small underestimation). As expected, the temperature profiles obtained with the standard Boussinesq approximation (SPH and DSC) are close to each other. For $Ga = 0.284$, 0.568 and 0.852 , qualitatively new phenomena appear. The velocity increases with increasing Ga . It is an expected result, because the growth of the Gay-Lussac number causes higher differences in density that lead to the increase of buoyancy effects.

A very interesting and not widely investigated phenomenon is the influence of the Ga parameter on the local and average Nusselt number. To the best of our knowledge, this problem was considered by Pessoa and Piva (2009) only. Doing such simulations, we decided to investigate two kinds of fluids. In the first, the thermal

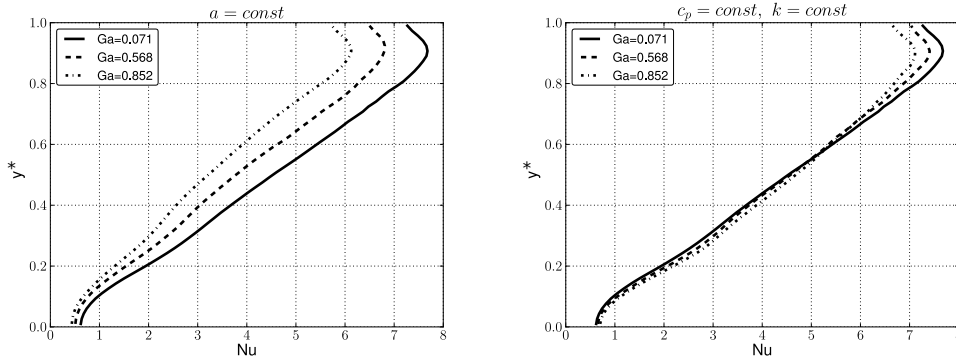


Figure 7.9: The local Nusselt number along the cold wall at $Ra = 10^5$ and varying Gay-Lussac numbers. Data obtained using constant (left) and variable (right) thermal diffusivity coefficient a .

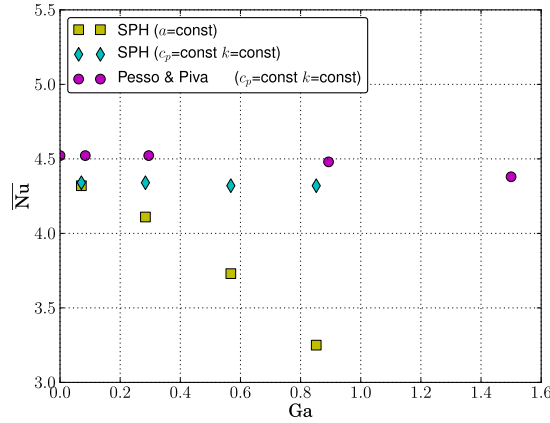


Figure 7.10: The average Nusselt numbers \overline{Nu} as a function of the Gay-Lussac (Ga) number at $Ra = 10^5$ and $Pr = 0.71$ using variable and constant thermal diffusivity coefficient a . Reference data: Pessoa and Piva (2009).

diffusivity coefficient a is constant. In the second, the specific heat capacity c_p and thermal conductivity k do not change, thus $a \sim \rho^{-1}$. Obtained results for the local Nusselt number are presented in Fig. 7.9. In the case of constant a , the increase of Ga causes the local Nusselt number to decrease. In the case of constant c_p and k , the local Nusselt number variation is caused by two factors: a faster convection and a growths of thermal diffusivity coefficient. Since the mean value of a in the domain increases with Ga , heat is transferred faster, causing the local Nusselt Nu to grow. This effect compensates for the influence of convection.

Figure 7.10 shows the average Nusselt number as a function of Ga obtained for steady-state solution. Presented SPH results are compared to those obtained by Pessoa and Piva (2009) for the heat diffusivity a depending on ρ . In both methods the increase of Ga insignificantly decreases the average Nusselt number. This tendency is in agreement with the scale analysis performed by Pessoa and Piva (2009). How-

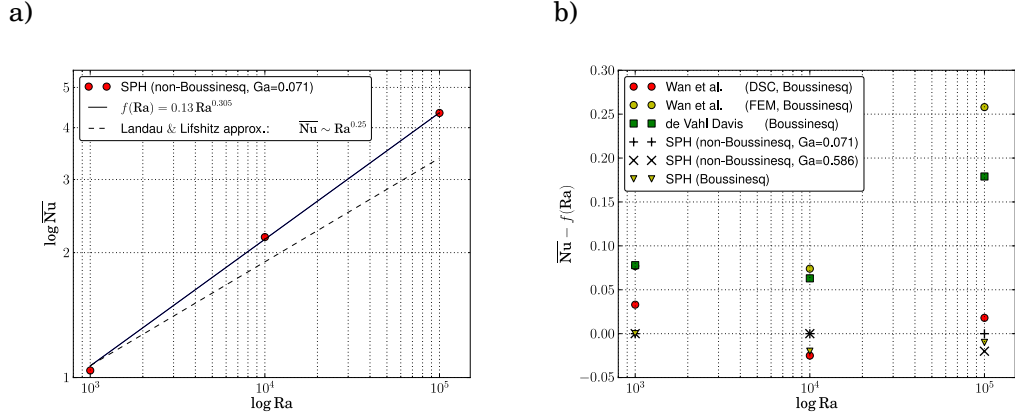


Figure 7.11: Differentially heated cavity: (a) the averaged Nusselt (\overline{Nu}) obtained with the new approach ($Ga = 0.071$) as a function of the Rayleigh number with adjusted correlation $f(Ra)$, (b) distinction between $f(Ra)$ and other results.

ever, the SPH computations obtained with a constant a show a considerably different behavior: the growth of Ga drastically decreases the average Nusselt number.

Figure 7.11(a) presents the average Nusselt numbers as a function of the Rayleigh number. The solid line represents the power-law correlation $\overline{Nu} = f(Ra)$ adjusted to these data. Figure 7.11(b) shows distinction between $f(Ra)$ and solutions obtained using various methods, including both standard and new SPH formulations. It is instructive to compare our results with the correlation for the average Nusselt number in the simpler case of free convection on a flat vertical wall performed by Landau and Lifschitz (1987):

$$\overline{Nu} \sim Ra^{0.25}. \quad (7.33)$$

Since we may treat that system as a simplification of the differentially heated square cavity considered here, the Landau and Lifschitz solution and our correlation

$$\overline{Nu} \sim Ra^{0.305}, \quad (7.34)$$

are indeed similar to each other.

7.4 Conclusions

In Section 7.2 the new SPH form of the energy equation has been introduced and validated with heat transfer process in homogeneous and inhomogeneous slabs. Since the proposed form is based on the Hu and Adams (2006) formalism, and, therefore, constructed on the basis of normalised kernels, it is potentially more accurate than the approaches based on the standard SPH formulae (Cleary, 1998; Cleary and Monaghan, 1999).

In Section 7.3 an extensive discussion about the natural convection phenomena was presented. The use of Boussinesq approximation for modelling natural convection phenomena is wide-known and commonly used, specially by engineers.

However, allowing the density to change considerably due to high temperature gradients, the classical Boussinesq approximation may fail. In such a case, a more general formulation is necessary. In the present chapter, we have proposed the new approach for dealing with the natural convection phenomena more generally, computing flows in the non-Boussinesq regime using Lagrangian SPH method. The important is that the new method is also valid for multiphase flow simulations. To assess this new technique, we first performed simulations in the Boussinesq approximation regime using the standard formulation and the new approach. In this study we computed a series of simulations of natural convection in the horizontally-heated square cavity using both methods. Obtained results were compared to the available data from the literature. All the confronted results show good accordance. The average Nusselt numbers differ up to 4% between different approaches. Since in the non-Boussinesq regime the new dimensionless number Ga is necessary to describe the flow, the influence of this parameter on the velocity field and the Nusselt numbers was investigated. The results agree reasonably well with the reference computations of Pessa and Piva (2009).

Chapter 8

Towards phase-change simulations

8.1 Introduction

A numerical solution of the phase change problem involves the modelling of many coupled elements like the momentum and energy equations, the latent heat and inter-phase mass transfer, the surface tension forces, discontinuities of material properties, and finally the interface shape tracking. In the case of Eulerian CFD approaches, some of the above are treated with no major difficulty, yet some others are a little bit tricky. The examples are the computation of the position of the interface in Volume-Of-Fluid (Hirt and Nichols, 1981), Marker-And-Cell (Harlow and Welch, 1957; McKee et al., 2008), Front-Tracking (Tryggvason et al., 2001; Unverdi and Tryggvason, 1992) and the Level-Set (Sussman et al., 1994) approaches or, in general, the one-fluid approximation. However, it does not change the fact that these methods have proven to be efficient and sufficiently accurate for many cases of phase change phenomena (Jeon et al., 2009; Juric and Tryggvason, 1996, 1998; Kunkelmann and Stephan, 2010; Tryggvason et al., 2005).

Due to the Lagrangian formalism of Smoothed Particles Hydrodynamics, the problems with taking into account the discontinuity of material properties or with the interface handling are potentially less troublesome in this approach. However, this does not mean that SPH is an obvious choice for computing phase change phenomena.

The first implementations of phase change in SPH were proposed by Monaghan et al. (2005) to simulate the solidification of one- and two-component systems, cf. Sect. 8.2. Later, Cleary and Ha (2002), Cleary et al. (2006), and Cleary (2010) obtained very accurate simulations of casting processes including shrinkage of cooling metal, tracking of oxide formation, prediction of feeding, solidification front dynamics and prediction of the residual pressure distribution of solidified metal.

Unfortunately, complications appear when the liquid-vapour phase change is considered. Analysing the process of boiling macroscopically, when the temperature of the liquid near the interface is equal to (or higher than) the saturation temperature T_{sat} , phase change and, consequently, inter-phase mass transfer occurs. The main problem is the huge difference of densities between the liquid and gaseous

phases. However, the problem is not only a numerical one; even from the physical point of view there remain still unresolved issues such as the proper boundary condition for temperature at the interface (Juric and Tryggvason, 1998) or the liquid-bubble heat transfer mechanisms (Kim, 2009). So, apart from fluid-dynamical issues, also the non-equilibrium thermodynamics becomes involved in the picture.

The first SPH simulations of evaporation, taking into account only the van der Waals model of fluid based on the model developed by Tartakovsky and Meakin (2005) were performed by Charles and Daivis (2009). However, that application was limited only to mesoscopic scale flows.

In addition to a brief introduction to simulations of solidification using the SPH approach, our first ideas and sketches for implementation of the liquid-vapour phase change in the macroscopic scale are presented. They are subject to further discussions and subsequent modifications.

8.2 Freezing

Simulations of the solidification phenomena ('freezing') are of importance for many industrial and environmental problems. Examples include the die casting processes or the formation of ice on rivers. From the numerical point of view, due to rather small density changes, this is the simplest case of the phase change phenomena.

The simplest implementation of the solidification model in the SPH approach was proposed by Monaghan et al. (2005) to simulate the freezing of one- and two-component (water + salt) systems. Since Monaghan considered only cases without fluid motion, the model consists of heat conduction equation in form (7.5) and liquid-solid integer tagging system (colour function) to distinguish between particles representing different phases. If, due to heat conduction, a given particle reaches the temperature of solidification T_s , heat is stored until the latent heat L is extracted. When the latent heat is fully extracted, then a particle becomes a particle of the other phase.

Another SPH simulations of solidification were done by Cleary and Ha (2002), Cleary et al. (2006), and Cleary (2010) who proposed the WCSPH approach to model the processes of casting. Their dynamical (involving fluid motion) model was composed of the Navier-Stokes equation

$$\frac{d\mathbf{u}_a}{dt} = - \sum_b m_b \left[\left(\frac{p_a}{\rho_a^2} + \frac{p_b}{\rho_b^2} \right) - \frac{4}{\rho_a \rho_b} \frac{\mu_a \mu_b}{\mu_a + \mu_b} \frac{\mathbf{u}_{ab} \cdot \mathbf{r}_{ab}}{\mathbf{r}_{ab}^2 + \eta^2} \right] \nabla_a W_{ab}(h), \quad (8.1)$$

the continuity equation

$$\frac{d\rho_a}{dt} = \sum_b m_b \mathbf{u}_{ab} \cdot \nabla_a W_{ab}(h), \quad (8.2)$$

and the energy equation, written in terms of enthalpy (which is generally preferred for flows with phase changes)

$$\frac{dH_a}{dt} = \sum_b \frac{4m_b}{\rho_a \rho_b} \frac{k_a k_b}{k_a + k_b} \frac{T_{ab} \mathbf{r}_{ab}}{\mathbf{r}_{ab}^2 + \eta^2} \cdot \nabla_a W_{ab}(h). \quad (8.3)$$

The enthalpy per unit mass H is defined as

$$H = \int_0^T c_p(\Theta) d\Theta + L[1 - f_s(T)], \quad (8.4)$$

where L is the latent heat, and $f_s(T)$ is the local volume fraction of solid at temperature T . To model solidification/melting, Cleary et al. considered two different approaches. The first one involves a viscosity dependency with temperature. In this approach the solid phase is represented as a viscous pseudo-fluid. However, this does not allow to preserve stresses in the solidified metal. In the second approach (stress-preserving), when the temperature of a fluid particle is lower than the solidus temperature and this particle has more than two neighbours (under the kernel hat) representing the solid phase, then the N-S equation changes to another equation more suitable for solids (e.g., stopping a particle and freezing it in occupied place).

8.3 Boiling

The ability of fluids to store and then transfer large amount of energy in the form of the latent heat when boiling or condensation occurs is the key property exploited for energy management in many industrial applications. Among other processes and devices, the liquid-vapour phase change is crucial for heat exchangers in fossil power plants or in the primary circuits of nuclear reactors where huge amount of energy have to be extracted from the core as efficiently as possible. In the following, we will focus on boiling; yet, the modelling and numerical difficulties involved with condensation are similar.

When phase change occurs in a liquid coolant (nucleate boiling), energy is stored in the form of latent heat. Moreover, bubble formation may induce a considerable local velocity of the liquid layer on the heated surface. Both factors imply a substantial increase of heat transfer. Generally, an increase of the wall temperature leads to higher heat transfer. However, the practical use of boiling is limited by the condition called the critical heat flux or boiling crisis. It occurs when the boiling regime changes, with the increase of wall heat flux, from the sub-cooled (nucleate) boiling, through the so-called departure from nucleate boiling (DNB), the film boiling, up to the extreme situations when the evolution of vapour prevents the liquid from approaching the surface and the heat transfer suddenly decreases. Further increase of the wall heat flux produces a continuous layer of vapour at the heating wall so the surface is isolated from the liquid. Then, all the heat transfer occurs only due to the radiation and convection in gaseous phase. The prevention from DNB and, in consequence, from the overheating (burnout) of the heating surface is one of the most important issues in many engineering problems where heat production and conversion are crucial.

As mentioned in the Introduction, the main problem in the implementation of boiling in the SPH approach is the huge density difference between the phases and, therefore, the procedure of recolouring particles, used in simulations of solidification, can not be explicitly extended to reproduce the inter-phase mass transport in boiling. Moreover, since in the SPH particles represent volume elements of the fluids, the splitting and merging of particles procedure seems to be unrealistic (or a

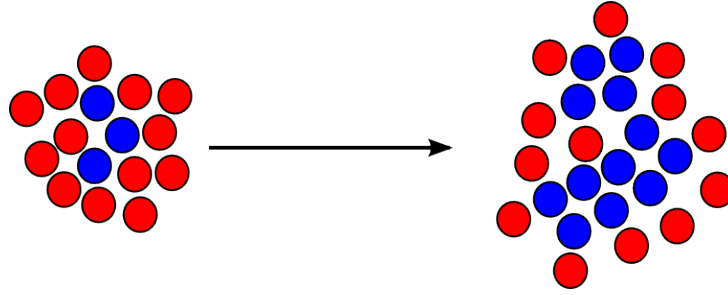


Figure 8.1: Scheme of phase-change model based on pushing new particles into the gaseous phase.

very complex issue). This is due to the fact that one particle of liquid should represent one thousand particles of vapour, say, while solutions based on fractional particles do not come into play.

8.3.1 Particle pushing model

The huge difference between the densities of phases suggests another, simple solution. After nucleation, vapour bubbles change their size due to the inter-phase mass flow. When a bubble grows, if we require a constant resolution, the number of SPH particles representing the gaseous phase should increase.

Yet, due to the density difference, the change of the liquid volume can be considered as negligible. It should be added here that at this stage we consider only nucleation boiling, without strong evaporation of the liquid. For such a case, this assumption is very close to reality. Since we treat the liquid as an infinite reservoir of the gaseous phase, to simulate the appearance of new elements of gaseous phase, we only put these new particles near the interface, cf. Sect. 8.1.

In cases when the liquid phase can no longer be treated as an infinite reservoir of vapour, an imaginable solution may be the addition of new vapour particles (all of the same mass for simplicity) at time steps when the locally accumulated latent heat will trigger the generation of one such particle, at the cost of a (minor) part of the liquid particle mass next to the interface. The mass of all vapour particles is predetermined to respect the assumed spatial resolution of the growing bubbles.

The first problem is the question of the location of these new particles. The simplest solution seems to be to find the location of the interface and create them there. However, in the SPH approach the interface position is not known explicitly. Using the kernel function with the smoothing length of order h , only what we know is the smoothed position of the interface, i.e., calculating the normal vectors to the interface (necessary to determine the surface tension) we find numerical representation of the surface Dirac delta function which does not vanish at particles placed away from the interface. The procedure of searching peaks of normal vectors to the interface, or regions, where a colour function has a specific value after smoothing, can be proposed using the SPH approach; however, because of the need to find values at points located between particles, this method is highly inefficient.

The second problem is the computation of the mass transfer rate $\dot{m} = \dot{q}/L$ where \dot{q} denotes the inter-phase heat transfer rate, and L is the enthalpy of vaporisation,

at the point where new particles will be placed. The useful solution, used in many Eulerian implementations of boiling (Jeon et al., 2009; Kunkelmann and Stephan, 2010) is (assuming that the heat conductivity on the interface is equal to heat conductivity in liquid)

$$\dot{m} = \frac{k(T_{\text{sat}} - T)S}{L\phi}, \quad (8.5)$$

where T_{sat} is the temperature of saturation, ϕ is the mean distance to the interface

$$\phi = \sum_{b, \text{ if } c_b \neq c_a} \frac{m_b}{\rho_b} |\mathbf{r}_b| W_{ab}(h), \quad (8.6)$$

while S is the area of the liquid-vapour interface which represents the particle.

To construct the procedure of computing the area (or length in 2D) of the interface, let us use the definition of the surface delta function

$$S = \int_{\Omega} \delta_s(\mathbf{r}) d\mathbf{r}. \quad (8.7)$$

As already mentioned in Sect. 5.3, the surface delta distribution δ_s can be expressed in many ways. Here, it is employed as previously

$$\delta_s = |\mathbf{n}|, \quad (8.8)$$

where the normal vector \mathbf{n} is obtained as in the computing of the surface tension force. Discretising Eq. (8.7), we may write

$$S = \sum_a \delta_s(\mathbf{r}_a) \Omega_a = \sum_a \frac{m_a}{\rho_a} |\mathbf{n}_a|. \quad (8.9)$$

To verify the correctness of the interface area computation, a two-dimensional case involving a circular area of one fluid of the radius $R = 0.25L$ in a square box of size $L = 1.0$ containing another fluid was considered. The computations of the interface length (2D) were performed and compared for three different kernels, described in Sect. 2.1, and two different procedures of finding the normal vectors (cf. Sect. 5.2). Figure 8.2 presents the convergence of the SPH solutions with the number of particles N using the procedure of normal vector computation with (right) and without (left) colour function smoothing procedure of Morris (2000). All simulations were performed with $h/\Delta r = 2$. All the presented results of the interface length computations are normalised by the box size L . Comparing these results it is worth noting that independently of the number of particles N in the domain, the chosen kernel and selected procedure of computing normal vectors, all results agree very well with the analytical solution (less than 1% of discrepancy). However, the least accurate solutions were obtained with the Wendland (1995), which seems to be the best choice taking into account the conclusions of Chapter 3. The main reason of this discrepancy of Wendland kernel is the overestimation of the mean density (described in Sect. 3.5). To (partially) remove this deficiency from the interface surface computation, the normalized form of Eq. (8.9) was proposed

$$S = \frac{\Omega \sum_a \frac{m_a}{\rho_a} |\mathbf{n}_a|}{\sum_a \frac{m_a}{\rho_a}}, \quad (8.10)$$

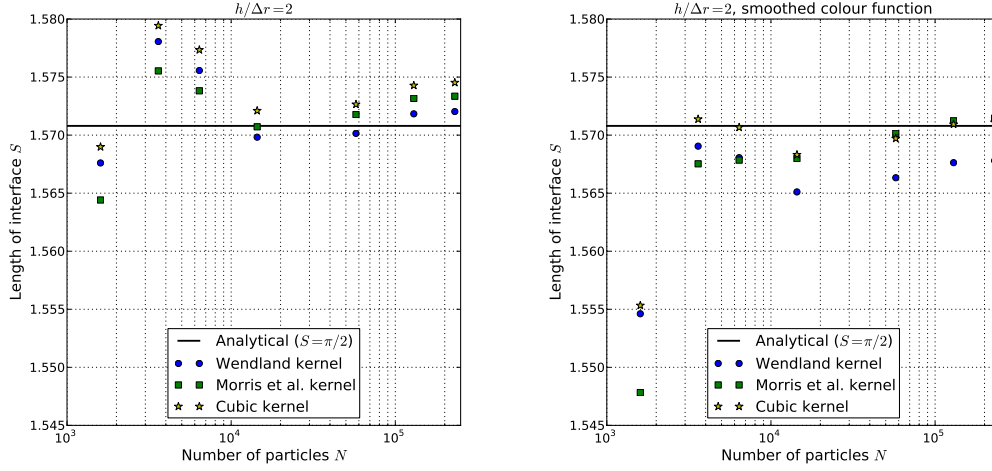


Figure 8.2: The convergence of the SPH computations of total interface length (2D) using the procedure of normal vector computations with (right) and without (left) colour function smoothing of Morris (2000).

where Ω denotes the initial volume (or surface in 2D) of the domain. The solutions are presented in Fig. 8.3. It is easy to note that using formula (8.10) the solutions obtained with the Wendland kernel are much more accurate than previously. Since the normal vector \mathbf{n} and density ρ are computed separately for each particle, taking into account Eq. 8.7, the surface of the interface visible by the particle is

$$S_a = \delta_s(\mathbf{r}_a)\Omega_a = \frac{m_a}{\rho_a}|\mathbf{n}_a|. \quad (8.11)$$

The sum over all particles naturally gives a total surface of the interface, cf. Eq. (8.9).

The last difficulty of particle pushing algorithm, also related to the numerical efficiency, is the need to perform a large number of operations of adding and removing elements representing particles in memory. Such algorithms are very time-consuming and very difficult to write in parallel form.

In order to make a preliminary assessment of the particle pushing model, we decided to analyse a very simple test case of bubble growth caused by pushing new gaseous particles. Fig. 8.4 presents a distribution of the SPH particles in the domain for one gaseous bubble submerged in liquid. The material parameters and initial distributions are as in the case of air bubble rising in water described in Sect. 4.2. But, in this test, the gravity is turned off. The simulations were performed without (left) and with (right) the particle pushing procedure. For each liquid particle placed near the interface, as measured by the smoothed value of colour function ($0.4 < \tilde{c} < 0.6$), if the condition $\dot{q} > m_G L$, where m_G is the mass of vapour particle, then the particle of gaseous phase is put into the position located at distance h from the particle in the direction normal to the interface.

From the results, it is easy to show that some deficiency of particles appears near the interface when particle pushing is switched on. The possible reason is the density disturbance generated when inserting new particles into fluid. These

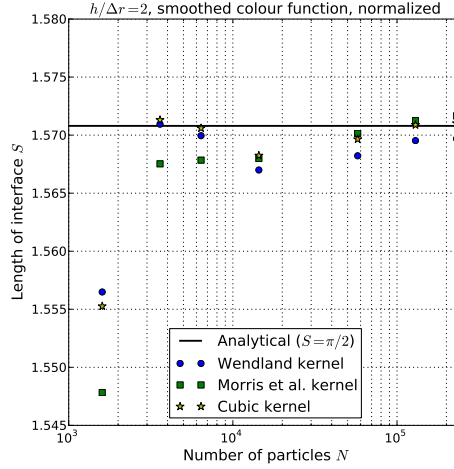


Figure 8.3: The convergence of the SPH computations of total interface length (2D) using the computations of normal vector with colour function smoothing procedure (Morris, 2000) and normalised form of Eq. (8.9).

local jumps of density fields cause the appearance of non-physical waves (weakly compressible approach), in some cases causing the appearance of instabilities.

8.3.2 Variable mass and volume model

Given all the drawbacks of the previous model, we abandoned it in favour of a new approach which does not suffer from a variable number of particles in the domain. The algorithm for this new model is presented in Fig. 8.6. In the first step, the temperature of the fluid and the heat transferred across the interface are determined using the SPH formula (the Colagrossi and Landrini formulation, cf. Sect. 4.1.2)

$$\varrho_a \frac{dU_a}{dt} = \sum_b \frac{4k_a k_b}{k_a + k_b} \frac{T_{ab} \mathbf{r}_{ab}}{r_{ab}^2 + \nu^2} \nabla_a W_{ab}(h) \Omega_b. \quad (8.12)$$

To simplify the problem, the temperature inside the bubble can be treated as uniform and equal to the temperature of saturation for a given gas pressure. The assumption of uniform temperature may be explained by the fact that for nucleate boiling, the thermal diffusion length of the vapour is much larger than the bubble diameter. The evaporation (or condensation) rate is obtained from the heat transferred across the interface calculated using the SPH formulation. Knowing the heat flux at the interface, the mass S^m and density S^ρ source terms can be determined

$$S_a^m = \frac{1}{L} \frac{dQ_a^{int.}}{dt}, \quad (8.13)$$

$$S_a^\rho = \frac{S_a^m}{\Omega_a}, \quad (8.14)$$

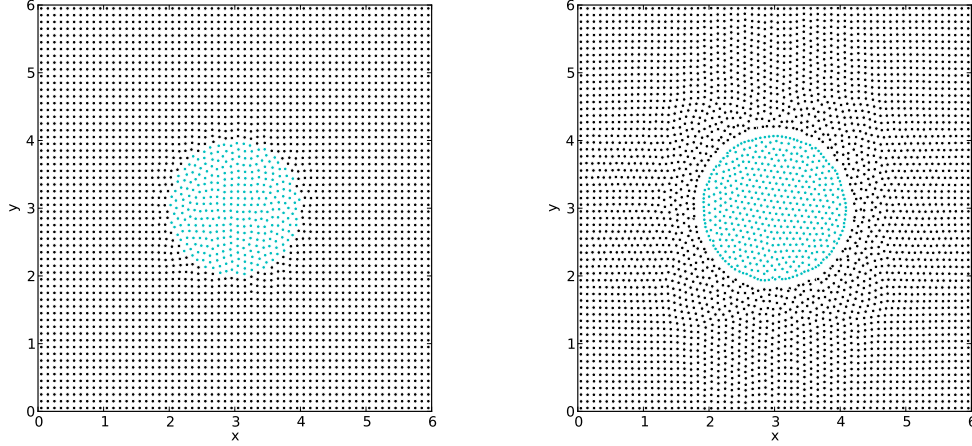


Figure 8.4: Distributions of the SPH particles in domain for the air bubble submerged in water with no gravity force; the simulations performed without (left) and with (right) the particle pushing phenomena.

where L is a latent heat, while $Q_a^{int.}$ is the heat transferred across the interface. In the next step, the density is calculated from the continuity equation

$$\frac{d\rho_a}{dt} = -\rho_a \sum_b \mathbf{u}_{ab} \cdot \nabla W_{ab}(h) \Omega_b + S_\rho, \quad (8.15)$$

while, at the same time, the mass of particles is changing according to

$$\frac{dm_a}{dt} = S_a^m. \quad (8.16)$$

It is important to note that the source terms are suitably chosen to keep the volume of particles Ω not affected. Then, knowing the density of the field, the pressure is calculated from the appropriate equation of state (weakly compressible model for liquid, compressible model for gas/vapour). Due to the changes of density caused by the phase change, the divergence of velocity is non-zero, so, the pressure changes. It causes, in the case of nucleate boiling, an increase of bubble volume. Thus, the volumes of particles Ω also change, cf. Fig. 8.5. Due to this fact, it is necessary to use an SPH formalism that allows to change the resolution of particles in the domain. The problem is almost the same as in the case of simulations of compressible (single phase) flows using the SPH approach. The only difference is the existence of the sharp interface separating the phases of different properties (gas/liquid, compressible/incompressible).

Multi-resolution SPH

The possibility of performing numerical simulations with an SPH formalism that allows for calculation with a variable resolution (spatially different particle number density) is important not only for the model of phase-change proposed here, but, also, to decrease numerical cost in general. In many numerical cases, the use

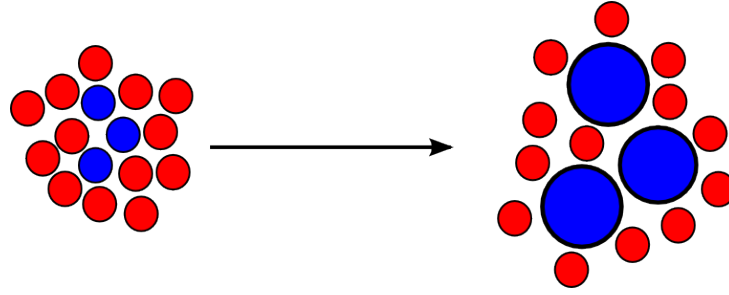


Figure 8.5: Scheme of phase-change model based on changing the mass and volume of particles.

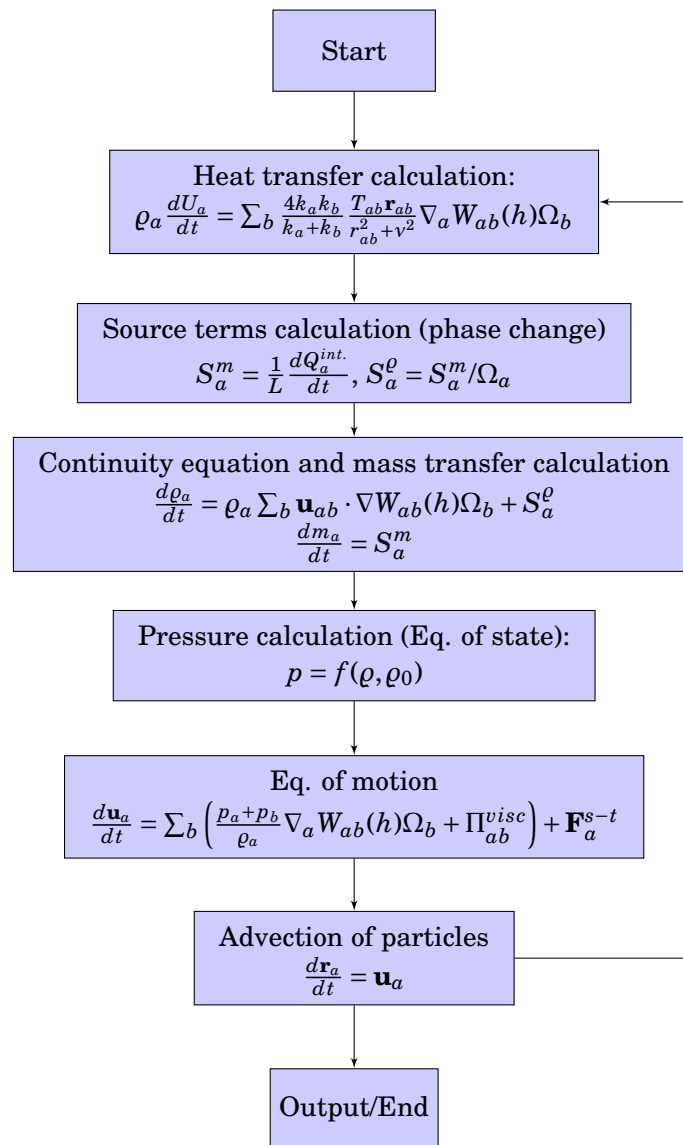


Figure 8.6: Algorithm of the SPH approach with the phase-change model.

of a smaller number of particles in the regions where small resolution is sufficient (reduction of a number of interactions between particles) can significantly speed up the simulation.

Unfortunately, the most useful multiphase flows model (taking into account accuracy and efficiency) proposed by Hu and Adams (2006) is not suitable for this purpose. The reason is that in this approach the density field is represented only by spatial distribution of neighbouring particles

$$\rho_a = m_a \sum_b W_{ab}(h), \quad (8.17)$$

so, there is no influence of the value of volumes Ω which represent particles. Another disadvantage of this approach is a lack of possibility to simulate the free surface flows, which may be important to provide space for increasing the volume system. Due to this fact, we decided to test, in these respects, the Colagrossi and Landrini (2003) formulation. In this approach the density field is evaluated using the continuity equation (and not the density definition).

To validate the usefulness of this approach for multi-resolution issues, firstly, the single phase lid-driven cavity case was considered. It involves a fluid inside a square ($L \times L$) box where only upper boundary moves with the constant velocity \mathbf{u}_w . In this work, we computed this case at $Re = 100$. The domain was initially divided in half into two sections with the resolution of 6400 and 3600 particles per domain. For both sections we decided to use the same kernel size that corresponds to $h/\Delta r = 1.8$ for lower resolution and $h/\Delta r = 2.4$ for higher resolution parts. The reference SPH simulations were performed with the uniform resolution of 6400 particles in domain ($h/\Delta r = 2$).

Figure 8.7 shows the evolution of particle distribution using different sizes (multi-resolution) of SPH particles in the domain. The comparison of the steady-state velocity profiles computed with uniform and multi-resolution distribution of particles is presented in Fig. 8.8. The results are compared to those from a numerical calculation on a fine grid performed with the Eulerian solver by Ghia et al. (1982). It shows that the use of multi-resolution SPH for the single phase flows does not introduce any numerical artifacts which can affect the results.

To validate the multi-resolution SPH for multiphase flows, it was decided to simulate the square-droplet deformation test case. The initial geometry of the system is as in the case of the square-droplet deformation presented in Sect. 5.5.1 (2D). The gas-liquid density and viscosity ratio between inner (*in*) and outer (*out*) phases are respectively $\rho_{out}/\rho_{in} = 10$ and $\nu_{out}/\nu_{in} = 10$. In this case $Ca^2/We = v_{out}^2 \rho_{out}/a\sigma = 2/30$, while the capillary number, $Ca = \rho_{out} v_{out} u/\sigma$, based on the maximal velocity in the domain is about 0.07. The resolution of the outer phase is 3600 particles per domain, while the resolution of the inner phase is 10000 particles per domain. Similarly to the previous case we decided to use the same kernel size that corresponds to $h/\Delta r = 1.8$ for the outer phase and $h/\Delta r = 3$ for the inner phase. The reference SPH simulations were performed with the uniform resolution of 3600 particles in domain ($h/\Delta r = 1.8$). To model the surface-tension phenomena, the CSF method was used. The initial and the steady-state particle distributions are presented in Fig. 8.9. From the Laplace law, the pressure within the formed droplet must be higher than in the surrounding fluid and should change across the interface, satis-

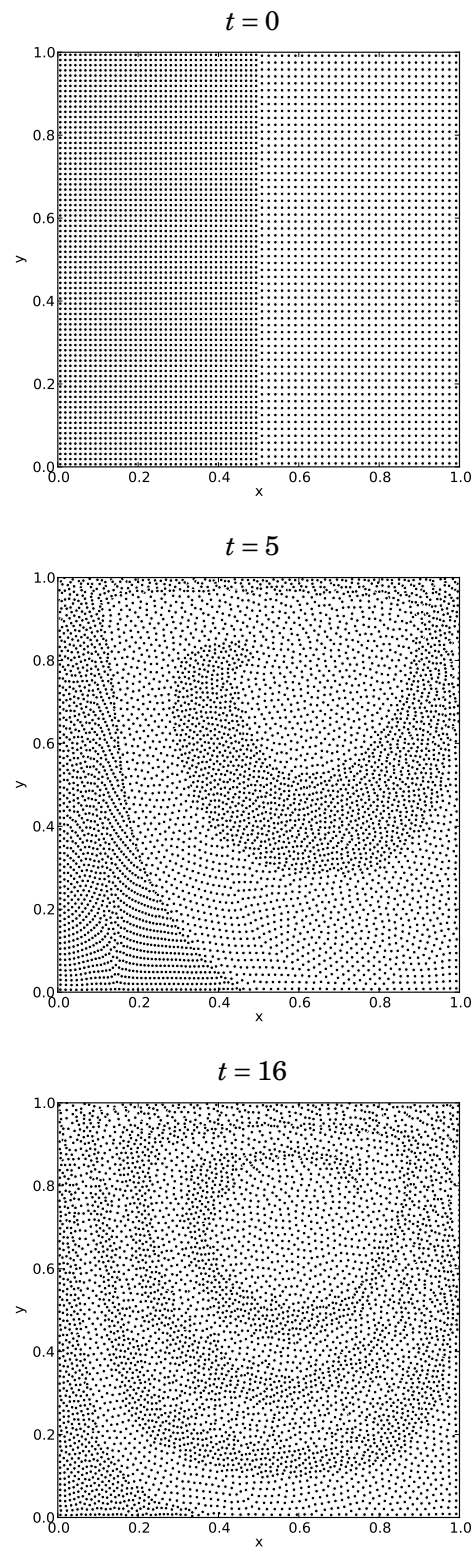


Figure 8.7: Evolution of particle distribution for the lid-driven cavity test (two-dimensional) at $Re = 100$ using different sizes of SPH particles in the domain; time is normalised with the convective time scale $L/|\mathbf{u}_w|$.

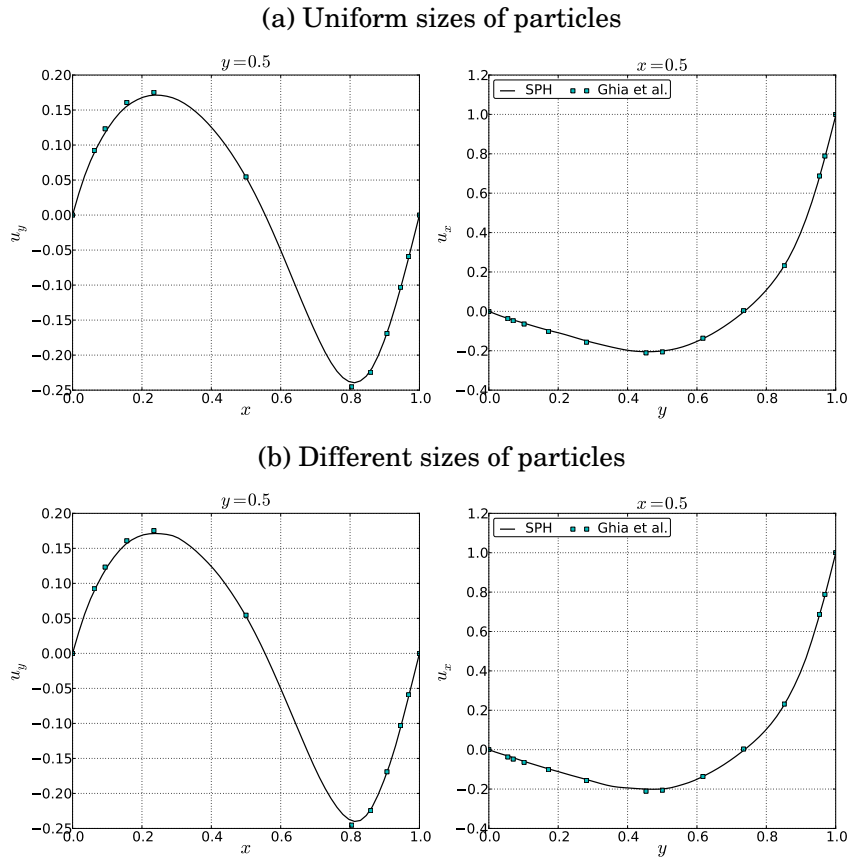


Figure 8.8: The lid-driven cavity (two-dimensional) steady-state velocity profiles at $Re = 100$ computed using WCSPH with uniform (a) and different (b) sizes of particles in a domain, against Ghia et al. (1982).

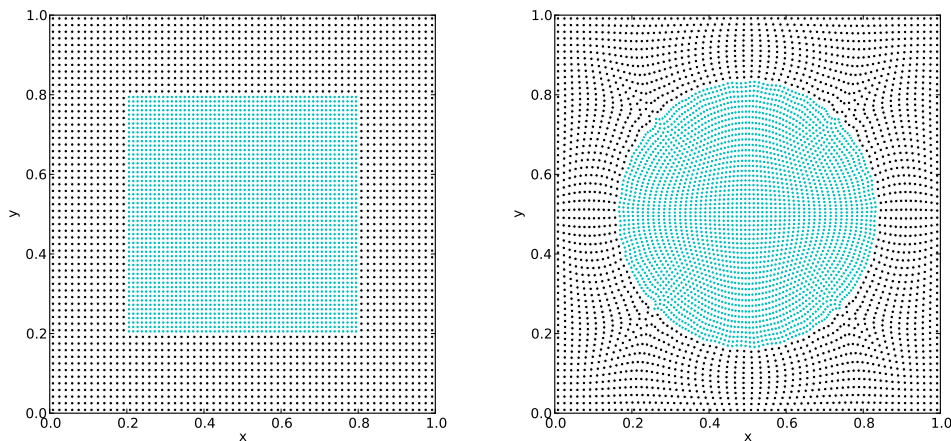


Figure 8.9: Particle distribution of the square-droplet deformation test with multi-resolution: (left) the initial state, (right) the steady-state solution.

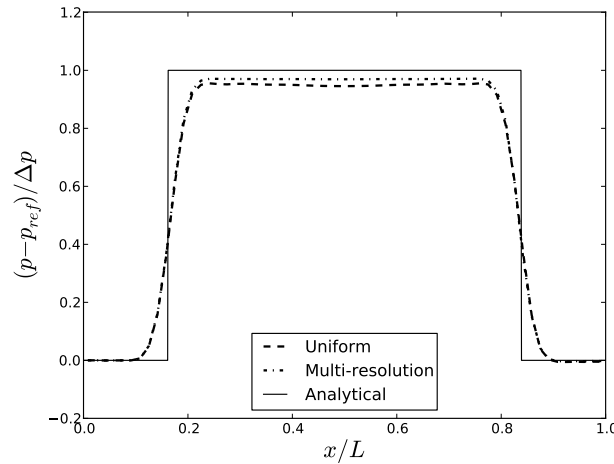


Figure 8.10: Pressure profiles in the steady-state solution of square-droplet deformation obtained using the uniform- and multi-resolution SPH. Results are compared to the analytical solution.

ifying the condition

$$\Delta p = \frac{\sigma\sqrt{\pi}}{a}. \quad (8.18)$$

Resulting analytical and numerical pressure profiles are presented in Fig. 8.10. The obtained result can be also compared to the SPH simulations obtained using the uniform initial distribution. In this case, as in the case of single-phase lid-driven cavity flow, the use of multi-resolution does not introduce any numerical artifacts which affect the result. Moreover, the use of higher resolution only inside the considered droplet may allow to obtain a higher accordance with the analytical result, cf. Fig. 8.10.

However, it is important to note, that due to the accuracy (sufficiently high number of particles under kernel hat) and efficiency (sufficiently low number of particles under kernel hat) reasons, in the cases where the ratio between particle volumes of different phases in the domain is very high, it is important to use variable kernel smoothing length h . This new approach of phase change implies a new problem that needs to be solved. Furthermore, the increase (or decrease) of volume of the SPH particles (even using the variable kernel smoothing range) causes the change of the spatial resolution. However, as it was earlier mentioned, the splitting and merging of particles procedure seems to be unrealistic (or a very complex issue).

8.4 Conclusions

From both numerical and physical point of view, modelling of phase change phenomena is a very complex problem. It involves a long list of coupled elements which have to be properly simulated. However, since the Smoothed Particle Hydrodynamics method is a fully Lagrangian approach, the problems with taking into account

the discontinuity of material properties or with the interface handling are potentially less troublesome than in the Eulerian methods.

In the case of solidification/melting processes, where the density ratio between phases is not very high, the SPH method seems to be very useful. But, in the case of boiling (evaporation/condensation) phenomena, situation is very different.

The main problem in the Eulerian simulations of the boiling phenomena is not the transfer of mass through the interface (even rapid), but, rather a precise handling of the interface position. In the SPH method, the situation is opposite. There is no necessity to calculate the position of the interface during a simulation, but, due to the Lagrangian nature of method (the fact that not a space, but liquid is discretised), the mass transfer through the interface is not an easy task.

In this chapter the problems associated with the SPH implementation of boiling were presented and two different approaches to solve the problem of mass transfer were discussed. The first one is based on adding new vapour particles at time steps when the locally accumulated latent heat will trigger the generation of one such particle. However, in this method new problems appear: the question of the location of these new particles, the computation of the mass transfer rate at new particle positions and problems with efficiency of reallocation (extension of) data arrays in memory. The second proposition is to change the volume and mass of elements of fluid (particles) during phase change. However, this method implies the necessity to use the SPH formalism which allows to change the volume and mass of particles, what can be done using, eg., the Colagrossi and Landrini (2003) formalism. However, the increase (or decrease) of the volume of the SPH particles (even using the variable kernel smoothing range) causes the change of the spatial resolution. Since the procedure of splitting/merging particles, due to the complexity, does not seem to be a viable option, the only possibility is to accept this deficiency or perform a remeshing procedure (re-distribution of SPH particles in the domain), resulting in return to the Eulerian point of view with all its drawbacks.

In the opinion of the author, the presented in this chapter methods of extending the SPH method by the ability to simulate boiling processes, despite many difficulties, have potential to successfully perform this task. However, except these ideas, there are three more possibilities which are also worth considering. The first is, as it was mentioned earlier, the use a remeshing procedure, so that mass transfer could be simulated using the Eulerian formalism, while advection could be simulated using SPH. The second possibility is to follow the idea of Charles and Daivis (2009), which involves only the van der Waals model of fluid, so that the engineering application is limited to the mesoscopic scale flows only. The third idea is to develop multi-scale SPH approach able to simulate flow at hydrodynamic level in the whole domain except the regions placed close to the interface where the van der Waals model of fluid could be applied.

Chapter 9

Perspectives

Due to the fact that SPH is a fully Lagrangian technique and there is no necessity to handle the interface position as it is obligatory in Eulerian methods, during the last ten years, the SPH approach has been greatly developed to deal with free-surface and multiphase flows. However, as it was shown in this work, there are still many unsolved problems. An interesting issue is the micro-mixing of the SPH particles at the interface. This numerical artifact may highly affect the accuracy of results. The main reason of this phenomenon is a lack of mechanism assuring immiscibility of phases in SPH. In this work all the remedies which are available in the literature were discussed and a new variant of sharpness correction procedure was proposed and validated. However, despite the significant improvement in accuracy observed using the sharpness correction procedures, it is clear that further studies to resolve this problem are necessary. In the opinion of the author, a promising idea of preventing the appearance of the non-physical interface fragmentation is the use of hybrid approaches combining the SPH method with Level Set or Front Tracking.

A significant part of this work was devoted to the problem of modelling bubbles rising through liquids, including bubble-bubble interactions. The simulations of such phenomena are very important for many industrial applications. In the present work only the simple case of bubble-bubble coalescence has been considered. But, generally, depending on the Weber number, bubbles can both: coalesce or bounce, cf. Duineveld (1998). What is more, after bouncing bubbles can both coalesce and separate without coalescing. Therefore, a natural next step is to assess and check if the SPH method is able to predict all these regimes. On the other hand, in most of industrial applications, bubbles do not rise separately or in pairs, but, rather in very dense swarms. Therefore, a question arises about the usefulness of the SPH method for simulations of the cases involving large numbers of interacting bubbles. Weighting between the accuracy and the computational time, maybe, for such industrial applications, it is more convenient to use rather statistical approaches, and not SPH. However, for sure, the SPH method has potential to accurately simulate the processes involving the motion of bubbles induced by the Marangoni effect and the surface-agents dynamics. The first attempts to model this issue have been taken by Adami et al. (2010) who proposed the SPH formula for the surfactant (scalar function) transport equations. These authors showed the usefulness of their model to simulations of an oscillating bubble and deformation

of bubble in shear flow. It could be relevant to extend the SPH by the ability of simulate bubbles rising in water taking into account the influence of surfactants. When surfactants are added to water, above a critical concentration, bubbles start to behave like rigid particles - the drag coefficient is similar to that of solid sphere (stopping internal recirculation), cf. Duineveld (1998). What is more, above the critical concentration, the interacting bubbles are prevented from coalescing.

Another challenging task that is definitely worth undertaking is an attempt to extend the SPH method by the ability of modelling the liquid-gas phase transitions. Some of the first ideas were presented in this work. All these concepts were based on the macro-scale description of the phase change phenomena, which not only causes a lot of numerical problems, but also necessitates the use of coarse models of physics, what significantly limits their potential application. However, besides the presented concepts some other ideas can be also proposed. One of the most promising ideas is to go down to the meso-scale level using the van der Waals equation of state (Charles and Daivis, 2009). Using this concept, the processes of phase change would be modelled much more accurately at the cost of numerical efficiency. However, the computation time could be reduced through the use of multi-scale approach. Using such a technique, the flow in the whole domain could be simulated using classical SPH at the hydrodynamic level. Only the regions placed close to the liquid-vapour interface could be modelled using the meso-scale approach with the van der Waals equation of state. What is more, in the cases where the meso-scale description is too rough, even Molecular Dynamics simulations could be done. Additional advantage of using the multi-scale ideas is an explicit computation of surface tension force. The ability to accurately simulate this phenomenon using the van der Waals equation of state was proven by Tartakovsky et al. (2009). Yet another advantage is lack of troubles with the micro-mixing phenomena at the hydrodynamic level. In the procedure of projection of field onto the coarse grid (SPH particles representing macro-scale elements of fluid) the micro-mixing phenomena could be naturally removed (smoothed).

Bibliography

- Adami, S., Hu, X.Y., Adams, N.A., 2010. A conservative SPH method for surfactant dynamics, *J. Comput. Phys.* **229**, 1909-1926.
- Aidun, C.K., Clausen, J.R., 2010. Lattice-Boltzmann Method for complex flows, *Annu. Rev. Fluid Mech.* **42**, 439-472.
- Amaya-Bower, L., Lee, T., 2010. Single bubble rising dynamics for moderate Reynolds number using Lattice Boltzmann Method, *Comput. Fluids* **39**, 1191-1207.
- Andrews, M.J., O'Rourke, P.J., 1996. The Multiphase Particle-In-Cell (MP-PIC) method for dense particle flows, *Int. J. Multiphase Flow* **22**, 379-402.
- Batchelor, G.K., 1967. *An Introduction to Fluid Dynamics*, Cambridge University Press.
- Becker, R., Braack, M., 2002. Solution of a stationary benchmark problem for natural convection with large temperature difference, *Int. J. Therm. Sci.* **41**, 428-439.
- Belytschko, T., Krongauz, Y., Dolbow, J., Gerlach, C., 1998. On the completeness of meshfree particle methods, *Int. J. Numer. Mech. Eng.* **43**, 785-819.
- Benz, W., Asphaug, E., 1993. Explicit 3D continuum fracture modeling with Smoothed Particle Hydrodynamics, *Proceedings of Twenty-fourth Lunar and Planetary Science Conference*, 99-100.
- Benz, W., Asphaug, E., 1995. Simulations of brittle solids using Smoothed Particle Hydrodynamics, *Comput. Phys. Commun.* **87**, 253-265.
- Berczik, P., 2000. Modeling the star formation in galaxies using the chemodynamical SPH code, *Astron. Astrophys.* **360**, 76-84.
- Bhaga, D., Weber M.E., 1981. Bubbles in viscous liquids: shapes, wakes and velocities, *J. Fluid Mech.* **105**, 61-85.
- Bonet, J., Lok, T.-S. L., 1999. Variational and momentum preservation aspects of SPH formulations, *Comput. Methods Appl. Mech. Eng.* **180**, 97-115.
- Bonometti, T., Magnaudet, J., 2006. Transition from spherical cap to toroidal bubbles, *Phys. Fluids* **33**, 52-102.

- Brackbill, J.U., Kothe, D.B., Zemach, C., 1992. A continuum method for modelling surface tension, *J. Comput. Phys.* **100**, 335-354.
- Brennen, C.E., 2005. *Fundamentals of Multiphase Flow*. Cambridge Univ. Press, Cambridge.
- Bürzle, F., Clark, P.C., Stasyszyn, F., Greif, T., Dolag, K., Klessen, R.S., Nielaba, P., 2010. *Mon. Not. R. Astron. Soc.* **412**, 171-186.
- Campbell, P.M., 1989. Some new algorithms for boundary value problems in smoothed particle hydrodynamics, Technical Report NA-TR-88-296, Mission Research Corporation, Albuquerque.
- Carslaw, H.S., Jaeger, J.C., 1965. *Conduction of Heat in Solids*, Oxford Univ. Press, London.
- Chaniotis, A.K., Poulikakos, D., Koumoutsakos, P., 2002. Remeshed smoothed particle hydrodynamics for the simulation of viscous and heat conducting flows, *J. Comput. Phys.* **182**, 67-90.
- Chaniotis, A.K., Frouzakis, C.E., Lee, J.C., Tomboulides, A.G., Poulikakos, D., Boulouchos, K., 2003. Remeshed smoothed particle hydrodynamics for the simulation of laminar chemically reactive flows, *J. Comput. Phys.* **191**, 1-17.
- Charles, A., Daivis, P., 2009. Smooth Particle Hydrodynamics for Vapour Liquid Coexistence, 18th World IMACS-MODSIM Congress, Cairns, Australia 2009.
- Cheng, M., Hua, J., Lou, J., 2010. Simulations of bubble-bubble interaction using a lattice Boltzmann method, *Comput. Fluids* **39**, 260-270.
- Chui, Y.-P., Heng, P.-A., 2010. A meshless rheological model of blood-vessel interaction in endovascular simulation, *Prog. Biophys. Mol. Bio.* **103**, 252-261.
- Cleary, P.W., 1998. Modelling confined multi-material heat and mass flows using SPH, *Appl. Math. Model.* **22**, 981-993.
- Cleary, P.W., 2010. Extension of SPH to predict feeding, freezing and defect creation in low pressure die casting, *Appl. Math. Model.* **34**, 3189-3201.
- Cleary, P.W., Ha, J., 2002. Three-dimensional smoothed particle hydrodynamics simulation of high pressure die casting of light metal components, *J. Light Met.* **2**, 169-183.
- Cleary, P.W., Monaghan, J.J., 1999. Conduction modelling using smoothed particle hydrodynamics, *J. Comput. Phys.* **148**, 227-264.
- Cleary, P.W., Ha, J., Prakash, M., Nguyen, T., 2006. 3D SPH flow predictions and validation for high pressure die casting of automotive components, *Appl. Math. Model.* **30**, 1406-1427.
- Colagrossi, A., Antuono, M., Le Touzé, D., 2009. Theoretical considerations on the free-surface role in the smoothed-particle-hydrodynamics model, *Phys. Rev. E* **79**, 056701.

- Colagrossi, A., Landrini, M., 2003. Numerical simulation of interfacial flows by smoothed particle hydrodynamics, *J. Comput. Phys.* **191**, 227-264.
- Cottet, G.H., Koumoutsakos, P., 2000. *Vortex Methods, Theory and Practice*, Cambridge University Press.
- Crespo, A.J.C., 2008. Application of the Smoothed Particle Hydrodynamics model SPHysics to free-surface hydrodynamics, PhD thesis, Universidade de Vigo, Departamento de Física Aplicada, Spain.
- Cummins, S.J., Rudman, M., 1999. An SPH projection method, *J. Comput. Phys.* **152**, 584-607.
- Daltymple, R.A., Rogers, B.D., 2006. Numerical modeling of water waves with the SPH method, *Coast. Eng.* **53**, 141-147.
- Das, A.K., Das, P.K., 2009. Bubble evolution through submerged orifice using smoothed particle hydrodynamics: Basic formulation and model validation, *Chem. Eng. Sci.* **64**, 2281-2290.
- Delorme, L., 2008. Sloshing flows. Experimental investigation and numerical simulations with smoothed particle hydrodynamics, PhD thesis, Universidad Politécnica de Madrid, Spain.
- De Vahl Davis, G., 1983. Natural convection of air in a square cavity, a bench mark numerical solution, *Int. J. Numer. Meth. Fluids* **3**, 249-264.
- Domínguez, J.M., Crespo, A.J.C., Gómez-Gesteira, 2013. Optimization strategies for CPU and GPU implementations of a smoothed particle hydrodynamics method, *Comput. Phys. Commun.* **184**, 617-627.
- Duineveld, P.C., 1998. Bouncing and coalescence of bubble pairs rising at high Reynolds number in pure water or aqueous surfactant solutions, *Appl. Sci. Res.* **58**, 409-439.
- Dyka, C.T., Ingel, R.P., 1995. An approach for tensile instability in smoothed particle hydrodynamics, *Comput. Struct.* **57**, 573-580.
- Espanol, P., Revenga, M., 2003. Smoothed dissipative particle dynamics, *Phys. Rev. E* **67**, 026705.
- Faber, J., Rasio, F.A., 2000. Post Newtonian calculations of binary neutron stars coalescence. Method and first results, *Phys. Rev. D* **62**, 1-23.
- Faber, J., Rasio, F.A., 2001. Post Newtonian calculations of binary neutron stars coalescence. Mass-ratio, equation of state and spin, *Phys. Rev. D* **63**, 1-16.
- Feldman, J., Bonet, J., 2007. Dynamic refinement and boundary contact forces in SPH with applications in fluid flow problems, *Int. J. Numer. Meth. Eng.* **72**, 295-324.
- Flekkoy, E.G., Coveney, P.V., De Fabritiis, G., 2000. Foundations of Dissipative Particle Dynamics, *Phys. Rev. E* **62**, 2140-2157.

- Frank, X., Funfschilling, D., Midoux, N., Li, H.Z., 2006. Bubble in a viscous liquid: lattice Boltzmann simulation and experimental validation, *J. Fluid Mech.* **546**, 113-122.
- Ghia, U., Ghia, K.N., Shin, C.T., 1982. High Re-resolution for incompressible flow using the Navier-Stokes equations and a multigrid method, *J. Comput. Phys.* **48**, 387-411.
- Gingold, R.A., Monaghan, J.J., 1977. Smoothed Particle Hydrodynamics: Theory and application to non-spherical stars, *Mon. Not. R. Astron. Soc.* **181**, 375-389.
- Gingold, R.A., Monaghan, J.J., 1982. Kernel estimates as a basis for general particle methods in hydrodynamics, *J. Comput. Phys.* **46**, 429-453.
- Grenier, N., Antuono, M., Colagrossi, A., Le Touzé, D., Alessandrini, B., 2009. An Hamiltonian interface SPH formulation for multi-fluid and free-surface flows, *J. Comput. Phys.* **228**, 8380-8393.
- Grimaldi, A., Sollo, A., Guida, M., Marulo, F., 2013. Parametric study of a SPH high velocity impact analysis - A birdstrike windshield application, *Compos. Struct.* **96**, 616-630.
- Gryffits, D.J., 1999. *Introduction to Electrodynamics - 3rd ed.*, Prentice Hall.
- Guida, M., Marulo, F., Meo, M., Grimaldi, A., Olivares, G., 2011. SPH - Lagrangian study of bird impact on leading edge wing, *Compos. Struct.* **93**, 1060-1071.
- Hadamard, J.S., 1911. Mouvement permanent lent d'une sphère liquide et visqueuse dans un liquide visqueux, *CR Acad. Sci.* **152**, 1735-1738.
- Haddad, B., Pastor, M., Palacios, D., Munoz-Salinas, E., 2010. A SPH depth integrated model for Popocatepetl 2001 lahar (Mexico): Sensitivity analysis and runout simulation, *Eng. Geol.* **114**, 312-329.
- Harlow, F., Welch, J.E., 1957. Numerical calculation of time-dependent viscous incompressible flow of fluid with a free surface, *Phys. Fluids* **8**, 2182-2189.
- Hirt, C.W., Nichols, B.D., 1981. Volume of fluid (VOF) method for dynamics of free boundaries, *J. Comput. Phys.* **39**, 201-225.
- Hongbin, J., Xin, D., 2005. On criteria for smoothed particle hydrodynamics kernels in stable field, *J. Comput. Phys.* **202**, 699-709.
- Hoover, W.G., 1998. Isomorphism linking smooth particles and embedded atoms, *Physica A* **260**, 244-254.
- Hu, X.Y., Adams, N.A., 2006. A multi-phase SPH method for macroscopic and mesoscopic flows, *J. Comput. Phys.* **213**, 844-861.
- Hu, X.Y., Adams, N.A., 2007. An incompressible multi-phase SPH method, *J. Comput. Phys.* **227**, 264-278.

- Hu, X.Y., Adams, N.A., 2009. A constant-density approach for incompressible multi-phase SPH, *J. Comput. Phys.* **228**, 2082-2091.
- Hua, J., Lou, J., 2007. Numerical simulation of bubble rising in viscous liquid, *J. Comput. Phys.* **222**, 769-795.
- Hua, J., Stene, J.F., Lin, P., 2008. Numerical simulation of 3D bubbles rising in viscous liquid using a front tracking method, *J. Comput. Phys.* **227**, 3358-3382.
- Hughes, J.P., Graham, D.I., 2010. Comparison of incompressible and weakly-compressible SPH models for free-surface water flows. *J. Hydraul. Res.* **48**, 105-117.
- Jeon, S.-S., Kim, S.-J., Park, G.-C., 2009. CFD simulation of condensing vapor bubble using VOF model, *World Academy of Science, Engineering and Technology* **60**, 209-215.
- Johnson, G.R., Stryk, R.A., Beissel, S.R., 1996. SPH for high velocity impact computations, *Comput. Methods Appl. Mech. Engrg* **139**, 347-373.
- Juric, D., Tryggvason, G., 1996. A front-tracking methods for dendritic solidification, *J. Comput. Phys.* **123**, 127-148.
- Juric, D., Tryggvason, G., 1998. Computations of boiling flows, *Int. J. Multiphase Flow* **24**, 387-410.
- Jutzi, M., Asphaug, E., Gillet, P., Barrat, J.-A., Benz, W., 2013. The structure of the asteroid 4 Vesta as revealed by models of planet-scale collisions, *Nature* **494**, 207-210.
- Kajtar, J.B., Monaghan, J.J., 2010. On the dynamics of swimming linked bodies, *Eur. J. Mech. B-Fluids* **29**, 377-386.
- Kajtar, J.B., Monaghan, J.J., 2012. On the swimming of fish like bodies near free and fixed boundaries, *Eur. J. Mech. B-Fluids* **33**, 1-13.
- Kao, P.-H., Yang, R.-J., 2007. Simulating oscillatory flows in Rayleigh-Benard convection using lattice Boltzmann method, *Int. J. Heat Mass Trans.* **50**, 3315-3328.
- Khayyer, A., Gotoh, H., Shao, S.D., 2008. Corrected incompressible SPH method for accurate water-surface tracking in breaking waves, *Coast. Eng.* **55**, 236-250.
- Kim, J., 2009. Review of nucleate pool boiling bubble heat transfer mechanisms, *Int. J. Multiphase Flow* **35**, 1067-1076.
- Kim, N.H., Ko, S.K., 2008. Numerical simulation on solitary wave propagation and run-up by SPH method, *KSCE J. Civ. Eng.* **12**, 221-226.
- Koshizuka, S., Nobe, A., Oka, Y., 1998. Numerical analysis of breaking waves using the moving particle semi-implicit method, *Int. J. Numer. Meth. Fluids* **26**, 751-769.

- Kunkelmann, C., Stephan, P., 2010. Numerical simulation of the transient heat transfer during nucleate boiling of refrigerant HFE-7100, *Int. J. Refrig.* **33**, 1221-1228.
- Lafaurie, B., Nardone, C., Scardovelli, R., Zaleski, S., Zanetti, G., 1994. Modelling merging and fragmentation in multiphase flows with Surfer, *J. Comput. Phys.* **113**, 134-147.
- Lage, J.L., Bejan, A., 1991. The Ra-Pr domain of laminar convection in an enclosure heated from the side, *Numer. Heat Tr. A-Appl.* **19**, 21-41.
- Lamb, H., 1932. *Hydrodynamics*, Dover, New York.
- Landau, L.D., Lifschitz, J.M., 1987. *Fluid Mechanics*, Pergamon Press.
- Le Touzé, D., Marsh, A., Oger, G., Guilcher, P.M., Khaddaj-Mallat, C., Alessandrini, B., Ferrant, P., 2010. SPH simulation of green water and ship flooding scenarios, *J. Hydrodyn.* **22**, 231-236.
- Lee, E.S., 2007. Truly incompressible approach for computing incompressible flow in SPH and comparisons with traditional weakly compressible approach, PhD thesis, University of Manchester, UK.
- Lee, E.S., Moulinec, C., Xu, R., Violeau, D., Laurence, D., Stansby, P., 2008. Comparisons of weakly compressible and truly incompressible algorithms for the SPH mesh free particle method, *J. Comput. Phys.* **227**, 8417-8436.
- Lee, E.S., Violeau, D., Issa, R., Ploix, S., 2010. Application of weakly compressible and truly incompressible SPH to 3-D water collapse in waterworks. *J. Hydraul. Res.* **48**, 50-60.
- Le Quéré, P., 1991. Accurate solutions to the square thermally driven cavity at high Rayleigh number, *Comput. Fluids* **20**, 29-42.
- Li, J., Liu, H., Gong, K., Tan, S.K., Shao, S., 2012. SPH modeling of solitary wave fissions over uneven bottoms, *Coast. Eng.* **60**, 261-275.
- Liu, M.B., Liu, G.R., 2003. *Smoothed Particle Hydrodynamics: A Meshfree Particle Method*, World Scientific, Singapore.
- Liu, M.B., Liu, G.R., 2006. Restoring particle consistency in smoothed particle hydrodynamics, *Appl. Numer. Math.* **56**, 19-36.
- Liu, M.B., Liu, G.R., Lam, K.Y., 2003. Constructing smoothing functions in smoothed particle hydrodynamics with applications, *J. Comput. Appl. Math.* **155**, 263-284.
- Liu, Z.W., Pakmor, R., Röpke, F.K., Edelman, P., Wang, B., Kromer, M., Hillebrandt, W., Han, Z.W., 2012. Three-dimensional simulations of the interaction between Type Ia supernova ejecta and their main sequence companions, *Astron. Astroph.* **548**, A2.

- Lo, D.C., Murugesan, K., Young, D.L., 2005. Numerical solution of three-dimensional velocity-vorticity Navier-Stokes equations by finite difference method, *Int. J. Numer. Meth. Fluids* **47**, 1469-1487.
- López, H., Sigalotti, L., 2006. Oscillation of viscous drops with smoothed particle hydrodynamics, *Phys. Rev. E* **73**, 051201.
- Lucy, L.B., 1977. A numerical approach to the testing of the fission hypothesis, *Astron. J.* **82**, 1013-1024.
- Marchandise, E., Geuzaine, P., Chevaugeon, N., Remacle, J.F., 2007. A stabilized finite element method using a discontinuous level set approach for the computation of bubble dynamics, *J. Comput. Phys.* **225**, 949-974.
- Marrone, S., Colagrossi, A., Antuono, M., Lugni, C., Tulin, M.P., 2011. A 2D+t SPH model to study the breaking wave pattern generated by fast ships, *J. Fluids Struct.* **27**, 1199-1215.
- McKee, S., Tomé, M.F., Ferreira, V.G., Cuminato, J.A., Castelo, A., Sousa, F.S., Mangiavacchi, N., 2008. The MAC method, review, *Comput. Fluids* **37**, 907-930.
- Minier, J.P., Pozorski, J., 1999. Wall boundary conditions in PDF methods and application to a turbulent flow, *Phys. Fluids* **11**, 2632-2644.
- Monaghan, J.J., 1989. On the problem of penetration in particle methods, *J. Comput. Phys.* **82**, 1-15.
- Monaghan, J.J., 1992. Smoothed Particle Hydrodynamics, *Ann. Rev. Astron. Astrophys.* **30**, 543-574.
- Monaghan, J.J., 1994. Simulating free surface flows with SPH, *J. Comput. Phys.* **110**, 399-406.
- Monaghan, J.J., 2000. SPH without a tensile instability, *J. Comput. Phys.* **159**, 290-311.
- Monaghan, J.J., 2005a. Smoothed Particle Hydrodynamics, *Rep. Prog. Phys.* **68**, 1703-1759.
- Monaghan, J.J., 2005b. Smoothed Particle Hydrodynamics, IPAM Notes, School of Mathematical Sciences, Monash University, Melbourne, Australia.
- Monaghan, J.J., 2012. Smoothed Particle Hydrodynamics and its diverse applications, *Ann. Rev. Fluid Mech.* **44**, 323-346.
- Monaghan, J.J., Huppert, H.E., Worster, M.G., 2005. Solidification using smoothed particle hydrodynamics, *J. Comput. Phys.* **206**, 684-705.
- Morris, J.P., 1996. Analysis of Smoothed Particle Hydrodynamics with Applications, PhD thesis, Department of Mathematics, Monash University, Australia.
- Morris, J.P., 2000. Simulating surface tension with smoothed particle hydrodynamics, *Int. J. Numer. Meth. Fluids* **33**, 333-353.

- Morris, J.P., Fox, P.J., Zhu, Y., 1997. Modeling low Reynolds number incompressible flows using SPH, *J. Comput. Phys.* **136**, 214-226.
- Nagamine, K., Springel, V., Hernquist, L., 2004. Star formation rate and metallicity of damped Lyman α absorbers in cosmological particle hydrodynamics simulations, *Mon. Not. R. Astron. Soc.* **348**, 435-450.
- Nagasawa, M., Nakamura, T., Miyama, S.M., 1988. Three-dimensional hydrodynamics simulations of type II supernova - mixing and fragmentation of ejecta, *Publ. Astron. Soc. Jpn.* **40**, 691-708.
- Nugent, S., Posch, H.A., 2000. Liquid drops and surface tension with smoothed particle applied mechanics. *Phys. Rev. E* **62**, 4968-4975.
- Ohta, M., Imura, T., Yoshida, Y., Sussman, M., 2005. A computational study of the effect of initial bubble conditions on the motion of a gas bubble rising in viscous liquids, *Int. J. Multiphase Flow* **31**, 223-237.
- Pesso, T., Piva, S., 2009. Laminar natural convection in a square cavity: Low Prandtl numbers and large density differences, *Int. J. Heat Mass Trans.* **52**, 1036-1043.
- Pianet, G., Vincent, S., Leboi, J., Caltagirone, J.P., Anderhuber, M., 2010. Simulating compressible gas bubbles with smooth volume tracking 1-Fluid method, *Int. J. Multiphase Flow* **36**, 273-283.
- Pope, S.B., 1994. Lagrangian PDF methods for turbulent flows, *Annu. Rev. Fluid Mech.* **26**, 23-63.
- Pozorski, J., Wawreńczuk, A., 2002. SPH computation of incompressible viscous flows, *J. Theor. Appl. Mech. (Pol.)* **40**, 917-937.
- Prakash, M., Cleary, P.W., 2011. Three dimensional modelling of lava flow using Smoothed Particle Hydrodynamics, *Appl. Math. Model.* **35**, 3021-3035.
- Randles, P.W., Libersky, L.D., 2000. Normalized SPH with stress points. *Int. J. Numer. Meth. Eng.* **48**, 1445-1462.
- Ritchie, B.W., Thomas, P.A., 2001. Multiphase smoothed-particle hydrodynamics, *Mon. Not. R. Astron. Soc.* **323**, 743-756.
- Robinson, M., 2009. Turbulence and Viscous Mixing using Smoothed Particle Hydrodynamics, PhD thesis, Monash University, Australia.
- Rybczynski, W., 1911. On the translatory motion of a fluid sphere in a viscous medium, *Bull. Int. Acad. Pol. Sci. Lett., Sci. Math. Nat. Ser. A*, 40-46.
- Sankaranarayanan, K., Kevrekidis, K., Sundaresan, I.G., Lu, J., Tryggvason, G., 2003. A comparative study of lattice Boltzmann and front-tracking finite-difference methods for bubble simulations, *Int. J. Multiphase Flow* **29**, 109-116.

- Sankaranarayanan, K., Shan, X., Kevrekidis, K., Sundaresan, I.G., 1999. Bubble flow simulations with the lattice Boltzmann method, *Chem. Sci. Eng.* **54**, 4817-4823.
- Shao, J.R., Li, H.Q., Liu, G.R., Liu, M.B., 2012. An improved SPH method for modeling liquid sloshing dynamics, *Comput. Struct.* **100**, 18-26.
- Shao, S., Lo, E.Y., 2003. Incompressible SPH method for simulating Newtonian and non-Newtonian flows with a free surface, *Adv. Water Resour.* **26**, 787-800.
- Shao, S., Ji, C., Graham, D.I., Reeve, D.E., James, P.W., Chadwick, A.J., 2006. Simulation of wave overtopping by an incompressible SPH model, *Coast. Eng.* **53**, 723-735.
- Shapiro, P.R., Martel, H., Villumsen, J.V., Owen, J., 1996. Adaptive Smoothed Particle Hydrodynamics with application to cosmology: methodology, *Astrophys. J. Suppl.* **103**, 269-330.
- Shen, H.T., Su, J., Liu, L., 2000. SPH simulation of river ice dynamics, *J. Comput. Phys.* **165**, 752-770.
- Shepard, D., 1968. A two-dimensional interpolation function for irregularly-spaced data, *Proceedings of ACM National Conference*, 517-524.
- Schoenberg, I.J., 1946. Contributions to the problem of approximation of equidistant data by analytic functions, *Q. Appl. Math.* **4**, 45-99.
- Shu, C., Wang, L., Chew, Y.T., 2003. Numerical computation of three-dimensional incompressible Navier-Stokes equations in primitive variable form by DQ method, *Int. J. Numer. Meth. Fluids* **43**, 345-368.
- Sinnott, M.D., Cleary, P.W., Arkwright, J.W., Dinning, P.G., 2012. Investigating the relationship between peristaltic contraction and fluid transport in the human colon using Smoothed Particle Hydrodynamics, *Comput. Biol. Med.* **42**, 492-503.
- Springel, V., 2010. Smoothed Particle Hydrodynamics in astrophysics, *Annu. Rev. Astron. Astr.* **48**, 391-430.
- Springel, V., White, S.D.M., Jenkins, A., Frenk, C.S., Yoshida, N., Gao, L., Navarro, J., Thacker, R., Croton, D., Helly, J., Peacock, J.A., Cole, S., Thomas, P., Couchman, H., Evrard, A., Colberg, J., Pearce, F., 2005. Simulating the joint evolution of quasars, galaxies and their large-scale distribution, [arXiv:astro-ph/0504097](https://arxiv.org/abs/astro-ph/0504097).
- Sussman, M., Smereka, P., 1997. Axisymmetric free boundary problems, *J. Fluid Mech.* **341**, 269-294.
- Sussman, M., Smereka, P., Osher, S.J., 1994. A level-set approach for computing solutions to incompressible two-phase flow, *J. Comput. Phys.* **114**, 146-159.
- Swegle, J.W., Hicks, D.L., Attaway, S.W., 1995. Smoothed Particle Hydrodynamics stability analysis, *J. Comput. Phys.* **116**, 123-134.

- Szewc, K., 2010. Smoothed Particle Hydrodynamics - the implementations of the incompressibility, *Copernican Letters* **1**, 141-154.
- Szewc K., 2011. Broken-dam simulations using Smoothed Particle Hydrodynamics, *Copernican Letters* **2**, 183-191.
- Szewc, K., Pozorski, J., 2010. Development of smoothed particle hydrodynamics (SPH) approach for simulation of wall boiling (first progress report), internal report, Institute of Fluid-Flow Machinery, Polish Academy of Sciences.
- Szewc, K., Pozorski, J., 2011. Development of smoothed particle hydrodynamics (SPH) approach for simulation of wall boiling (second progress report), internal report, Institute of Fluid-Flow Machinery, Polish Academy of Sciences.
- Szewc, K., Pozorski, J., 2012. Development of smoothed particle hydrodynamics (SPH) approach for simulation of wall boiling (third progress report), internal report, Institute of Fluid-Flow Machinery, Polish Academy of Sciences.
- Szewc, K., Pozorski, J., Minier, J.P., 2012a. Analysis of the incompressibility constraint in the SPH method, *Int. J. Numer. Methods Eng.* **92**, 343-369.
- Szewc, K., Pozorski, J., Minier, J.-P., 2013. Simulations of single bubbles rising through viscous liquids using Smoothed Particle Hydrodynamics, *Int. J. Multi-phase Flow* **50**, 98-105.
- Szewc, K., Pozorski, J., Tanière, A., 2011. Modeling of natural convection with Smoothed Particle Hydrodynamics: Non-Boussinesq formulation, *Int. J. Heat Mass Trans.* **54**, 4807-4816.
- Szewc, K., Tanière, A., Pozorski, J., Minier, J.-P., 2012b. A study on application of smoothed particle hydrodynamics to multi-phase flows, *Int. J. Nonlinear Sci. Numer. Simul.* **13**, 383-395.
- Takada, N., Misawa, M., Tomiyama, A., Fujiwara, S., 2000. Numerical simulation of two- and three-dimensional two-phase fluid motion by lattice Boltzmann method, *Comput. Phys. Commun.* **129**, 233-246.
- Takeda, H., Miyama, S.M., Sekiya, M., 1994. Numerical simulation of viscous flow by Smoothed Particle Hydrodynamics, *Prog. Theor. Phys.* **95**, 939-960.
- Tartakovsky, A.M., Ferris, K.F., Meakin, P., 2009. Lagrangian particle model for multiphase flows, *Comput. Phys. Commun.* **180**, 1874-1881.
- Tartakovsky, A., Meakin, P., 2005. Modeling of surface tension and contact angles with smoothed particle hydrodynamics, *Phys. Rev. E* **72**, 026301.
- Trac, H., Sills, A., Pen U.-L., 2007. A comparison of hydrodynamic techniques for modelling collisions between main-sequence stars, *Mon. Not. R. Astron. Soc.* **377**, 997-1005.
- Tryggvason, G., Bunner, B., Esmaeeli, A., Juric, D., Al-Rawahi, N., Tauber, W., Han, J., Nas, S., Jan, Y.-J., 2001. A front-tracking method for the computations of multiphase flow, *J. Comput. Phys.* **169**, 708-759.

- Tryggvason, G., Esmaeeli, A., Al-Rawahi, N., 2005. Direct numerical simulations of flows with phase change, *Comput. Struct.* **83**, 445-453.
- Tryggvason, G., Scardovelli, R., Zaleski, S., 2011. *Direct Numerical Simulations of Gas-Liquids Multiphase Flows*, Cambridge Univ. Press, Cambridge.
- Unverdi, S.O., Tryggvason, G., 1992. A front-tracking method for viscous, incompressible, multi-fluid flows, *J. Comput. Phys.* **100**, 25-37.
- Valizadeh, A., Shafieefar, M., Monaghan, J.J., Salehi Neyshaboori, S.A., 2008. Modeling two-phase flows using SPH method, *J. Appl. Sci.* **8**, 3817-3826.
- Vandamme, J., Zou, Q., 2012. Novel particle method for modelling the episodic collapse of soft coastal bluffs, *Geomorphology* **138**, 295-305.
- Van der Vorst, H.A., 1992. Bi-CGSTAB: a fast and smoothly converging variant of Bi-CG for solution of nonsymmetric linear systems. *SIAM J. Sci. Stat. Comp.* **2**, 631-644.
- Van Sint Annaland, M., Deen, N.G., and Kuipers, J.A.M., 2005. Numerical simulation of gas bubbles behavior using a three-dimensional volume of fluid method, *Chem. Eng. Sci.* **60**, 2999-3011.
- Veen, D., Gourlay, T., 2012. A combined strip theory and Smoothed Particle Hydrodynamics approach for estimating slamming loads on a ship in head seas, *Ocean Eng.* **43**, 64-71.
- Vierendeels, J., Merci, B., Dick, E., 2004. A multigrid method for natural convective heat transfer with large temperature differences, *J. Comput. Appl. Math.* **168**, 509-517.
- Wan, D.C., Patnaik, S.V., Wei, G.W., 2001. A new benchmark quality solution for buoyancy-driven cavity by discrete singular convolution, *Num. Heat Tr. B-Fund.* **40**, 199-228.
- Watkins, S.J., Bhattal, A.S., Francis, N., Turner, J.A., Whitworth, A.P., 1996. A new prescription for viscosity in Smoothed Particle Hydrodynamics, *Astron. Astrophys. Suppl. Ser.* **119**, 177-187.
- Wendland, H., 1995. Piecewise polynomial, positive definite and compactly supported radial functions of minimal degree, *Adv. Comput. Math.* **4**, 389-396.
- Wenxiao, P., Tartakovsky, A.M., Monaghan, J.J., A smoothed-particle hydrodynamics model for ice-sheet and ice-shelf dynamics, *J. Glaciol.* **58**, 216-222.
- Xu, R., 2009. *An Improved Incompressible Smoothed Particle Hydrodynamics Method and Its Application in Free-Surface Simulations*, PhD thesis, Faculty of Engineering and Physical Sciences, University of Manchester, UK.
- Xu, R., Stansby, P., Laurence, D., 2009. Accuracy and stability in incompressible SPH (ISPH) based on the projection method and a new approach, *J. Comput. Phys.* **228**, 6703-6725.

- Yildiz, M., Rook, R.A., Suleman, A., 2008. SPH with multiple boundary tangent method, *Int. J. Numer. Meth. Eng.* **77**, 1416-1438.
- Yoon, H.Y., Koshizuka, S., Oka, Y., 2001. Direct calculation of bubble growth, departure, and rise in nucleate pool boiling, *Int. J. Multiphase Flow* **27**, 277-298.
- Zalesak, S.T., 1979. Fully multidimensional flux-corrected transport algorithms for fluids, *J. Comput. Phys.* **31**, 335.
- Zhou, G., Ge, W., Li, J., 2008. A revised surface tension model for macro-scale particle methods, *Powder Technol.* **183**, 21-26.
- Zhu, H.P., Zhou, Z.Y., Yang, R.Y., Yu, A.B., 2008. Discrete particle simulation of particulate systems: A review of major applications and findings, *Chem. Eng. Sci.* **63**, 5728-5770.

List of publications

During the author's candidature, several articles relating to the subject of this thesis were published in the printed or electronic version:

- Szewc, K., Pozorski, J., Minier, J.-P., 2013. Simulations of single bubbles rising through viscous liquids using Smoothed Particle Hydrodynamics, *Int. J. Multiphase Flow*. **50**, 98-105.
- Szewc, K., Pozorski, J., Minier, J.P., 2012. Analysis of the incompressibility constraint in the SPH method, *Int. J. Numer. Methods Eng.* **92**, 343-369.
- Szewc, K., Tanière, A., Pozorski, J., Minier, J.-P., 2012. A study on application of smoothed particle hydrodynamics to multi-phase flows, *Int. J. Nonlinear Sci. Numer. Simul.* **13**, 383-395.
- Szewc, K., Pozorski J., 2012. Buoyancy driven, multi-phase flow simulations using smoothed particle hydrodynamics, XX Fluid Dynamics Conference, Gliwice, 2012.
- Szewc, K., Pozorski, J., 2012. Development of smoothed particle hydrodynamics (SPH) approach for simulation of wall boiling (third progress report), internal report, Institute of Fluid-Flow Machinery, Polish Academy of Sciences.
- Szewc, K., 2011. Broken-dam simulations using Smoothed Particle Hydrodynamics, *Copernican Letters* **2**, 183-191.
- Szewc, K., Pozorski, J., Tanière, A., 2011. Modeling of natural convection with Smoothed Particle Hydrodynamics: Non-Boussinesq formulation, *Int. J. Heat Mass Trans.* **54**, 4807-4816.
- Szewc, K., Tanière, A., 2011. A study on application of Smoothed Particle Hydrodynamics to multi-phase flows, 12th International Conference Multiphase Flow in Industrial Plants, Ischia, Italy.
- Szewc, K., Pozorski, J., 2011. Symulacje numeryczne przepływów wielofazowych metodą Smoothed Particle Hydrodynamics, II Kongres Mechaniki Polskiej, Poznań 2011, Poland.
- Szewc, K., Pozorski, J., 2011. Development of smoothed particle hydrodynamics (SPH) approach for simulation of wall boiling (second progress report), internal report, Institute of Fluid-Flow Machinery, Polish Academy of Sciences.

- Szewc, K., 2010. Smoothed Particle Hydrodynamics - the implementations of the incompressibility, *Copernican Letters* **1**, 141-154.
- Szewc, K., Pozorski, J., 2010. Development of smoothed particle hydrodynamics (SPH) approach for simulation of wall boiling (first progress report), internal report, Institute of Fluid-Flow Machinery, Polish Academy of Sciences.